Towards an Understanding of Core-Collapse Supernovae

David Vartanyan

A Dissertation
Presented to the Faculty
of Princeton University
in Candidacy for the Degree
of Doctor of Philosophy

Recommended for Acceptance
by the Department of
Astrophysical Sciences
Adviser: Professor Adam Burrows

September 2019

Abstract

The explosion mechanism of core-collapse supernovae (CCSNe) is a long-standing astrophysical problem buttressed with over half a century of computational research. Neutrino heating of the collapsing mantle, wherein a fraction of the profuse neutrino luminosity in a collapsing star deposits energy onto the stalled shock, remains the preferred explosion mechanism for garden-variety CCSNe. Recent improvements in neutrino physics and in supercomputer power jointly ushered in new capabilities for the study of CCSNe. FORNAX is an optimized state-of-the-art hydrodynamics/radiative transfer code with detailed microphysics and scalable design that effectively takes advantage of these developments. I implement FORNAX to provide a comprehensive, multi-dimensional study of CCSNe − horizontally-integrated, across a a broad suite of progenitor stars, and vertically-integrated, from explosion mechanism to observational signatures.

I provide a broad introduction of the topic, the code FORNAX, and the rich history of research in CCSNe in Chapter 1. Chapter 2 looks at the sensitive dependence of explosion outcome on neutrino microphysics, in particular the role of many-body interactions and inelastic neutrino scattering. Chapter 3 builds on these results to identify drivers of explosion outcome in a series of 2D axisymmetric simulations. Chapter 4 introduces the first 3D simulation by FORNAX. A 16-$M_\odot$ progenitor is carried out to roughly one second post-bounce, exploding promptly and robustly. The results highlight the need to carry simulations out longer, to several seconds, to identify asymptotic explosion energies. In Chapter 5, I look at neutrino and gravitational wave observational signatures, and their correlations with core physical dynamics, with a series of 11 progenitors evolved in 3D. This is the largest suite of 3D simulations to date, allowing a study of global characteristics of a diverse set of progenitor stars. The synergistic study of neutrinos and gravitational waves in forthcoming detectors can be used to profitably study physical phenomena in the supernova core.

CCSNe study has followed a Maslow hierarchy in ambition: first, to produce successful explosions; second, to produce robust explosion energies, and lastly, to produce CCSNe consistent with observable diagnostics. My thesis establishes well the first point, embarks on the second, and courts the third.

Acknowledgements

I would like to thank my advisor, Adam Burrows, who reached out to me near the end of my 2nd year and, in short work, deprived other professors of my utility. His work ethic is rivaled only by his sense of humor.

I am grateful to Joshua Dolence and Aaron Skinner as well as to local collaborators David Radice, Hiroki Nagakura, and Viktoriya Giranskaya for wonderful discussions and generous patience. All were instrumental to my education.

My advising committee, James Stone, Renyue Cen, Matthew Kunz, and Jeremey Goodman, deserves a special thank you for the valuable feedback and valiant attempts to stay awake during our committee meetings.

I am grateful to Jill Knapp, who helped make my studies at Princeton a reality. I would like to thank my first semester-project advisor, Roman Rafikov, for showing me the ropes early on. I am grateful to Jenny Greene and Anthony Piro for essential and continued guidance along the way. I am grateful to the department staff, and to Polly Strauss for her wonderful persona and helpfulness.

Special thanks go to Melinda Soares-Furtado, Yusra AlSayyad, Jamie Rankin, Eric Rogers, Amy Secunda, Claudia Brunner, and Amberly Simpson for embarking on our (award-winning) Dance Your PhD (see the final page, photo credit to Lance Beden). The effort goes to show that the human mind has no limits when finding creative avenues to procrastinate writing a thesis.

In addition to Melinda, I'd like to recognize Joshua Wallace and Kris Pardo as companions-in-arms. Special thanks also go to all my fellow Princeton Astrophysics students, and particularly to the Cookie Czars, and to all whom I have not named.

Above all, I am grateful to God for sustaining my strength, to my mother Marine, my father Sarkis, and my brother Mihran for sharing in my frustrations and joys, mitigating the former and magnifying the latter. Their faith nurtures mine.

To the reader

Relation to Published Work

Chapter 2 is based on a collaboration with Adam Burrows published in the Space Science Reviews, Volume 241 p. 33 (Burrows et al., 2018). The work was presented at the American Astronomical Society (AAS) Meeting #229 (Vartanyan & Burrows, 2017) as well as at the American Physics Society, Mid-Atlantic Annual Meeting in Newark, NJ 2017.

Chapter 3 is based on a collaboration with Adam Burrows and the Princeton group published in the Monthly Notices of the Royal Astronomical Society, Volume 477 p. 30910−3108 (Vartanyan et al., 2018b) and presented at AAS Meeting #231 (Vartanyan et al., 2018a) as well as at the Wilhelm und Else Heraeus-Seminar: Supernovae - From Simulations to Observations and Nucleosynthetic Fingerprint in Bad Honnef, Germany 2018.

Chapter 4 is based on a collaboration with Adam Burrows and the Princeton group published in the Monthly Notices of the Royal Astronomical Society, Volume 482 p. 351−369 (Vartanyan et al., 2019b) and presented at AAS Meeting #233 (Vartanyan & Burrows, 2019).

Chapter 5 is based on a collaboration with Adam Burrows and the Princeton group in a forthcoming publication, accepted by the Monthly Notices of Royal Astronomical Journal, with the preprint available at Vartanyan et al. (2019a). The work was presented at MICRA 2019: Microphysics in Computational Relativistic Astrophysics in Jena, Germany 2019.

Contents

Chapter 1

Introduction

1.1 A Brief History

Stemming from the Latin word "novus" for new, supernovae are the explosive deaths of stars. First coined by Baade & Zwicky (1934) to distinguish them from "nova," supernovae are several thousand times brighter than their cognates. Supernovae are broadly categorized as either thermonuclear or core-collapse. The former are driven by ignition of thermonuclear fusion; the latter, more humbly, by gravity. My study focuses on the latter, aptly termed core-collapse supernovae (CCSNe), which are triggered by gravitational collapse in the iron cores of massive stars.

Stars evolve through a dynamic between gravity and pressure. In the stellar core, nuclear fusion initially burns hydrogen into helium, and into consecutively heavier elements. Stars more than 8 $M_\odot$ (with initial mass function-weighted mean masses of $\sim 12-15 M_\odot$) burn up to iron in the core over million year lifetimes. Iron lies near the peak of the nuclear binding energy curve (Nickel-62 is most tightly bound), and hence further nuclear fusion of iron is endothermic and can no longer sustain the star against gravitational collapse. Additionally, electron capture on heavy nuclei and photo-dissociation of iron into helium nuclei sap pressure support. This culmi-

nation of events triggers core collapse on a freefall timescale of seconds. The outer supersonically collapsing envelope of the star is oblivious to the homologous collapse manifesting in the inner core.

During collapse, once the density reaches $\sim 10^{12}$ g cm^{-3}, Freedman scattering of neutrinos off nuclei effectively traps the neutrinos in the infalling material, with mean free paths of tens of centimeters at these high densities. Neutrino trapping during collapse maintains an electron fraction Y_e of $\sim$0.3, down from a pre-collapse value of $\sim$0.44, and staves off core bounce. Because the Chandrasekhar mass scales with Y_e^2, the core mass after neutrino trapping is $\sim$0.5 M$_\odot$. Once the collapsing core reaches nuclear densities $\sim 2.6\times10^{14}$ g cm^{-3}, the strong nuclear force becomes repulsive and the equation of state for the core stiffens. The collapse overshoots and bounces forcefully outward, driving a shock wave into the outer envelope. After neutrino trapping, the core bounces and collapses within a free-fall time of

$$t_{\rm ff} \sim \frac{1}{\sqrt{G\rho}} \sim \frac{1}{\sqrt{\rho_{13}}} \text{ ms.} \tag{1.1}$$

At bounce, the gravitational binding released from collapsing a core with a Chandrasekhar mass of M$_c$ $\sim$1.4 M$_\odot$ and a radius R$_c$ of $\sim$10,000 km to a proto-neutron star (PNS) with comparable mass but a radius of R$_{\rm PNS}$ $\sim$12 km is of order,

$$E_{Grav} \sim G M_c^2 \left(\frac{1}{R_{\rm PNS}} - \frac{1}{R_c} \right) \sim 10^{53} \, \text{ergs} \, . \tag{1.2}$$

Shock breakout is accompanied by an electron neutrino burst, resulting from electron capture on protons behind the shock. Deleptonization and neutronization in the inner core allows for the formation of positrons, which was prior suppressed by the high electron chemical potential. Subsequent $e^- e^+$ pair annihilation and nucleon bremsstrahlung source heavy-neutrinos "ν_μ" and electron anti-neutrinos, whose breakout burst is delayed and muted relative to electron neutrinos. The breakout

neutrino burst − which dissipates the shock of energy − and photodissociation − which unbinds nuclei at the expense of the kinetic pressure − together debilitate the shock. As a result the shock "stalls" and is buried under the ram pressure of the infalling material. CCSNe theory attempts to understand how the stalled shock is "revived," typically within a few hundred milliseconds in simulations, to produce robust explosions.

The requisite CCSNe mechanism must be able to reproduce explosion statistics, energies, and observable diagnostics consistent with observations and theory. The preferred mechanism for shock revival and CCSNe explosion is the neutrino-heating mechanism. The dominant reactions in CCSNe involved are charged-current, absorption reactions of electron neutrinos and anti-neutrinos off free nucleons,

$$\nu_e + n \longrightarrow p + e^-$$
$$\bar{\nu}_e + p \longrightarrow n + e^+ .$$

More than 99% of the gravitational binding energy in a CCSNe is released through neutrinos, and the neutrino-heating mechanism requires only a small fraction of this energy to couple with the matter in the collapsing star via the weak force to revive the stalled shock. Shock revival is often used as a proxy for explosion. However, a true merit of explosion would be confirming that the star becomes gravitationally unbound, which requires carrying out simulations for longer. As we will repeat throughout, we find rapidly growing explosion energies even one second after bounce for many of our exploding progenitors in 3D, emphasizing the need for longer simulations to capture asymptotic explosion energies of CCSNe.

Core-collapse supernovae are critical to understand because they dynamically influence the interstellar medium, source cosmic rays and dominate the relic cosmic neutrino background (Mathews et al. 2019), produce much of the elemental abun-

dances in the universe (Burbidge et al. 1957), and can even be used as standard candles to calibrate cosmological distances (Kasen & Woosley 2009). CCSNe theory can be compared to observations by fitting stellar evolution models using, e.g MESA (Farmer et al. 2016), to observed optical light curves and photospheric velocities (Ricks & Dwarkadas 2019; Morozova et al. 2018a; Goldberg et al. 2019). Observations yield mean estimated explosion energies of 10^{51} ergs, or one Bethe (Kasen & Woosley 2009). Current 3D CCSNe models seem as-of-yet under-energetic (see, e.g. Murphy et al. 2019) compared to observations, but as we will demonstrate throughout, and in particular in Chapter 4, the resolution may lie simply with continuing 3D simulations for longer, as many of our models have not yet asymptoted to explosion energy after one second of evolution post-bounce.

Supernovae have held historical significance. There is petroglyph evidence of possible detection of supernova HB9 roughly 5000 BC (Hamacher 2014), and possibly even of the Vela supernova more than 10,000 BC. Early written records of supernovae date back to 1054 A.D in China during the Song Dynasty rule. In 1940, Gamow & Schoenberg (1940) first associated neutrinos with supernovae, and identified core collapse as a possible trigger for such explosions. However, it was not until Colgate & White (1966) that the neutrino-heating mechanism for producing CCSNe was established: core collapse of an unstable star would yield a profusion of neutrinos, which would then deposit energy in the envelope of the star to produce an explosion. By the work of Bethe & Wilson (1985), the neutrino-heating mechanism, requiring only $\sim$0.1% of the released neutrino flux to revive a stalled shock, was the preferred explosion mechanism for CCSNe. Two years later, SN1987a provided the first detection of neutrinos (an ample nineteen) from a supernova (as well as evidence of Cobalt-56 radioactive-decay powering the optical light curve).

1.2 FORNAX

FORNAX (Skinner et al. 2016, 2019; Wallace et al. 2016; Burrows et al. 2018, 2019; Seadrow et al. 2018; Morozova et al. 2018b; Radice et al. 2017, 2019; Vartanyan et al. 2018b, 2019b,a; Nagakura et al. 2019a) is a multi-dimensional, multi-group radiation transport/hydrodynamics (rad/hydro) code used to study CCSNe. FORNAX solves the comoving-frame velocity-dependent transport equations to order $O(v/c)$. The hydrodynamics uses a directionally-unsplit Godunov-type finite-volume scheme and computes fluxes at cell interfaces using an HLLC Riemann solver. Across the shock interface, the solver switches to HLLE to minimize diffusion and overcome the carbuncle problem. It employs a spherical dendritic grid that deresolves in radial and azimuthal binning at small radii and along the pole in order to overcome the Courant condition.

FORNAX solves the four conservation equations for mass, momentum, energy, and lepton number. The Newtonian form of the equations is as follows:

$$\rho_{,t} + (\rho \mathbf{v^i})_{;\mathbf{i}} = 0\,, \tag{1.3a}$$

$$(\rho \mathbf{v_j})_{,t} + (\rho \mathbf{v^i v_j} + P\delta^i_j)_{;i} = -\rho\phi_{,j} + c^{-1}\sum_s \int_0^\infty (\kappa_{s\varepsilon} + \sigma^{\rm tr}_{s\varepsilon})\mathbf{F}_{s\varepsilon j} d\varepsilon\,, \tag{1.3b}$$

$$\begin{aligned}\left[\rho\left(e + \frac{1}{2}\|\mathbf{v}\|^2\right)\right]_{,t} + \left[\rho\mathbf{v^i}\left(e + \frac{1}{2}\|\mathbf{v}\|^2 + \frac{P}{\rho}\right)\right]_{;i} &= -\rho v^i \phi_{,i} \\ &- \sum_s \int_0^\infty \left(j_{s\varepsilon} - c\kappa_{s\varepsilon}E_{s\varepsilon} - \frac{\mathbf{v}^i}{c}(\kappa_{s\varepsilon} + \sigma^{\rm tr}_{s\varepsilon})\mathbf{F}_{s\varepsilon i}\right) d\varepsilon\,,\end{aligned} \tag{1.3c}$$

$$(\rho Y_e)_{,t} + (\rho Y_e \mathbf{v}^i)_{;i} = \sum_s \int_0^\infty \xi_{s\varepsilon}(j_{s\varepsilon} - c\kappa_{s\varepsilon}E_{s\varepsilon}) d\varepsilon\,, \tag{1.3d}$$

where e is the specific internal energy, $P = P(\rho, e, Y_e)$ is the pressure, ρ is the mass density, Y_e is the electron fraction, v_i are the velocity components, $\kappa_{s\varepsilon}$ and $\sigma^{\rm tr}_{s\varepsilon}$ are

the absorption and transport scattering opacities, and $s \in \{\nu_e, \bar{\nu}_e, \text{“}\nu_\mu\text{”}\}$, where

$$\xi_{s\varepsilon} = \begin{cases} -(N_A\varepsilon)^{-1} & s = \nu_e, \\ (N_A\varepsilon)^{-1} & s = \bar{\nu}_e, \\ 0 & s = \nu_x\,. \end{cases} \tag{1.4}$$

N_A is Avogadro's number.

The radiation transport operators are treated with an explicit Godunov characteristic method. The neutrino source and sink terms coupling radiation to matter are operator split and treated implicitly. For neutrino energies, we use logarithmically spaced bins from 0−300 MeV for electron-neutrinos, and 0−100 MeVf for electron anti-neutrinos and “heavy”-neutrinos, “ν_μ”, where we bundle μ,τ neutrinos and anti-neutrinos into one species. The high muon and tauon rest masses suppress their formation (but see Bollig et al. 2017), and electron anti-neutrinos are suppressed by the high electron chemical potential.

We solve for radiation transport using M1 closure, which takes the first two moments of the Boltzmann transport equation (energy and the flux vector (E, **F**) and approximates the subsequent two moments (pressure and heat tensors, **P, Q**) using an analytic expression (Vaytet et al. 2011). The two moments are as follows:

$$E_{s\varepsilon,t} + (\alpha \mathbf{F}^i_{s\varepsilon} + \mathbf{v}^i E_{s\varepsilon})_{;i} - \alpha \mathbf{v}^i_{;j} \frac{\partial}{\partial \ln \varepsilon} \mathbf{P}^j_{s\varepsilon i} = \alpha(j_{s\varepsilon} - c\kappa_{s\varepsilon} E_{s\varepsilon}) + \alpha G^e\,, \tag{1.5}$$

$$\mathbf{F}_{s\varepsilon j,t} + (c^2 \alpha^i_{s\varepsilon j} + \mathbf{v}^i \mathbf{F}_{s\varepsilon j})_{;i} + \alpha \mathbf{v}^i_{;j} \mathbf{F}_{s\varepsilon i} - \alpha v^i_{;k} \frac{\partial}{\partial \varepsilon} (\varepsilon \mathbf{Q}^k_{s\varepsilon ji}) \; = -c\alpha(\kappa_{s\varepsilon} + \sigma^{\mathrm{tr}}_{s\varepsilon}) \mathbf{F}_{s\varepsilon j} + \alpha \mathbf{G}^m_j\,. \tag{1.6}$$

$\mathrm{E}_{s\varepsilon}$ is the radiation energy density spectrum (zeroth moment), $\mathbf{F}_{s\varepsilon i}$ is the radiation flux spectrum (first moment), $\mathbf{P}^i_{s\varepsilon j}$ is the radiation pressure tensor (second moment),

$\mathbf{Q}^k_{s\varepsilon ji}$ is the heat tensor (third moment), $\alpha = \exp(\phi/c^2)$, and the other variables have their standard meanings. ϕ is the gravitational potential.

We approximate relativistic gravity following Case B of Marek et al. (2006). In our above moment equations, G^e and $\mathbf{G}^m_j$ are gravitational redshift corrections. The potential ϕ is the GR-corrected monopole term ϕ_{TOV}, and we include both velocity and redshift corrections due to GR.

For neutrino interactions, we include a detailed suite of microphysical interactions. To highlight the magnitude of the weak force for neutrino-matter interactions, a characteristic neutrino cross-section is

$$\sigma_0 = \frac{4G_F^2(m_e c^2)^2}{\pi(\hbar c)^4} \sim 1.7 \times 10^{-44}\ \mathrm{cm}^2\,, \tag{1.7}$$

almost two decades smaller in magnitude than the cross section for Thomson scattering of a photon off an electron. G_F is the Fermi constant.

For neutrino-nucleon scattering (neutral-current) and absorption (charged current), we use the formalism of Burrows et al. (2006). For inelasticity in neutrino-nucleon and neutrino-electron scattering, we follow Burrows & Thompson (2004). For nucleon-nucleon bremsstrahlung and electron-positron pair annihilation, which dominate heavy neutrino production, we follow the formalism in Thompson et al. (2000). For electron capture on nuclei during infall, we use Juodagalvis et al. (2010). We do not include neutrino flavor-changing reactions, whose rates are low compared to the other reactions included.

Weak magnetism and recoil corrections are included in both scattering absorption reactions as multiplicative terms. Pauli exclusion is included via the stimulated emission term in Burrows et al. (2006). We include the many-body correction to neutrino-nucleon scattering following Horowitz et al. (2017), which fits to high densities following Burrows & Sawyer (1998). A corresponding fit for charged-current

reactions has not yet been calculated nor included (Roberts & Reddy 2017). For detailed information about the code setup and tests, see Skinner et al. (2019).

1.3 The Computational CCSNe Community

Here we highlight the distinct advantages of FORNAX within the 3D computational CCSNe community by highlighting relative strengths and weaknesses of other competitive codes and their associated groups. We use this opportunity to briefly discuss the rich computational heritage of the CCSNe community. The first 3D CCSNe codes date back to the gray, smooth particle hydrodynamics code SN-SPH (Fryer & Warren 2002, 2004; Fryer et al. 2006). CCSNe codes have improved since, in particular in their treatment of neutrino transport. Early simulations used lightbulb heating (originally in Bethe-Hydro Murphy & Burrows 2008, subsequently in Nordhaus et al. 2010; Hanke et al. 2012; Handy et al. 2014), which assumes analytic approximations of neutrino heating and cooling rates and has seen use in codes like CASTRO (Zhang et al. 2013; Burrows et al. 2012). This was in part superseded by leakage schemes (originally used with GR1D, O'Connor & Ott 2010, 2011, 2013; Ott et al. 2013, where an approximate optical depth is calculated to determine how much luminosity "leaks" out (Ruffert et al. 1996; Rosswog & Liebendörfer 2003). Advanced spectral leakage (Perego et al. 2016), which solves leakage with the addition of spectral dependence, has seen a recent revival (Gizzi et al. 2019). We also mention the isotropic diffuse source approximation (IDSA), which treats distinctly neutrinos in optically thick and optically thin regimes, and interpolates between the two, such as ELEPHANT (Liebendörfer et al. 2009), 3DSNe-IDSA (Kotake et al. 2018, no 3D simulations to date), and SPHYNX (Cabezón et al. 2017, 2018). In the discussion below, we neglect such simplified schemes within the context of the current competitive CCSNe landscape, and we expect significant differences when compared to higher-fidelity closure

schemes (Pan et al. 2019). Rather, we discuss exclusively codes with 3D capabilities using sophisticated neutrino transport and detailed neutrino microphysics, albeit with differing rad/hydro implementations.

PROMETHEUS-VERTEX (Fryxell et al. 1991; Rampp & Janka 2002) is a multi-group CCSNe code employed by the Garching group (Hanke et al. 2013; Tamborra et al. 2014b; Melson et al. 2015a,b; Summa et al. 2018) with detailed microphysics, including inelastic scattering of neutrinos off electrons and nucleons, on a spherical grid with approximate general-relativistic corrections and velocity redshifts. Prometheus-VERTEX includes neutrino-neutrino pair conversions, which nonetheless is sub-dominant for energy transport relative to the absorption and scattering. VERTEX solves for neutrino transport using a variable Eddington factor to close the moment equations, and extends to multiple dimensions with the ray-by-ray approximation, discussed subsequently. The inner core ($\sim$1.6 km) is evolved in 1D, and the simulation fidelity is limited by the ray-by-ray approach to neutrino transport, which has clear axial artifacts that abet explosion in 2D (the effect of ray-by-ray in 3D is yet unclear). Nuclear burning is approximated by the "flash" method (Rampp & Janka 2002), where an element in a given cell is instantaneously converted to its final product if the cell temperature is above the requisite reaction temperature.

More recently, the Garching group has published 3D CCSNe studies with a new code, AENUS-ALCAR, (Obergaulinger 2008; Just et al. 2015; Glas et al. 2018, 2019) that employs M1 closure instead of the ray-by-ray approximation. AENUS-ALCAR includes detailed neutrino microphysics, including inelastic neutrino scattering, and M1 closure for neutrino transport, with velocity dependent terms and GR corrections. The inner core is again evolved in spherical symmetry. However, their high-resolution 3D runs (Glas et al. 2019) are still coarser than the resolution of our standard 3D runs.

COCONUT-FMT (fast multi-group transport, Müller et al. 2010; Müller & Janka 2015) is a conformal GR (albeit with a spherically symmetric, stationary spacetime metric) multi-group CCSNe code. The code neglects velocity-dependence and inelastic neutrino scattering (the energy bins are decoupled), using simplified neutrino transport based on a stationary two-stream solution with the ray-by-ray approximation. COCONUT-FMT is also limited by its simplified neutrino microphysics, neglecting, for instance, elastic scattering of neutrino off electrons, electron-positron pair annihilation, and inelastic neutrino scattering (Müller 2015; Müller et al. 2017; Müller 2019). Further, bremsstrahlung rates are approximated with a one particle rate (the code only handles single neutrino reactions for elastic scattering). Neutrino transport is treated with a two-stream solution at high optical depths fit to a flux factor, from variable Eddington closure, at lower optical depths. The neutron star core is treated as spherically symmetric, where convection is approximated with mixing length theory. Because the code ignores neutrino-electron scattering, important on infall, it assumes an approximate deleptonization scheme in the core. For nuclear burning, COCONUT-FMT follows the "flash" treatment used by the Garching group. In recent work, Müller et al. (2017), evolved an 18-$M_\odot$ progenitor in 3D, starting pre-collapse, to an impressive 2.5 seconds postbounce, abetted in large part by its simplified neutrino solver.

CHIMERA (Bruenn et al. 2018) is a multi-group CCSNe code employed by the OakRidge group. The code solves for four coupled species of neutrinos (ν_e, $\bar{\nu}_e$, ν_μ, and $\bar{\nu}_\mu$) on a spherical grid using multi-group flux-limited diffusion (akin to a one-moment closure, Bruenn 1985) in the ray-by-ray approximation with velocity redshifts and approximate GR corrections. CHIMERA incorporates a detailed set of microphysics, including inelastic neutrino scattering off electrons and nucleons, and uses the XNET nuclear network (Hix & Thielemann 1999). The inner core ($6-10$ km, depending on

post-bounce time) is evolved entirely in spherical symmetry. Their only published 3D simulation to date (of a 15-$M_\odot$ progenitor), Lentz et al. 2015) explodes.

Kuroda et al. (2016b) developed a multi-group AMR CCSNe code, fGR1, with full GR and M1 closure for neutrino transport with detailed neutrino microphysics, including inelastic scattering. They solve on a Cartesian box with nine layers of refinement. Though they have multi-group capabilities, all but their most recent simulation (collapse to a black hole of a 70-$M_\odot$ Kuroda et al. 2017) assumes energy-independent neutrino transport.

Einstein-ZELMANI is a full GR multi-group CCSNe employed by the Caltech group (Roberts et al. 2016; Ott et al. 2018; Schneider et al. 2019). The code uses M1 closure (with the Minerbo closure, Minerbo 1978) on a Cartesian adaptive-mesh refinement (AMR) grid with eight levels of refinement. It does not, however, allow for inelastic scattering, include velocity-dependence in its neutrino transport, nor enforce lepton conservation by design.

FLASH (Fryxell et al. 2000) is a multi-group CCSNe code that employs M1 closure on an AMR grid. It uses approximate GR and neglects inelastic neutrino scattering processes in their 3D simulation, though they have inelastic scattering capabilities for neutrinos off electrons. In their recent 3D simulations, full velocity and redshift dependence of the neutrino transport is included only in their low-resolution simulation (O'Connor & Couch 2018a). They find no explosion of their 20-$M_\odot$ progenitor.

The ray-by-ray plus (rbrp, e.g. Hanke et al. 2013) approach is distinguished from the ray-by-ray (rbr, originally Burrows et al. 1995) approach by the inclusion of lateral neutrino advection by matter and of neutrino contribution to the lateral pressure gradient in the core. We emphasize that the ray-by-ray approximation reduces neutrino transport to multiple 1D solutions along different radial rays, with the specific intensity azimuthally symmetric around each radial direction. The ray-by-ray approximation lacks lateral neutrino transport. By contrast, a closure scheme obtains

successive angular moments of the Boltzmann transport equation, which is integrated to form a hierarchy of moments of the specific intensity. In M1 closure, the zeroth (energy) and first (flux vector) moments are closed by an analytic expression of the second (pressure tensor) and third (heat tensor) moments. More recent efforts (Nagakura et al. 2019c) have developed simulation capabilities in full phase space (3 in physical space and 3 in momentum space, see also Brandt et al. 2011; Abdikamalov et al. 2012; Richers et al. 2017; Nagakura et al. 2018 for multi-angle CCSNe simulations).

CCSNe simulations are further complicated by additional differences in physical setup, including the implementation of neutrino opacities and nuclear equation of state, neither of which are perfectly understood (Tews et al. 2017; Roberts & Reddy 2017) with different grid and neutrino-energy resolutions. In addition to physical differences in setup, seemingly unimportant computational details, such as the specific super-computing cluster used, the choice of compiler, the computational modules and environment, the choice of optimization flags, can all causes differences in simulation results. Differences in progenitor models for the same stellar mass between different stellar evolution groups, and even by the same group over various iterations (Woosley & Heger 2007; Sukhbold et al. 2016, 2018), add additional uncertainty. Fortunately, these worries are tempered in a recent code-comparison study (O'Connor et al. 2018), where many of the above-mentioned groups performed an independent, blind comparison of their simulation results of the evolution in spherical symmetry of a 20-$M_\odot$ progenitor. The CCSNe community can find solace in that the results were surprisingly similar, albeit in spherical symmetry, given the different implementation of the same neutrino physics and different rad/hydro solvers implemented by each group.

However, multidimensional simulations are more sensitive to code fidelity due to the complicated nature of turbulent flow. As such, we identify a metric for code competitiveness on the basis of detailed neutrino transport (via M1 closure) and neutrino

microphysics, in particular the inclusion of non-isoenergetic (inelastic) neutrino scattering, processes. To date, FORNAX is the only multi-dimensional supernova code which employs M1 closure (and not ray-by-ray) with a detailed suite of neutrino microphysics, including the many-body effect and inelastic neutrino scattering off electrons and nucleons, with approximate GR with velocity- and redshift-dependent neutrino transport. It has the additional advantage of excellent scaling: its static mesh refinement avoids spherical coordinate singularities, and its explicit neutrino transport allows for scaling to hundreds of thousands of cores. This advantage has allowed us to produce over twenty 3D simulations over the last year − more than all other competitive groups combined − with over ten already published.

I identify in Chapter 2 important microphysics which can qualitatively alter explosion outcome. In Chapter 3, I identify the compounded role of neutrino microphysics with progenitor profile, macrophysical perturbations, and possible stellar rotation on promoting successful stellar explosion in a series of axisymmetric simulations. The presence of a sharp Silicon-Oxygen interface at $\sim$1.5-$M_\odot$ is potentially critical to shock revival. In Chapter 4, I extend the study to the successful explosion of a 16-$M_\odot$ progenitor and review its explosion diagnostics. Finally, in Chapter 5, I extend the 3D study to 11 progenitors all evolved in 3D to identify CCSNe neutrino and gravitational wave signatures, detectable by next-generation instrumentation, and their correlations with the dynamics of the inner CCSNe core. I summarize my work and comment on future directions for the community in Sec 6. The driving question, and the subject of this thesis, is to identify the aspects of CCSNe physics integral to explosion outcome.

Chapter 2

Neutrino Microphysics in CCNSe

2.1 Introduction

In this Chapter, we briefly highlight the recent advances in neutrino microphysics and their significant impact on the study of CCSNe. We pay special attention to the differential neutrino-nucleon scattering cross section, which to lowest order in $\frac{\epsilon}{M}$ (assuming a neutron medium for simplification) is

$$\frac{d\sigma_0}{d\Omega} = \frac{G_F^2 \epsilon^2}{4\pi^2}[C_V^2(1+\cos\theta)S_V + C_A^2(3-\cos\theta)S_A]\,, \tag{2.1}$$

where G_F is the Fermi constant, ϵ is the neutrino energy, M is the nucleon mass, θ is the scattering angle, C_V is the vector coupling constant, and C_A the axial-vector coupling constant. The coupling constants differ between neutrons and proton. S_A and S_V are structure factors that determine the response of the system to medium spin and density fluctuations, respectively, and asymptote to zero at low densities. This simplified expression neglects, e.g., the weak magnetism correction, which scales as $\frac{\epsilon}{M}$, and is important at high neutrino energies. These corrections are included, however, in Fornax, and this simplified expression serves to highlight several points of note. First, the differential neutrino-nucleon scattering cross section scales as the neutrino

energy squared. Second, ambient structure factor corrections (Horowitz et al. 2017; Burrows & Sawyer 1998) modify the scattering cross section. Third, the axial-vector component, all else being equal, provides a larger contribution to the scattering cross section because of the multiplicative factor of three.

I perform two-dimensional axisymmetric simulations using FORNAX with progenitors from Woosley & Heger (2007) to study the sensitivity of explosion outcome on neutrino microphysics. We present a study of the 16- and 20-$M_\odot$ progenitors (Woosley & Heger 2007) employing the SFHo equation of state (Steiner et al. 2013 unless otherwise noted. We introduce physically motivated pre-collapse convective velocity perturbations for certain simulations noted below. For these, the maximum perturbation speed on the grid is set to 1000 km s^{-1}, which as indicated earlier may be near or beyond the expected upper end of the range, a spherical harmonic index l of 2, and a radial quantum number n of 5, following the formalism of Müller & Janka (2015).

In § 2.2, we identify the effect of the many-body correction and nucleon recoil through inelastic neutrino scattering off nucleons and neutrino energy transport and successful stellar explosion. We briefly discuss equation-of-state effects and the shortcomings of the ray-by-ray approximation. In § 2.3, we look at shortcomings of existing parameterizations of explosion outcomes. We summarize the results in § 2.4.

2.2 Microphysics

In Fig. 2.1, we summarize the effects of changes to neutrino microphysics on explosion outcome on the evolution of a 16-$M_\odot$ progenitor. Our default run, which includes both inelastic scattering (off electrons and nucleons) as well as the many-body (MB) correction explodes at ∼150 ms, indicated by the rapid shock acceleration. Removing either (or both) inelastic scattering and MB effects results in a stalled shock and

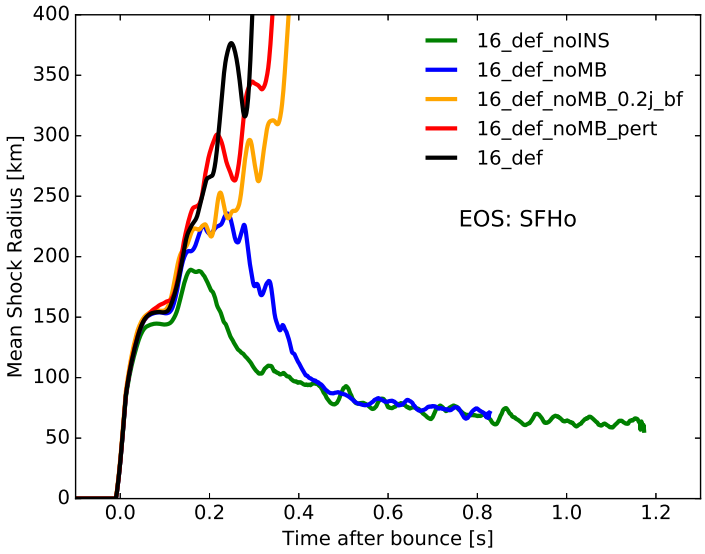

Figure 2.1: Shock radii (in km) versus time post-bounce (in s) for variations on the default 16-$M_\odot$ progenitor. Default model "def" refers to inclusion of inelastic scattering off both electrons (IES) and nucleons (INS), as well as the inclusion of the Horowitz et al. (2017) many-body correction (MB). This model explodes at ∼250 ms post-bounce. I then remove and add certain inputs, denoted by a subscript with "def". Removing either the many-body correction (blue, "16_def_noMB") or inelastic scattering off nucleons (green, "16_def_noINS") leads to a dud. However, even without the many-body correction (noMB), modifying the opacity table to include Fischer's correction (Fischer 2016) to the nucleon-nucleon bremsstrahlung rate ("bf") and only 20% of the electron capture rate (Juodagalvis et al. 2010) on heavy nuclei (orange, "0.2j"), leads to an explosion ∼50 and ∼100 ms, respectively, after our default model. This helps illustrate the sensitive dependence of the outcome − explosion or dud − on the microphysical inputs when near criticality.

failed explosion. Adding either moderate velocity perturbations to the failed model, without the MB corrections, or adding Fischer's correction (Fischer 2016) to the nucleon-nucleon bremsstrahlung rate with a reduced electron capture rate on nuclei during infall revives the stalled shock into an explosion. Neutrino microphysics are crucial to the explosion outcome. However, even in the case of a failed explosion in our simulations, incorporating physical changes to either the progenitor structure (see Chapter 3) or to the detailed microphysics, within the range of uncertainty can, promote explosion.

A reduced electron capture rate on nuclei during infall (Juodagalvis et al. 2010) reduces core deleptonization and maintains a higher electron degeneracy pressure. In the inner region of collapse, this leaves behind a larger protoneutron star, with a more superficial shock. The higher degeneracy pressure also slows collapse, reducing ram pressure ahead of the shock. Both these effects are favorable to shock revival. Similarly, the inclusion of the many-body effect reduces the neutrino-nucleon scattering opacity in the high densities of core, increasing neutrino luminosity losses. This serves to virially compress and heat the core, increasing the resident neutrino energies. Since the neutrino-nucleon scattering cross-section scales as the neutrino energy squared, 2.1, the neutrinos more efficiently deposit energy behind the stalled shock, at lower densities where the many-body effect is no longer significant. The net effect of both inelastic scattering and the many-body correction improve neutrino heating of the stalled mantle and encourage successful stellar explosion.

In Fig. 2.2, we plot the neutrino spectra for the three species studied before (solid) and after (dashed) explosion. We emphasize the comparison between models with (black) and without inelastic scattering (green) and the many-body effect. Prior to explosion, both inelastic scattering and the many-body lead to neutrino upscattering and yield a harder neutrino spectra, favorable to the neutrino-heating mechanism for explosion outcome. After 400 ms, the default model has exploded, ceasing accretion, and hence presents a softer neutrino spectra. Furthermore, in Fig. 2.3, We find that, prior to explosion, inclusion of inelastic scattering off nucleons reduces ν_μ luminosities and RMS energies by $\sim$10%, and slightly increases ν_e and $\bar{\nu}_\mathrm{e}$ luminosities. The RMS energies for the latter are largely unchanged. Müller et al. (2012b) similarly found ν_μ downscattering boosting $\nu_e, \bar{\nu}_e$ neutrino luminosities near their neutrinospheres and upscattering of $\nu_e, \bar{\nu}_e$ luminosities. Inelastic scattering loss to the nucleon medium by ν_μ is compensated for by an increase in $\nu_e, \bar{\nu}_e$ luminsoties. Since ν_μ neutrinos have smaller matter interaction cross sections than $\nu_e, \bar{\nu}_e$, inelastic scattering leads to net

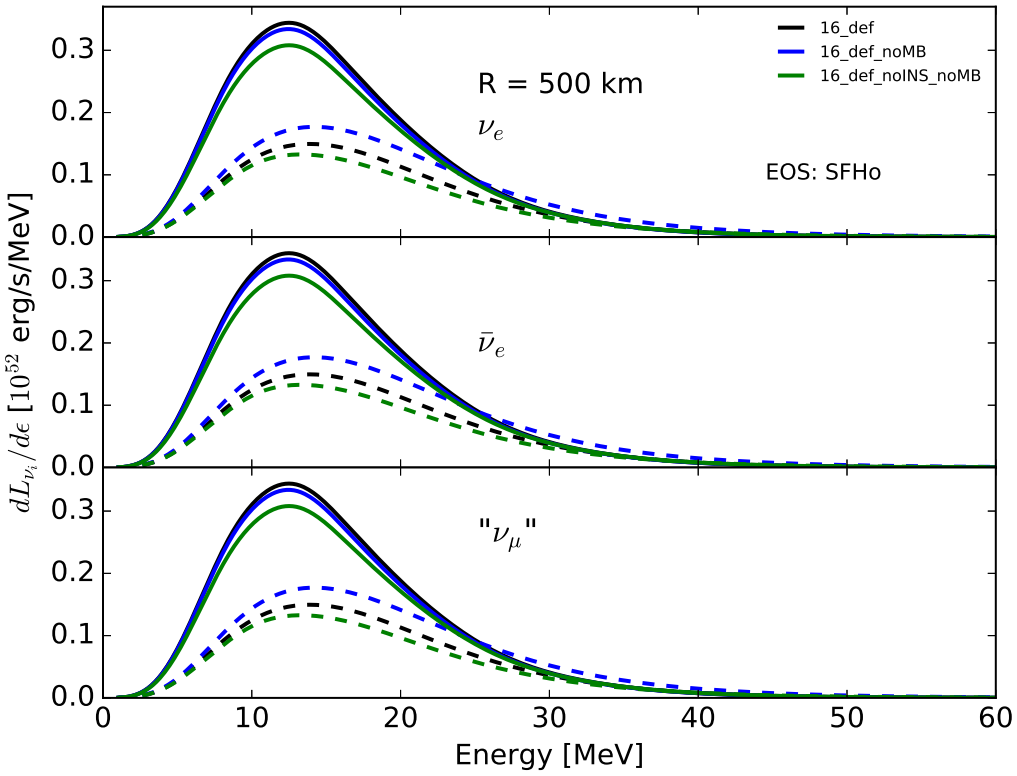

Figure 2.2: The role of inelastic scattering off electrons and nucleons and the neutral-current many-body correction on the emergent spectra (in 10^{52} erg/s/MeV) at 500 km at 100 (solid) and 400 (dashed) ms post-bounce. At early times, prior to explosion, both inelastic scattering off electrons and nucleons and the many-body correction lead to upscattering. At 400 ms, the default model has exploded and hence has a diminished spectrum vis-à-vis the non-exploding model 16_def_noMB.

energy transfer from neutrinos to both electrons and nucleons, improving neutrino heating behind the stalled shock.

2.2.1 Equation of State

We provide a cursory look at equation-of-state (EOS) effects on shock revival. All models include inelastic scattering off electrons and nucleons and the many-body correction, unless otherwise specified. Figure 2.4, left panel, shows a plot of the shock radius as a function of time for the 16-$M_\odot$ progenitor for two different equations of

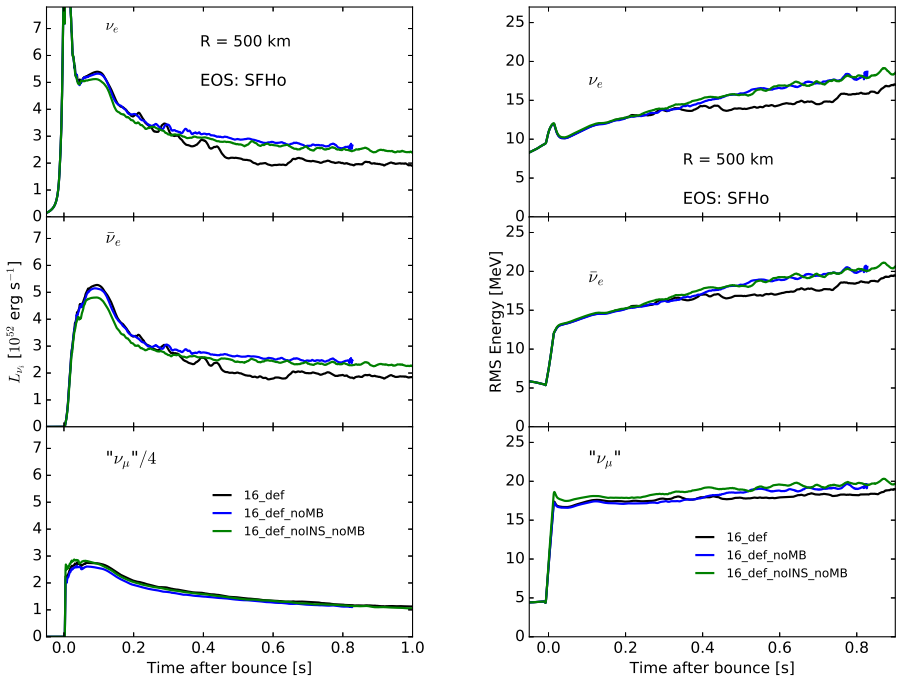

Figure 2.3: Modification due to inelastic scattering off electrons and nucleons of the luminosities (left) and RMS energies (right) of neutrinos at 500 km, redshifted to the lab frame. Including inelastic scattering off nucleons decreases the ν_μ luminosities and RMS energies by $\sim 10\%$, as in Müller et al. (2012b), while slightly increasing the ν_e and $\bar{\nu}_e$ luminosities. RMS energies of the latter are mostly unaffected by inelastic scattering. The default model (black, with many-body corrections and both inelastic scatterings) shows a dip in luminosity and RMS energy after 300 ms post-bounce, the time of its explosion.

state: SFHo (Steiner et al. 2013, and DD2 (Hempel & Schaffner-Bielich 2010). For core temperatures of $\sim$25 MeV and electron fraction Y_e $\sim$0.3, the DD2 equation of state is the stiffer of the two. A careful study of the relationship between equation of state and explosion tendency has not been conducted, but results here indicate that the SFHo equation of state is more conducive to an explosion, all else being equal, for the 16-$M_\odot$ progenitor. Furthermore, although the model with DD2 equation of state does not explode, incorporating the many-body and inelastic neutrino scattering effects discussed produces a shock radius stalled further out by $\sim$70 km. We briefly state that a stiffer equation of state may produce core bounce at lower densities with

a shock radius further out. A softer equation of state will yield a shock buried deeper in, in a more compact core with higher neutrino energies. The latter behaves similar to the inclusion of general-relativistic effects and the many-body effect, both of which also yield a more compact core. However, the reality is much more complicated and no simple conclusion between equation of state and explosion outcome exists. A recent study (Schneider et al. 2019), finds that a higher effective nucleon mass at nuclear densities is more conducive to explosion outcome for a 20-$M_\odot$ progenitor evolved in a 3D octant with ZELMANI.

2.2.2 Ray-by-Ray Approximation

The ray-by-ray approximation (Burrows et al. 1995; Buras et al. 2006) to neutrino transport approximates multi-dimensional transport by solving for the specific intensity along many 1D radial rays and sphericizing the matter distribution. The ray-by-ray plus approach allows for matter advection of neutrinos at high densities and approximates the contribution to lateral pressure by neutrinos, but ray-by-ray in any incarnations neglects lateral transport of neutrinos and as such can lead to spurious results. In the right panel of Fig. 2.4, we plot the shock radius versus time after bounce for the 20 $M_\odot$ progenitor using the LS220 EOS (Lattimer & Swesty 1991), with and without the ray-by-ray plus (rbrp) approximation to neutrino transport used by many groups in multidimensional simulations (see, e.g. Hanke et al. 2013; Melson et al. 2015a; Summa et al. 2016; Bruenn et al. 2016; Müller et al. 2018). Including rbrp leads to an explosion when otherwise there was none. The model with rbrp, both with (blue) and without (green) the many-body effect explodes, albeit $\sim$700 ms later without the many-body effect. The model without rbrp, even with the many-body correction (black) fails to explode, suggesting that the artificial ray-by-ray+ is more significant to explosion than the physical inclusion of the many-body correction. The ray-by-ray approximation artificial promotes explosion when otherwise there may be

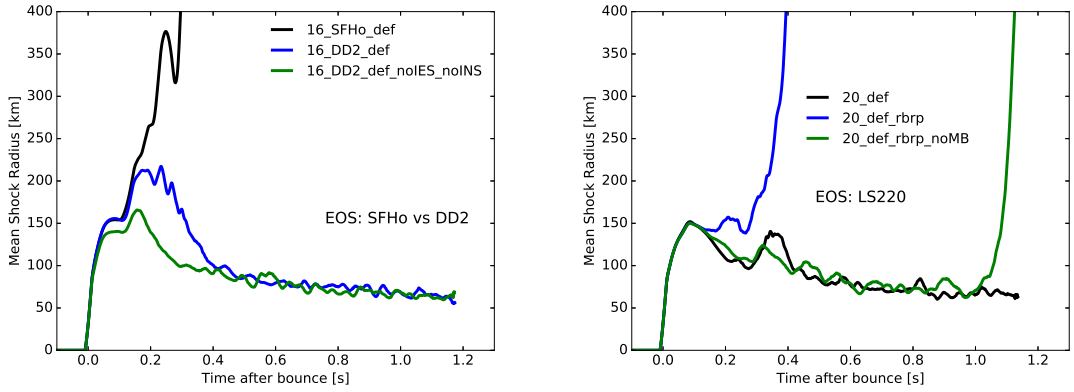

Figure 2.4: **Left**: Shock radii (km) versus time after bounce (s) for the SFHo and DD2 EOS for the $16M_{\odot}$ WH07 progenitor as a function of time after bounce. Only the former (our default model) explodes. We also plot for comparison a model with the DD2 EOS, but without any inelastic scattering off electrons or nucleons. Though neither DD2 model explodes, including inelastic scattering increases the stalled shock radius by ∼70 km. **Right**: Shock radius (km) versus time after bounce (s) for the 20 $M_{\odot}$ WH07 progenitor using the LS220 EOS, with and without the ray-by-ray plus (rbrp) approximation to neutrino transport. All models include inelastic scattering off electrons and nucleons. Including ray-by-ray+ (rbrp) leads to an explosion when otherwise there was none. The model with ray-by-ray+ and without many-body (green) explodes as well, though 700 ms after the model with ray-by-ray+ and many-body, suggesting that the ray-by-ray+, though artificial, is more significant to explosion than the physical inclusion of the many-body correction.

none (Dolence et al. 2015; Skinner et al. 2016; Glas et al. 2019), and emphasizes the need for high-fidelity neutrino transport, currently M1 closure (e.g. Skinner et al. 2016; Roberts et al. 2016), in CCSNe simulations. The results are most problematic in 2D axisymmetric simulations, where there is a preferred explosion axis, though the artifacts of ray-by-ray in 3D remain to be determined.

2.3 Compactness

The compactness parameter (O'Connor & Ott 2011, 2013) has often been used as a proxy for explosion in the supernova context. Compactness is a local parameter obtained by simply dividing the enclosed stellar mass for a given mass cut divided by the radius for that cut, akin to a pseudo-potential. There is no reason to expect that a

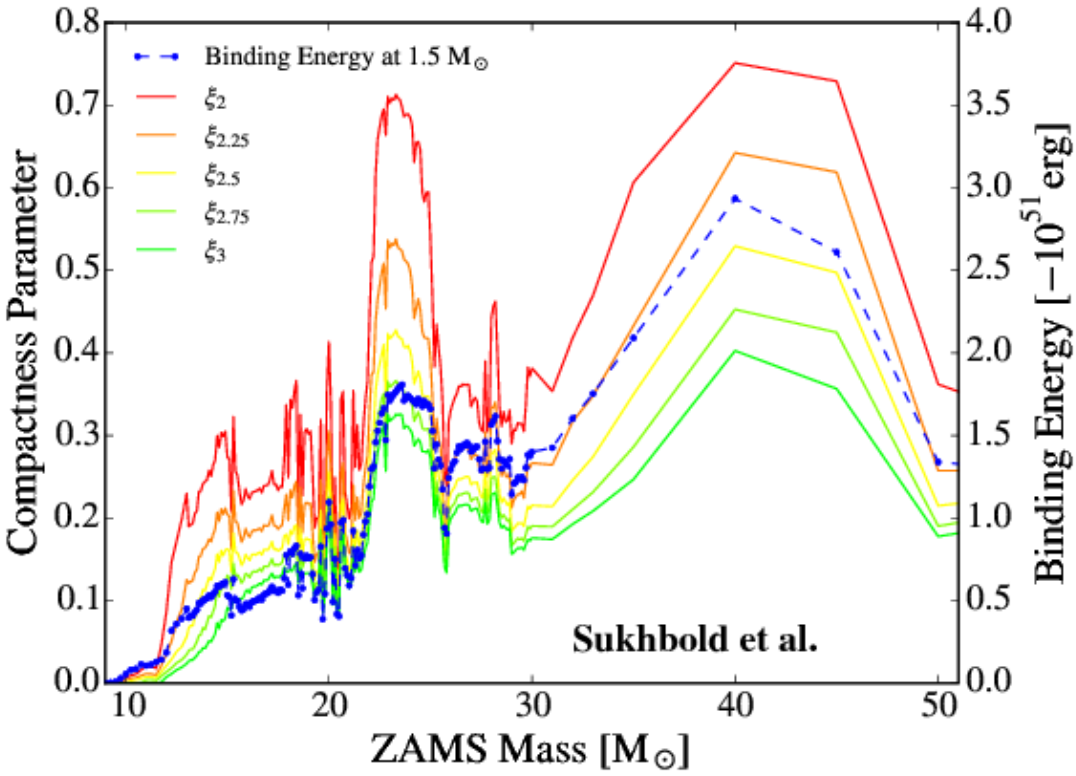

Figure 2.5: This plot depicts the dependence of the compactness parameter O'Connor & Ott 2011, 2013), calculated at various interior masses, versus progenitor ZAMS mass (using Sukhbold et al. 2016, though the same trend exists for Woosley & Heger 2007), as well as the corresponding envelope binding energy (blue dots; in Bethes [10^{51} ergs]) for a baryon mass cut of 1.5 $M_\odot$. As this figure shows, whatever the position at which compactness is defined, it correlates extremely well with envelope binding energy. It is our contention that it is the latter quantity that is more germane to the outcome of core collapse.

single local parameter can predict the outcome of a supernova, and we emphasize that compactness does not correlate with explosion outcome (e.g. Burrows et al. 2019). However, we illustrate in Fig. 2.5 the strong correlation between compactness and the more physical envelope binding energy, exterior to 1.5 $M_\odot$, for a series of progenitors from 10−40 $M_\odot$ (Sukhbold et al. 2016, also Woosley & Heger 2007). If the stalled shock is successfully revived, the stellar envelope gravitational binding energy sets an approximate physical condition to fully explode a star and is more pertinent to explosion outcome, on second timescales. Shock revival happens more immediately, on hundreds of milliseconds timescales. We discuss in subsequent Chapters the im-

portance of a pronounced Silicon-Oxygen interface as a possible metric for successful shock revival.

2.4 Conclusion

In this Chapter, we presented recent developments in neutrino microphysics, namely the many-body correction to neutrino-nucleon scattering and inelastic neutrino scattering off electrons and nucleons. Both effects are found to be favorable to shock revival, and emphasize the critical dependence on explosion outcome on detailed microphysics. We do not yet include the vector component of the many-body effect, which is expected to be subdominant, nor the contribution of medium effects on charged-current reactions, for which a suitably calculated fit does not yet exist, nor self-consistent treatment of the equation of state with the neutrino opacities (Roberts & Reddy 2017; Nagakura et al. 2019b). We also briefly discussed the yet-ambiguous equation of state dependence on shock revival, and commented on the inadequacies of using parameterized relations, such as compactness, to predict explosion outcome. In the following Chapters, we will present results using this microphysical setup in multi-dimensional simulations, both in 2D (Chapter 3), and in 3D (Chapter 4, 5).

Chapter 3

CCSNe in 2D: Exploring the Explosion Mechanism

3.1 Introduction

For over fifty years, since neutrinos were proposed by Colgate & White (1966) as critical to core-collapse supernovae, simulations have attempted, often unsuccessfully, to reproduce the robust explosions seen in Nature. Given recent detection of gravitational waves from compact mergers (Abbott et al. 2016a; Abbott et al. 2017), simultaneous detection of electromagnetic radiation, a neutrino signature (Ott et al. 2012), and gravitational waves from supernovae (Ott 2009; Müller et al. 2013; Cerdá-Durán et al. 2013; Kotake 2013; Kuroda et al. 2016a) represents a yet unbreached frontier and a probe of three of the four fundamental natural forces. Such observations will be tractable by second and third generator detectors (Yakunin et al. 2015; Andresen et al. 2017) and allow constraints on the explosion mechanism, progenitor mass, and equation of state (Morozova et al. 2018b). Improvements over the years in understanding the multitude of microphysical interactions and in the capabilities of

multi-dimensional simulations have combined together to improve our understanding of this central phenomenon.

Using the CHIMERA code, the Oak Ridge group (Bruenn et al. 2013; Bruenn et al. 2016) found explosions for the 12-, 15-, 20-, and 25-$M_\odot$ progenitors from Woosley & Heger 2007 (henceforth, WH07), all roughly at the same post-bounce time and without the shock radius stalling. Employing PROMETHEUS-VERTEX, Summa et al. (2016) found later explosions over a spread of explosion times for the same four progenitors and 14 additional progenitors in the 11-28 $M_\odot$ mass range, from Woosley et al. (2002). Both approaches use a ray-by-ray approach of multiple one-dimensional solutions to approximate multi-dimensional neutrino transport and include inelastic scattering of neutrinos off nucleons and electrons. However, earlier studies suggest that the ray-by-ray approach introduces axial artifacts and exaggerates anisotropies (Ott et al. 2006, Skinner et al. 2016, Dolence et al. 2015, Burrows et al. 2018) which may artificially promote explosion, at least in two dimensions. Recently updated results for the same progenitors by O'Connor & Couch (2018b) found explosions for all but the 12-$M_\odot$ progenitor using an M1 closure scheme for neutrino transport rather than the ray-by-ray approximation, but ignoring inelastic neutrino scattering processes. All their explosions were significantly delayed relative to Summa et al. (2016) (490 ms for the 15-$M_\odot$ model, 500 ms for the 20-$M_\odot$ model, and 270 ms for the 25-$M_\odot$ model). Though, O'Connor & Couch (2018b) found earlier explosions by 100-150 ms by correcting for inelastic neutrino scattering, this is insufficient to explain the delayed explosions using M1 transport rather than ray-by-ray. The lack of explosion for the 12-$M_\odot$ progenitor, and significantly delayed explosions for the remaining three models, buttress our argument that the ray-by-ray approach either allows an explosion where there would have been none, or accelerates the time of explosion, at least in 2D. The potential artifacts of the ray-by-ray approach in three dimensions remain unclear.

Abdikamalov et al. (2016) (see also Radice et al. 2018) found that late nuclear shell burning produces strong turbulent convection, which promotes supernova explosion. These results were iterated in 3D by various groups (see below). More recently, using the M1 closure for multi-dimensional neutrino transport, O'Connor & Couch (2018b) found 2D explosions abetted by using a general relativistic rather than Newtonian treatment of gravity. Bollig et al. (2017) find that muon creation at the high temperatures in proto-neutron stars facilitates explosion in 2D. Thus, an interplay of turbulence, microphysics, and a proper treatment of gravity have been historically critical in producing supernovae explosions in two dimensions.

3D simulations have evolved in the decade since the early foray by Fryer & Warren (2002) using a grey scheme for neutrino transport. Using PROMETHEUS-VERTEX, Melson et al. (2015b) found that the 9.6-M$\odot$ progenitor explodes in 3D with faster shock expansion than in 2D. Melson et al. (2015a) found also explosion for a 20-$M_\odot$ progenitor, but only with a strangeness correction to the axial-vector coupling constant which may be too large to be physical (see Ahmed et al. 2012, Green et al. 2017). Using ZEUS-MP and omitting heavy neutrinos, Takiwaki et al. (2012) explode their 11.2-$M_\odot$ progenitor in 3D on a low-resolution grid with the IDSA scheme and the ray-by-ray approach to solve for multi-dimensional neutrino transport. Comparing to 2D, 3D resulted in increased neutrino dwell time in the gain region and more violent convection, but also increased neutrino cooling. Updating the IDSA scheme, including a leakage scheme for heavy neutrinos, and quadrupling the ϕ resolution, Takiwaki et al. (2014) identified shock revival for all models, with delayed explosion at higher resolution and more robust explosions in 2D than 3D. More recently, the Garching group studied the 15-$M_\odot$ WH07 progenitor with various rotation models (Summa et al. 2018). They concluded that rapid rotation inhibits explosion in 2D but promotes it in 3D, citing the development of a SASI mode that compensates for reduced neutrino heating due to rotation. Notably, explosion set in shortly after the accretion

of the Si/O interface. Using FLASH, Couch & Ott (2013) produced explosions in 3D for their 15-$M_\odot$ progenitor when introducing perturbations to angular velocities. Such perturbations increased turbulent ram pressure (Couch & Ott 2015), mediating explosion. Müller et al. (2017) also presented the first simulations of the final minutes of iron core evolution in 3D, finding that asphericities in 3D progenitor structure enhance post-shock turbulence. Using COCONUT-FMT, Müller et al. (2017) similarly found their 18-$M_\odot$ model to explode when the progenitor is allowed to evolve in 3D for the final five minutes of oxygen burning. More generally, some past multi-group 3D simulations either did not explode (Hanke et al. 2013; Tamborra et al. 2014a), or exploded later than 2D counterparts (Couch 2013) more recent simulations suggest that 3D progenitors are only slightly less explosive (Roberts et al. 2016; Lentz et al. 2015; see review by Müller 2016).

In Burrows et al. (2018), we presented results of 2D simulations toggling a variety of physical processes, particularly inelastic neutrino scattering off electrons and nucleons and the many-body correction to neutrino-nucleon scattering opacities (Horowitz et al. 2017). We found that the results, particularly whether or not a model exploded, were sensitive to small changes in microphysics when near criticality for explosion. O'Connor et al. (2017) emphasized these results that explosion is sensitive to the many-body effect, with changes to the neutral-current scattering cross section at the 10-20% level at densities above 10^{12} g cm^{-3} pushing all their models from 12-25 $M_\odot$ to explode.

Here, we present the comprehensive results of a series of 2D radiation/hydro simulations using FORNAX of a suite of nine progenitors spanning 12 to 25 $M_\odot$ performed on a grid extending out to 20,000 km. Our key findings are that four of our progenitors explode with the inclusion of inelastic scattering processes off electrons and nucleons as well as with the many-body correction to neutrino-nucleon scattering opacities. We show that the non-exploding models can also be nudged to explosion with the

inclusion of additional physical inputs, such as modest rotation and perturbations to infall velocities.

In § 3.2, we introduce the numerical methods and setup for our simulations. In § 3.3, we remark on basic diagnostics of our results and explore the role of the Si/O interface accretion in explosion outcome. We expand these diagnostics in § 3.4, where we look at explosion energies and probe properties in the gain region. We also focus on a study of microphysical and macrophysical inputs, as well as progenitor dependence, illustrating that all models considered can explode with changes to opacities, moderate rotation and/or perturbations to infall velocities. We further explore the electron-fraction distribution of the ejecta mass for the exploding models, and look for evidence for the Lepton-number Emission Self-Sustained Asymmetry (LESA) but find none. In S 3.5, we comment on the properties of the resulting neutron stars. We compare our 2D and 1D simulations in § 3.6. Finally, we summarize our results and present our conclusions in § 3.7.

3.2 Progenitors and Setup

We consider nine progenitors from Woosley & Heger (2007) spanning 12 to 25 $M_{\odot}$. Their density profiles are illustrated in the left panel of Fig. 3.1. We evolve these models in two dimensions out to 20,000 km, until the maximum shock radius reaches the grid boundary, using FORNAX, a new multi-dimension, multi-group radiation/hydrodynamic code developed to study core-collapse supernovae (Wallace et al. 2016; Skinner et al. 2016, Burrows et al. 2018; Skinner et. al 2018, in prep.). FORNAX solves the comoving-frame velocity dependent transport equations to order O(v/c). The hydrodynamics uses a directionally-unsplit Godunov-type finite-volume scheme and computes fluxes at cell faces using an HLLC Riemann solver. It employs a dendritic grid that deresolves at small radii to overcome CFL limitations in evolu-

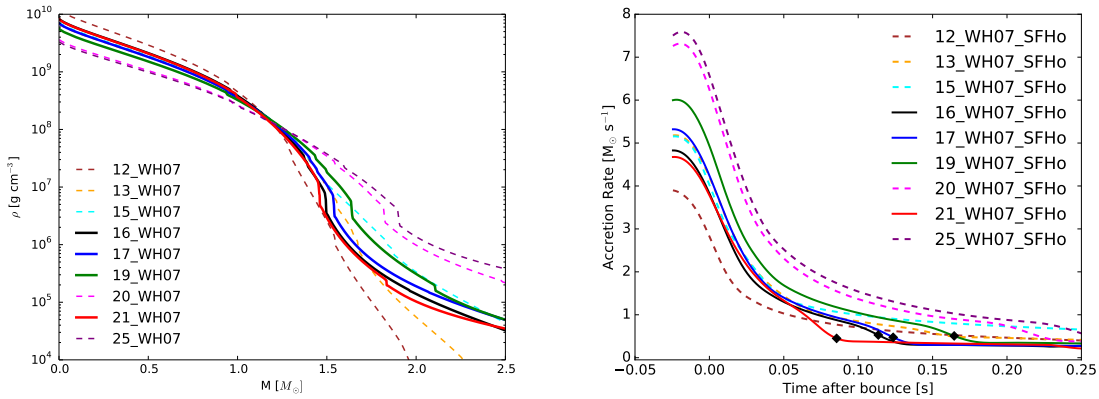

Figure 3.1: **Left panel:** Initial density profiles (in g cm^{-3}) against enclosed mass (in $M_\odot$) for the nine progenitors (12-, 13-, 15-, 16-, 17-, 19-, 20-, 21-, and 25-$M_\odot$) taken from Woosley & Heger (2007). We find that four of the nine benchmark models (including inelastic scattering off electrons and nucleons together with the many-body correction) explode, and their density profiles are illustrated in thick solid lines. The remaining five density profiles (dashed) correspond to non-exploding benchmark models. The exploding models have pronounced Si/O interfaces interior to 1.7 $M_\odot$ as seen by the sharp density drop-off at several $\times$ 10^6 g cm^{-3}. These models have steeper density gradients interior to the interface and shallower profiles exterior, which we argue promotes explosion. **Right panel:** Accretion rates (in $M_\odot$ s^{-1}) at 500 km for the six WH07 progenitors plotted against time (in seconds) after bounce. The majority of the models sustain accretion rates of over 1 $M_\odot$ s^{-1} for the first 300 ms. Note the approximate order of increasing accretion rate with progenitor mass for the non-exploding models (dashed). The accretion rates plummet over a spread of 150 ms for the various progenitors, similar to the spread in explosion times. All exploding models (solid, with explosion times marked with black diamonds) feature an early dip in accretion rate that corresponds to accretion of the Si/O interface and, subsequently, to explosion (see Fig. 3.3); note that the exploding models with Si/O interfaces further interior in mass (**left**) are the first to dip in accretion (**right**).

tion time while approximately preserving cell size and shapes to keep the timestep independent of resolution. Our default resolution is 608 radial cells by 256 angular cells. The radial grid extends out to 20,000 km and is spaced evenly with Δr $\sim$0.5 km for r $\leq$ 50 km and logarithmically for r $\geq$ 50 km, with a smooth transition between. The angular grid resolution varies smoothly from $\sim$0.95° at the poles to $\sim$0.65° at the equator. For this project, we use a monopole approximation for gravity. We include an approximate general relativistic term following Marek et al. (2006) and employ the SFHo equation of state (Steiner et al. 2013) which is consistent with all currently known nuclear constraints (Tews et al. 2017).

We solve for radiation transfer using the M1 closure scheme for the second and third moments of the radiation fields (Vaytet et al. 2011). We follow three species of neutrinos: electron-type, anti-electron-type, and treat the heavy neutrinos as a single species, "ν_μ." We use 20 energy groups spaced logarithmically between 1 and 300 MeV for electron neutrinos and to 100 MeV for anti-electron- and "ν_μ"-neutrinos.

We follow the notation of Burrows et al. (2018) for our progenitors, with IES_INS_MB indicating inelastic scattering of neutrinos off electrons (IES) and nucleons (INS) and the many-body (MB) correction to the neutrino-nucleon opacities. The neutrino-matter interactions follow Burrows et al. (2006), with inelastic neutrino-nucleon scattering incorporated using a modified version of Thompson et al. (2003). For a more detailed discussion of the numerical methods employed by Fornax, see Wallace et al. (2016); Radice et al. (2017); Burrows et al. (2018); Skinner et al. (2019).

3.3 Explosion Dynamics

We present results that the progenitor structure is crucial in determining explosion outcome for our model suite of simulations. In Fig. 3.1, right panel, we illustrate the

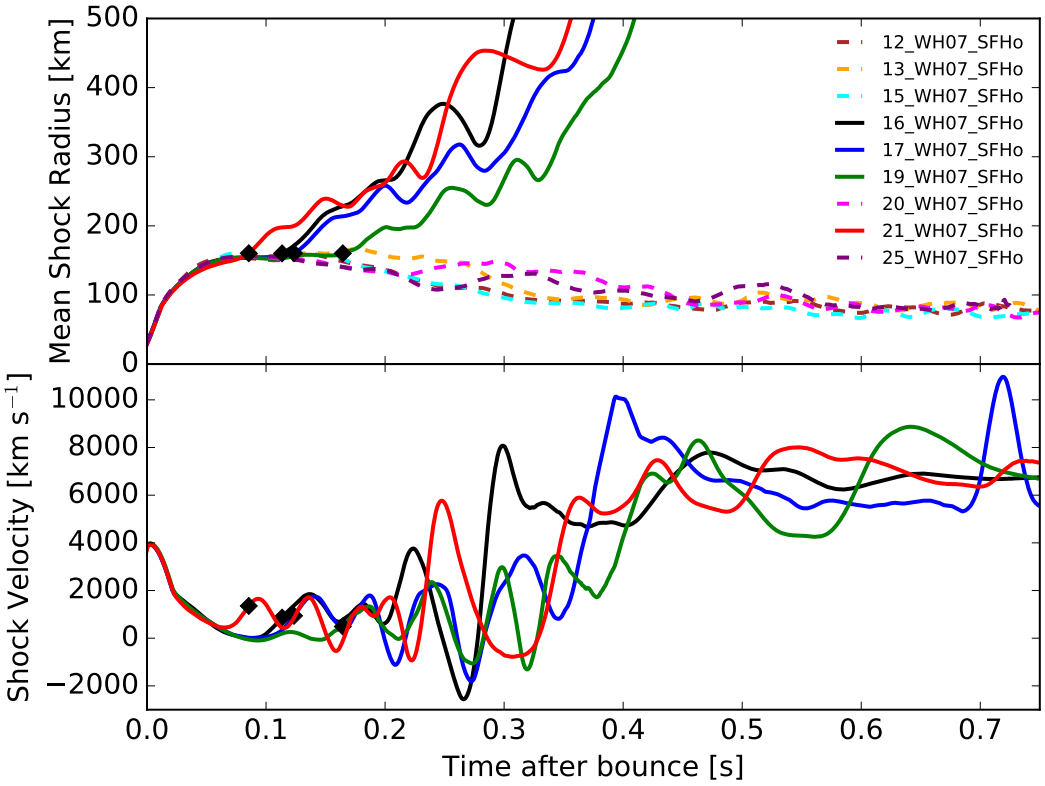

Figure 3.2: **Top panel**: Plotted are the mean shock radii (in kilometers) for our 2D simulations of the 12-, 13-, 15-, 16-, 17-, 19-, 20-, 21-, and 25-$M_\odot$ progenitors (Woosley & Heger 2007) as a function of time (in seconds) after bounce. Exploding models are illustrated in solid, and non-exploding models in dashed. The shock radii evolve almost identically until ∼100 ms after bounce. We see no monotonic correlation with progenitor mass and explosion. However, we note the correlation between the position of the Si/O interfaces in Fig. 3.1 and explosion times. Interfaces located deeper in the progenitor correspond to earlier explosions, with explosion order of 21-, 16-, 17-, and 19-$M_\odot$, suggesting that earlier accretion of these interfaces prompts earlier explosion. **Bottom panel**: We plot average shock velocities as a function of time (in seconds) after bounce. Note that the shock is moving outwards at early times, accumulating mass and decreasing in velocity until 100 ms. The 25-$M_\odot$ progenitor (not shown) has the largest shock velocity early on, peaking at over 20,000 km s^{-1}, roughly 6% the speed of light. At late times, all shock velocities asymptote to approximately 10,000 km s^{-1}. This figure is smoothed using a running time average of 10 ms.

accretion rates (in $M_\odot$ s^{-1}) as a function of time after bounce (in seconds) at 500 km for the first several hundred milliseconds post-bounce. In the top panel of Fig. 3.2, we illustrate the mean shock radii (in km) and the shock velocity (km s^{-1}) as a function of time after bounce (in seconds) in the top and bottom panels, respectively, for our suite of nine WH07 progenitors from 12 to 25 $M_\odot$. Explosion times, defined as when the mean shock radius reaches 160 km after passing an inflection point, are indicated subsequently in our figures as black diamonds. The explosion times are non-monotonic with progenitor mass and have a spread of approximately 100 ms for the various explosions. The mean shock radii evolve almost identically until 100 ms post-bounce, then continue to rise without stalling for all our exploding models. Models 16-, 17-, 19- and 21- $M_\odot$ all explode, with the heaviest, the 21 $M_\odot$ model exploding first. These four have not been the focus of previous studies in recent simulations. Both Bruenn et al. (2016) (see also their Paper 1, Bruenn et al. 2013) and Summa et al. (2016) studied the 12-, 15-, 20- and 25-$M_\odot$ WH07 progenitors, finding that all of them explode, but using the ray-by-ray approximation to neutrino transport and the LS220 equation of state (Lattimer & Swesty 1991). We find that none of these models explodes for our default setup, but we show later (Sec. 3.4) that, with moderate macrophysical modifications, all progenitors models can be nudged into explosion. However, using M1 transport rather than ray-by-ray for neutrino transport, O'Connor & Couch (2018b) find delayed explosions for the 15-, 20-, and 25-$M_\odot$ progenitors. There are significant physical differences between our two approaches, including a different analytic closure (Minerbo 1978 vs. Vaytet et al. 2011), a different equation of state (LS220 vs. SFHo), and different energy resolutions (12 vs. 20 energy groups). In particular, the LS220 equation of state has shown to be more explosive than the SFHo (Bollig et al. 2017). Be that as it may, we show in Sec. 3.4 that all progenitors are close to criticality for explosion.

Models 16- and 17-$M_\odot$ explode in short succession of each other, with the 19-$M_\odot$ progenitor exploding last, roughly 50 ms later. As we will discuss in Sec. 3.4, explosion order anti-correlates with explosion energy. In the bottom panel of Fig. 3.2, we plot the mean shock velocity versus time after bounce for the four exploding models. At late times, the shock velocities undulate with no regard to progenitor mass, asymptoting to roughly 7000 km s^{-1} with values as high as 10,000 km s^{-1}, around 0.03 times the velocity of light, c. However, the early rise in velocities at $\sim$0.1s after bounce follows the explosion ordering seen in the shock radii, with earlier explosions showing higher shock velocities at early times.

For the heaviest progenitors, the accretion rates remain over 1 $M_\odot$ s^{-1} until as late as 200 ms post-bounce, over a hundred of milliseconds longer than found by Radice et al. (2017) for a suite of lower mass (8.1 - 11 $M_\odot$) progenitors. We naively expect lower mass progenitors to have systematically lower accretion rates, resulting in less ram pressure to overcome to achieve explosion. While the five non-exploding models do have accretion rates which increase with mass, the four exploding models (16-, 17-, 19-, 21-$M_\odot$) see their accretion rates dip earlier for models that explode earlier. Note that even for our conservatively early definition of explosion time (shock radius reaching only 160 km, marked by the black diamonds), the accretion rate dips in advance of explosion, suggesting that the reduced accretion rate prompts explosion and is not a result of it. The magnitude of the accretion rate itself is not the determinant of explosion, but rather the interplay between accretion rate and accretion luminosity (Burrows & Goshy 1993; Müller & Janka 2015, Suwa et al. 2016). For instance, the 12-$M_\odot$ progenitor has the lowest accretion rate, but also a low luminosity (Fig. 3.4, top right panel) and does not explode. The sensitivity of explosion to the progenitor mass suggests that small differences in density profiles can be significant.

We propose that the early accretion of the Si/O interface promotes explosion (see also, e.g. Murphy & Burrows 2008). Looking at Fig. 3.1, we see that those models that do explode (solid) have several characteristics in their density profiles that distinguish them from models that do not explode (dashed). Namely, the density is quite high in the interior, out to 1.2 $M_\odot$, but then drops sharply. Furthermore, the exploding models all have a Si/O interface located interior to 1.7 $M_\odot$, where the density drops by a factor of several over a thin mass region. Our default 20- and 25-$M_\odot$ models also have Si/O burning interfaces, but these are located further out. The 12-, 13-, and 15-$M_\odot$ models do not feature prominent interfaces. None of these five models explodes during the physical time they were followed here, and all five models feature mean shock radii stagnating at 100 km, 700 milliseconds post-bounce. The variation in outcome − explosion or failure − over progenitors differing only by a solar mass suggests that certain density profiles are most prone to explosion, and that early accretion of the Si/O interface can be one key to explosion. In fact, looking at Fig. 3.1, we see that all four exploding models accrete Si/O interfaces early on, as indicated by the dip in accretion rates. Comparing with the shock radius evolution depicted in Fig. 3.2, we find explosion occurring soon after interface accretion.

In Fig. 3.3, we simultaneously show accretion rates at 500 km (in $M_\odot\ s^{-1}$, blue), the evolution of the Si/O interface (in km, red), and the maximum shock radius (in km, black) as a function of time after bounce (in seconds) for our four exploding models. Once the Si/O interface passes 500 km, at roughly 80 ms for the 21-$M_\odot$ progenitor, the corresponding accretion rate falls by a factor of five, from $\sim$10 to $\sim$2 $M_\odot\ s^{-1}$. Simultaneously, the maximum shock radii begins to climb towards explosion once it intersects the Si/O interface. The high accretion rates prior to interface accretion enhance the accretion luminosity interior to the stalled shock. The subsequent drop in accretion rate reduces the ram pressure of the infalling material exterior to the stalled shock, while still allowing the stalled shock to benefit for a short time interval

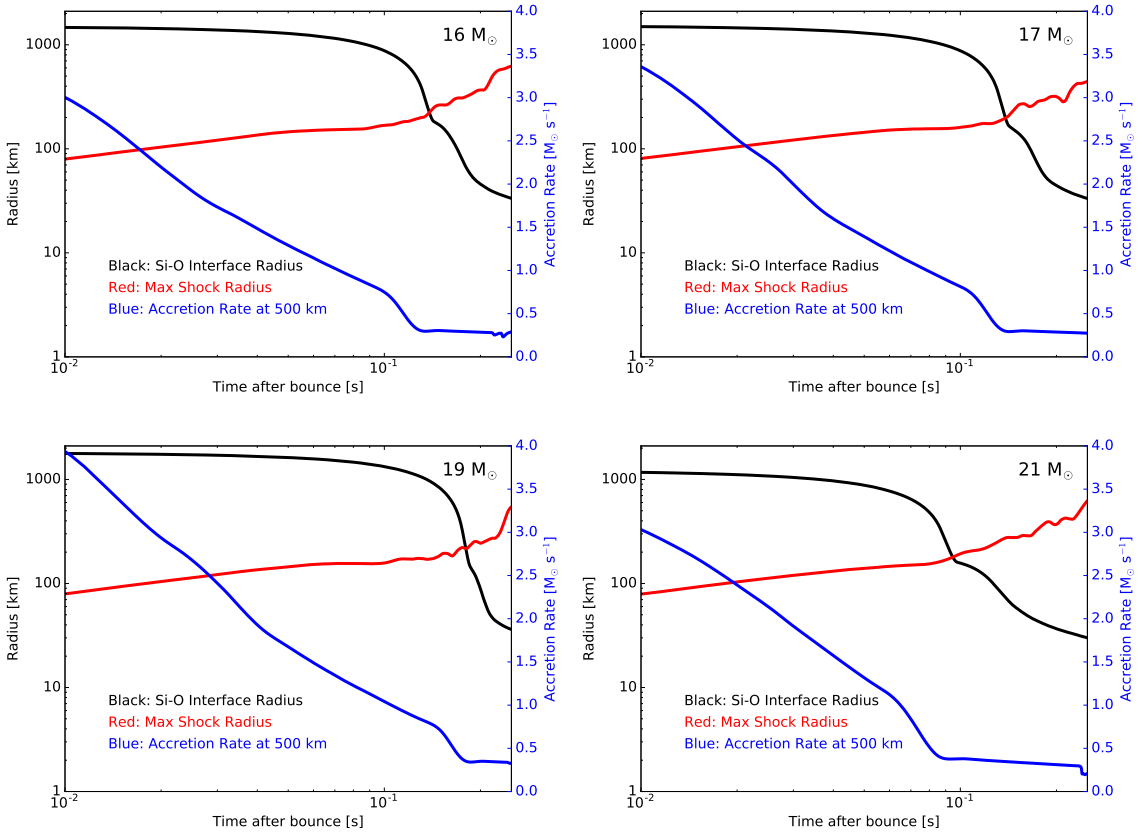

Figure 3.3: Maximum shock radius (in km, red), location of the Si/O interface (in km, black), and accretion rate at 500 km (in $M_\odot$ s^{-1}, blue) as a function of time after bounce (in seconds) for the exploding 16-, 17-, 19-, and 21-$M_\odot$ progenitors, left to right. The accretion rate radius is chosen to be close to, but outside, the maximum shock radius at early times post-bounce. We see a corresponding drop in the accretion rate just as the Si/O interface passes 500 km, which happens roughly 0.1 seconds after bounce for these models. Shortly afterwards, the maximum shock radius reaches the Si/O interface, and we witness the expansion of the maximum shock radius towards explosion. Note the simultaneous onset of variations in the maximum shock radius with the accretion of the Si/O interface.

from the high luminosity due to earlier accretion. This paints a coherent picture of the critical role of the interface in explosion.

The role of the Si/O interface has been studied earlier in literature. Using BETHE-hydro, Murphy & Burrows (2008) explored the evolution of the 11.2- and 15-$M_\odot$ progenitors, and found that accretion rates plummet following accretion of the Si/O interface. Hanke et al. (2013) evolve a 27-$M_\odot$ progenitor in both 2D and 3D and find strong shock expansion ensues after Si/O infall due to the resulting decrease in mass accretion. Summa et al. (2018) find that explosion for an artificially-rotating 15-$M_\odot$ progenitor follows shortly after accretion of the Si/O interface, but argue that a strong spiral SASI mode has set the grounds for explosion even earlier. Using Zeus-2D for 12-100 $M_\odot$ progenitors, Suwa et al. (2016) similarly found shock expansion associated with the density, and hence ram pressure, jump around the Si/O interface. However, shock expansion lasted briefly and the models did not explode. Recently, Ott et al. (2018) performed 3D simulations using the GR multi-group radiation hydrodynamics code ZELMANI. Omitting inelastic scattering processes and velocity dependence and with 12 energy groups spaced logarithmically between 1 and 248 MeV, they find similar results regarding the role of Si/O interface accretion to prompting explosion, perhaps even more critical than the compactness parameter. Similarly, for a suite of 2D progenitors from 11-28 $M_\odot$, Summa et al. (2017) find a steep drop in density at the Si/O interface corresponds to a reduction of the accretion ram pressure and subsequent strong shock expansion.

Literature is replete with analytical parametrizations of explosions, spanning the compactness (O'Connor & Ott 2011; O'Connor & Ott 2013; Nakamura et al. 2015) and Ertl parameters (Ertl et al. 2016), the antesonic condition (Pejcha & Thompson 2012; Raives et al. 2018); critical luminosity curves (Burrows & Goshy 1993; Summa et al. 2016; Summa et al. 2018) to scaling relations (Müller et al. 2016a) and integral

conditions (Murphy & Dolence 2017). We propose early accretion of the Si/O interface as one possible empirical condition.

3.4 Energetics and Diagnostics

Here, we present an analysis of the energetics of our results, explode the failed explosions of the prior section, and comment on the Y_e-mass ejecta distribution and the absence of the LESA.

In Fig. 3.4, we depict the lab-frame neutrino luminosities (in 10^{52} erg s^{-1}, top panel) and RMS energies (in MeV, bottom panel) as a function of time after bounce (in seconds), evaluated at 500 km and redshifted out to infinity for our nine progenitors. We assume a forward-peaked radial neutrino distribution as in Radice et al. (2017). At early times, RMS energies and luminosities are monotonic with progenitor mass for the non-exploding progenitors, with the 12-$M_\odot$ progenitor fielding neutrino luminosities 50% smaller and RMS energies 30% smaller than its more massive counterparts. Interestingly, the models that explode later reach higher post-breakout luminosities. Note that the exploding models show an expected dip in luminosities and RMS energies after explosion reverses accretion. Electron-type neutrino luminosities asymptote to $\sim 2 \times 10^{52}$ ergs s^{-1} by $\sim$1 second post-bounce for the exploding models.

We calculate diagnostic energies (Müller et al. 2012b) as the sum of the kinetic, internal, gravitational binding and nuclear binding energy interior to the grid and correct for the gravitational binding energies exterior to our 20,000 km grid. We list the binding and final energies in Table 3.1, with the latter summed over all zones where the final energy is positive.

The final explosion energies, with external binding energies subtracted, are illustrated in the top-left panel of Fig. 3.5 as a function of time after bounce for the four

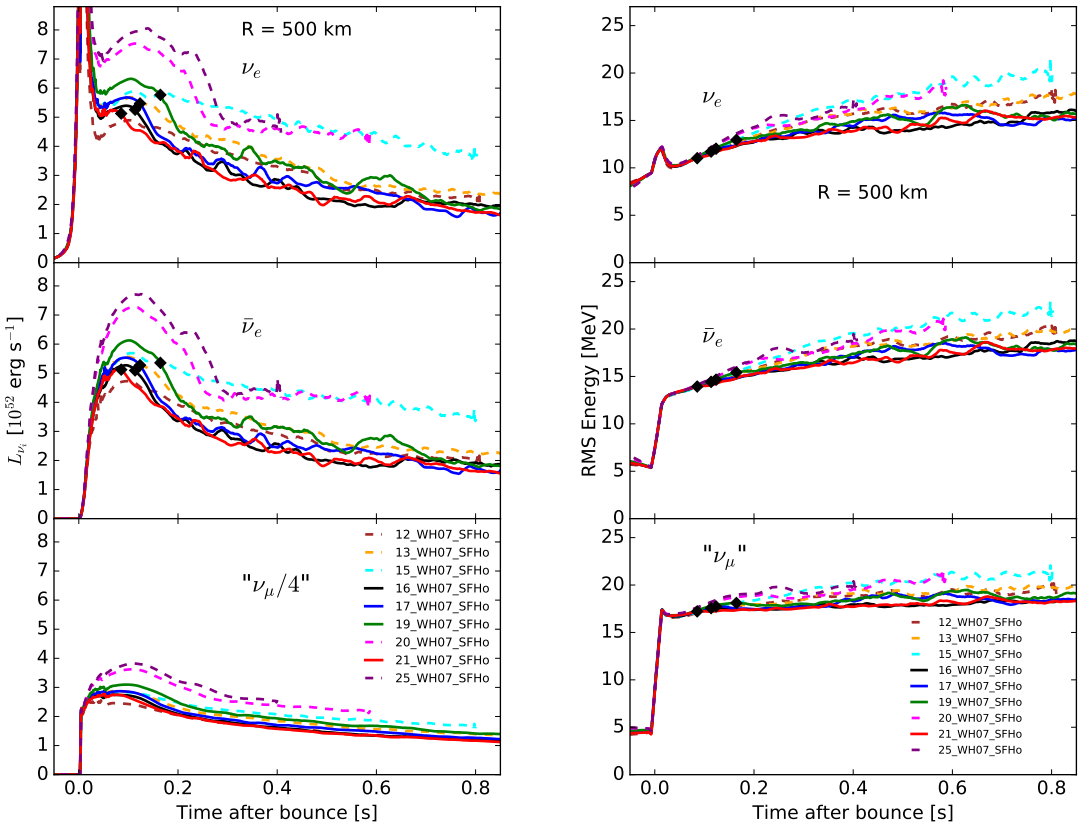

Figure 3.4: Lab-frame neutrino luminosities (ergs s^{-1}, **left panel**) and RMS neutrino energies (MeV, **right panel**) for our progenitor suite relative to time after bounce (in seconds) at 500 km. For the non-exploding models (dashed), the luminosities for all three neutrino species increases with progenitor mass. For the exploding models (solid), neutrino luminosity tracks explosion time, with earlier explosions having lower neutrino luminosities. Interestingly, we see no such feature in the RMS neutrino energies. Rather, all exploding models have similar RMS neutrino energies of under 15 MeV at late times for electron-type neutrinos. Non-exploding models have RMS energies several MeV higher for all neutrino species.

Model	M_{Bar} [$M_\odot$]	M_{Grav} [$M_\odot$]	-E_{Env} [10^{50} ergs]	E_{Tot} [10^{50} ergs]	$\dot{E}_{Tot}$ [10^{50} ergs s^{-1}]
16	1.70	1.52	1.57	1.64	0.4
17	1.74	1.56	2.02	2.89	0.8
19	1.84	1.64	2.70	2.40	0.8
21	1.63	1.47	3.56	-0.70	0.7

Table 3.1: Table 1: Explosion diagnostics and PNS properties for the four exploding models at the end of our simulations. We list the baryonic (M_{Bar}) and gravitational masses (M_{Grav}) in solar masses, the envelope energies (E_{Env}) and total explosion energies (E_{Tot}) in 10^{50} ergs, the rate of increase in explosion energy ($\dot{E}_{Tot}$) in 10^{50} erg s^{-1}. All values are calculated at the end of the simulation.

exploding progenitors. The 17-$M_\odot$ progenitor yields the highest diagnostic energy of $\sim 3 \times 10^{50}$ ergs at 2.0s after bounce. Its energy is still steeply rising at the end of the simulation, which ends once the outer shock radius reaches the grid edge at 20,000 km. This suggests the need to repeat such simulations over much larger radial domains and is consistent with the results found by Summa et al. (2016), who performed simulations over a 10,000 km grid and found explosion energies still rising for their suite of 12-, 15-, 20- and 25-$M_\odot$ WH07 progenitors.

Note, however, that they plot the diagnostic energy and do not correct for the gravitational binding burden off the grid, which would result in much smaller and even negative final energies for them. For the same progenitor suite, Bruenn et al. (2016) find final explosion energies corrected for the gravitational overburden − nearly an order larger, around 1 Bethe (1B = 10^{51} ergs). The 21-$M_\odot$ progenitor does not reach positive explosion energy by the end of our simulation since it has not yet overcome its gravitational overburden. Note also that the explosion energies anti-correlate with explosion times − the models that explode later have higher energies. The same behavior appears for the luminosities in Fig. 3.6, suggesting that a delayed explosion is more energetic. Interestingly, though the 16- and 17-$M_\odot$ progenitors explode almost simultaneously, their explosion energies are quite different, with the former asymptoting by the end of the simulation.

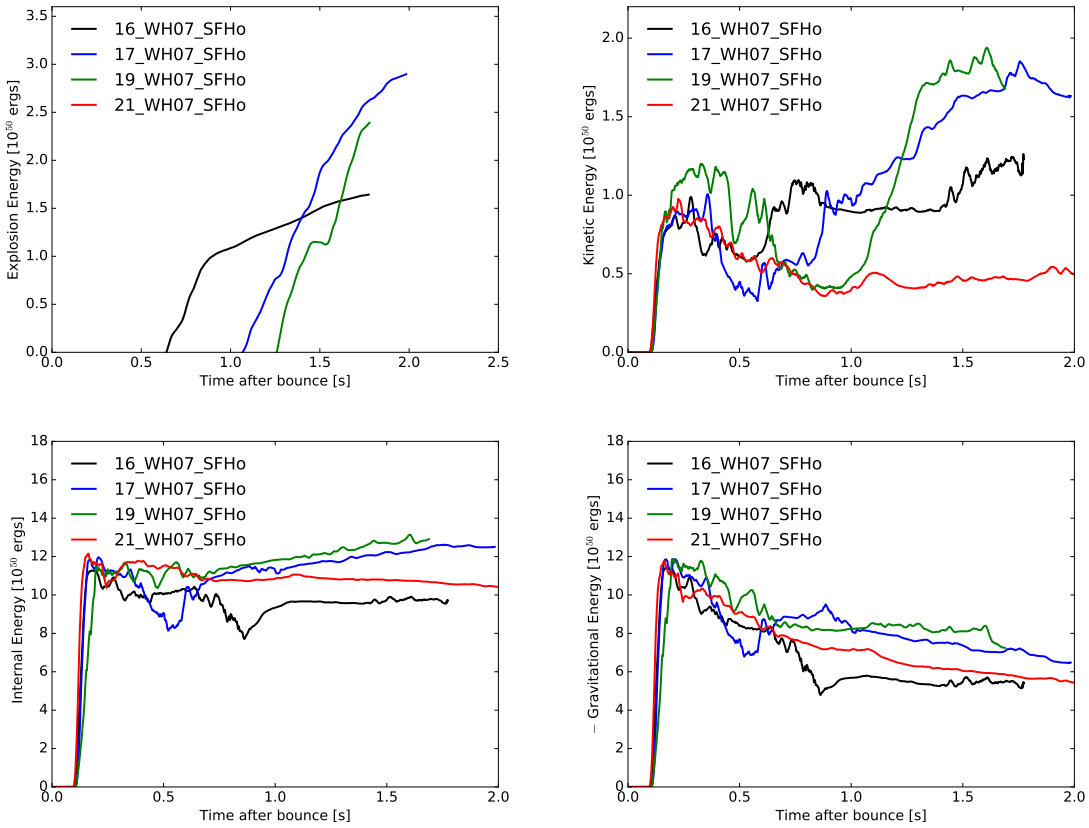

Figure 3.5: Explosion energies (in units of 10^{50} ergs) against time after bounce (in seconds) of the ejecta (defined as energetically unbound material) for the four exploding models. We plot the total explosion energy (**top left**), kinetic energies (**top right**), internal energies (**bottom left**), and gravitational binding energies (**bottom right**) multiplied by negative one to be positive. The explosion energy is defined in the text and includes the gravitational binding energy of the envelope exterior to our grid at 20,000 km. Note that, during the simulation, the 21-$M_\odot$ progenitor never has a positive explosion energy, despite being the first to explode. All energies are still rising at the end of the simulation, with the 16-$M_\odot$ progenitor having the slowest rate of increase. The 17-$M_\odot$ progenitor reaches the highest explosion energy, of 3×10^{50} ergs at the end of the simulation. Both the 17- and 19-$M_\odot$ models rise rapidly in kinetic energy after 0.8 seconds post-bounce, corresponding to a sharp increase in total energies. By comparison, both the internal energies and gravitational energies are relatively flat with time. Because we truncated our simulations when the shock radius neared the grid edge, with energies still rapidly rising, we highlight the significance of performing simulations over larger radial domains.

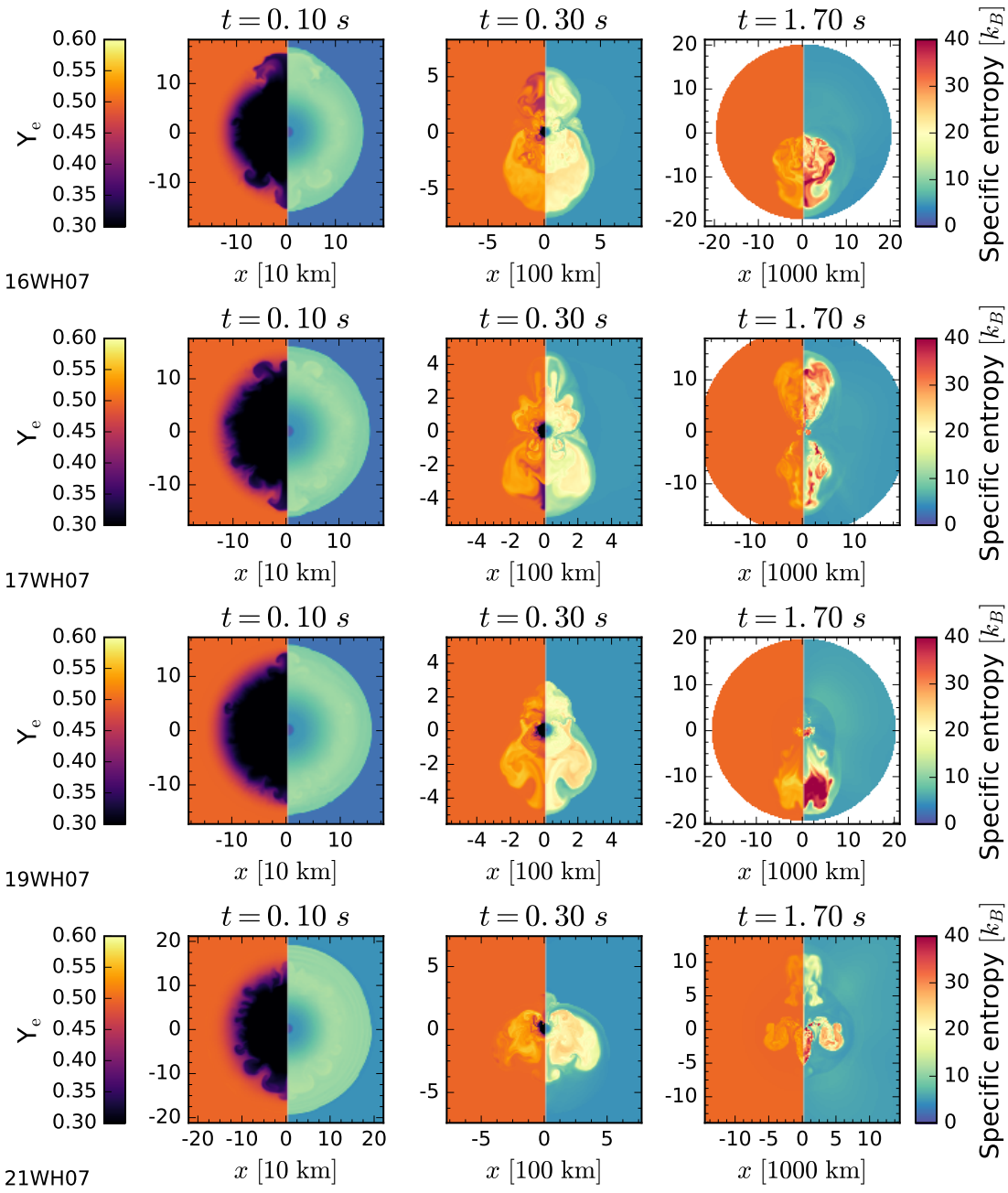

Figure 3.6: Ye (**left**) and specific entropy (k_B/nucleon, **right**) snapshots of the four exploding progenitors at 100, 300 and 1700 milliseconds post-bounce. As early as 100 ms post-bounce, we see nascent convection in the proto-neutron star. At late times, all explosions are very asymmetric. We find that models with multiple wide plumes have greater explosion energies than those localized in a single hemisphere. Because the two-dimensional nature of the simulation may artificially promote axial anisotropies, we presume that 3-D simulations will produce more isotropic explosions with consequently greater explosion energies.

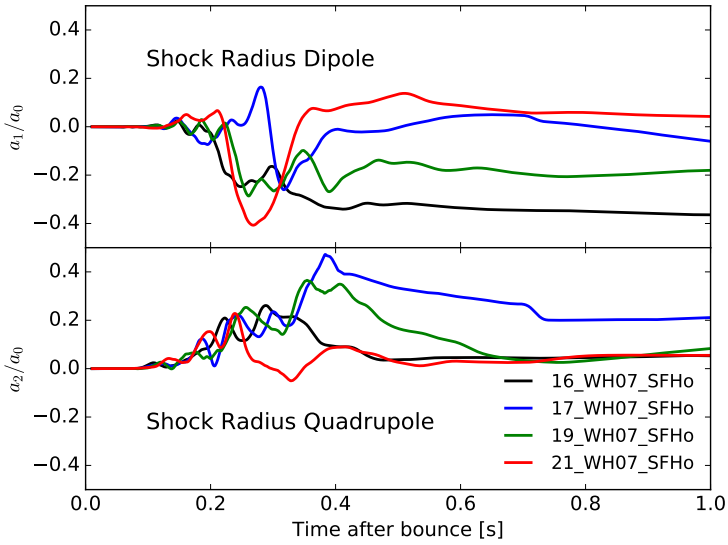

Figure 3.7: Dipole (**top panel**) and quadrupole (**bottom panel**) moments of the shock radii, normalized to the monopole moments and plotted against time after bounce (in seconds) for our four default exploding models. Note the presence of a strong dipole moment for the different models. Furthermore, all the models − with the possible exception of the 21-$M_\odot$ progenitor − have positive quadrupole moments, corresponding to equatorial pinching, with the 21-$M_\odot$ model showing equatorial wings as seen in the entropy profiles in Fig. 3.6.

In the top right panel, we show the kinetic energies which, early after bounce, are only a fraction of the internal energy. At late times, the kinetic energies of the 17- and 19-$M_\odot$ progenitors rise steeply, paralleling the larger explosion energy at late times for these models and accounting for roughly two-thirds of the final energies. Furthermore, from the entropy profiles in Fig. 3.6, we see that exploding models with multiple plumes covering a wider spread of solid angle have higher explosion energies. The 16-$M_\odot$ progenitor has an asymmetric explosion concentrated around the southern pole at late times, and has a correspondingly smaller explosion energy. On the other hand, the 17- and 19-$M_\odot$ progenitors have multiple wide plumes in both hemispheres with correspondingly higher explosion energies. The rapid rise in kinetic energy together with multiple expanding plumes, which drive this kinetic outflow, suggest that the morphology of the unbound material is significant in producing robust explosion

energies. Furthermore, simulations in 3D will not suffer from axial artifacts present in 2D; we thus expect more isotropic explosions in 3D with correspondingly higher explosion energies than in 2D. However, 3D simulations are required to draw consistent conclusions about explosion morphologies and energies. In the bottom right panel, we illustrate the (negative) gravitational binding energy interior to the grid, with magnitudes comparable to the internal energies. The 25-$M_\odot$ model does not have an exceptionally high interior binding energy; rather, a combination of low kinetic energy and high exterior binding overburden prevents its explosion energy from becoming positive. Its final energy at the end of our simulation is roughly -7×10^{49} ergs and rising.

As a final point on morphology, in Fig. 3.7, we plot the dipole (top panel) and quadrupole moments of the shock radii, normalized to the monopole moments and plotted against time after bounce (in seconds) for our four exploding models. All models feature a strong dipole moment, and with the possible exception of the 21-$M_\odot$ progenitor, have positive quadrupole moments, indicating equatorial pinching. Note that the 16-$M_\odot$ progenitor sustains a significant dipole moment even at late times and has a correspondingly smaller explosion energy. The 17-$M_\odot$ progenitor sustains a larger quadrupole moment at late times, and has a correspondingly larger explosion energy. These observations lend credence to our proposal that more isotropic explosions are more energetic, all else being equal.

3.4.1 Evolution of the Gain Region

To probe the dependence of progenitor mass on explosion outcome, we study the properties of the models in the gain region, defined as where there is net neutrino heating.

In Fig. 3.8, we illustrate, from top to bottom, the mass of the gain region in units of 10^{-3} $M_\odot$, the net heating rates $\dot{Q}$ in B s^{-1}, and the heating efficiency, defined as

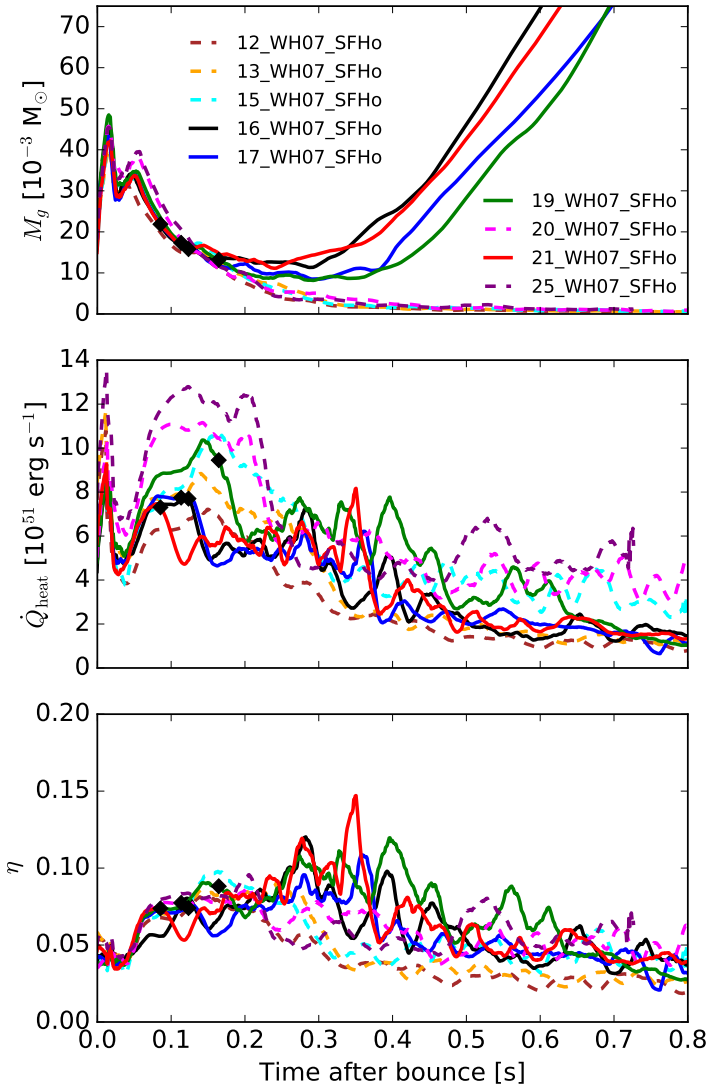

Figure 3.8: **Top panel**: Gain mass (in 10^{-3} $M_\odot$) as a function of time after bounce (in seconds). Through 100 ms post-bounce, the gain mass is similar for all the models. The gain mass then continues to rise for all the exploding models (solid lines), in order of explosion, and plummets for the non-exploding models (dashed). **Middle panel**: Heating rates (in 10^{51} erg s^{-1}) plotted against time after bounce (in seconds) for the nine models. The heating rates of the non-exploding models increase with increasing mass. Though the 20- and 25-$M_\odot$ progenitors have the highest heating rates, they are unable to overcome the greater gravitational binding energy. However, among the exploding models, earlier explosion corresponds to a lower heating rate. **Bottom panel**: Neutrino heating efficiency, $\frac{\dot{Q}_{heat}}{L_{\nu_e}+L_{\bar{\nu}_e}}$, of energy deposition. Note that the exploding models are distinguished by uniformly higher efficiency than the non-exploding models after explosion, as cooling fades.

$\frac{\dot{Q}_{heat}}{L_{\nu_e}+L_{\bar{\nu}_e}}$, as a function of post-bounce time (in seconds) for the suite of nine progenitor masses. In the top panel, models that explode (solid) continue to grow in gain mass past the first 200 ms, while the remainder (dashed) do not. Furthermore, models with higher accretion rates (see Fig. 3.1) have higher heating rates (middle panel) for the first 200 milliseconds of evolution, and hence earlier explosions feature lower heating rates. The heavier 20- and 25-$M_\odot$ models have the highest heating rates (not heating efficiency, bottom panel) early on, but these prove insufficient to overcome the greater ram pressure and the explosions are stifled. The exploding models have significantly higher heating efficiencies (bottom) after 200 milliseconds, following the explosion, than the non-exploding progenitors, with efficiency peaking at 0.15 for the 21-$M_\odot$ progenitor around 350 ms post-bounce.

For comparison, Summa et al. (2016) study 12-, 15-, 20-, and 25-$M_\odot$ progenitors, finding maximum heating efficiencies in the gain region of $\sim$0.12, 600 milliseconds post-bounce, and Bruenn et al. (2016) find maximum efficiencies of $\sim$0.15, 200 milliseconds post-bounce. Changes in gain properties may be endemic of explosion and not necessarily its precursors.

3.4.2 Microphysical Dependence

We briefly explore the effects of inclusion of various physical processes to the explosion outcome. We use the 16-$M_\odot$ progenitor as a case study. In Fig. 3.9 (top left panel), we plot the mean shock radii (top panel) for three runs − the default ('def') with IES_INS_MB, one with IES_INS, and one with IES only.

We note a steady march towards explosion as we include additional physical processes. Adding inelastic scattering off nucleons leads to a shock radius stalling further out, and the inclusion of the many-body effect converts the failure to explosion. Without all three effects, our 16-$M_\odot$ progenitor does not explode.

Buras et al. (2006) performed an early comparison of different neutrino interaction rates, finding reduced ν_e, $\bar{\nu}_e$ opacities when including inelastic scattering of neutrinos off nucleons via Burrows & Sawyer (1998), rather than the elastic approach of Bruenn (1985). Müller et al. (2012b) finds higher ν_e, $\bar{\nu}_e$ luminosities when including inelastic scattering off nucleons. Furthermore, O'Connor et al. (2017) find increased neutrino heating due to the many-body effect (Horowitz et al. 2017). Finally, O'Connor & Couch (2018b) found that including inelastic scattering produced earlier explosions for the 12-, 15-, and 25-$M_\odot$ progenitors, though not early enough to overcome the discrepancy in explosion time between their work and that of Summa et al. (2016).

As illustrated in Burrows et al. (2018), however, one can prompt the model without the many-body effect to explode by including either perturbations to the infall velocities or modifying the opacity table to include the Fischer (2016) correction to the nucleon-nucleon bremsstrahlung ("bf") and cutting the electron capture rate Juodagalvis et al. (2010) on heavy nuclei to only 20%. Non-exploding models can be made to explode with moderate changes to physical inputs.

3.4.3 Exploding the "Non-Exploding" Models

Though the many-body effect was crucial in exploding the 16-$M_\odot$ progenitor, this default microphysical setup proved insufficient in exploding five of our other WH07 models. Five (the 12-, 13-, 15-, 20-, and 25-$M_\odot$ models) of our nine WH07 models did not explode with the default setup, and we identify the absence of a sharp Si/O interface in the progenitor interior (see Fig. 3.1) as one key difference. We find that with the inclusion of additional inputs, such as perturbations and/or moderate rotation, all these models explode.

We perturb the infalling velocities to 1000 km s^{-1} over 3 regions using the prescription of Müller & Janka (2015) (see also Radice et al. 2017). We use $n = 5$ radial nodes and $l = 2$ angular modes. Our perturbed regions span 1000-2000 km, 2100-

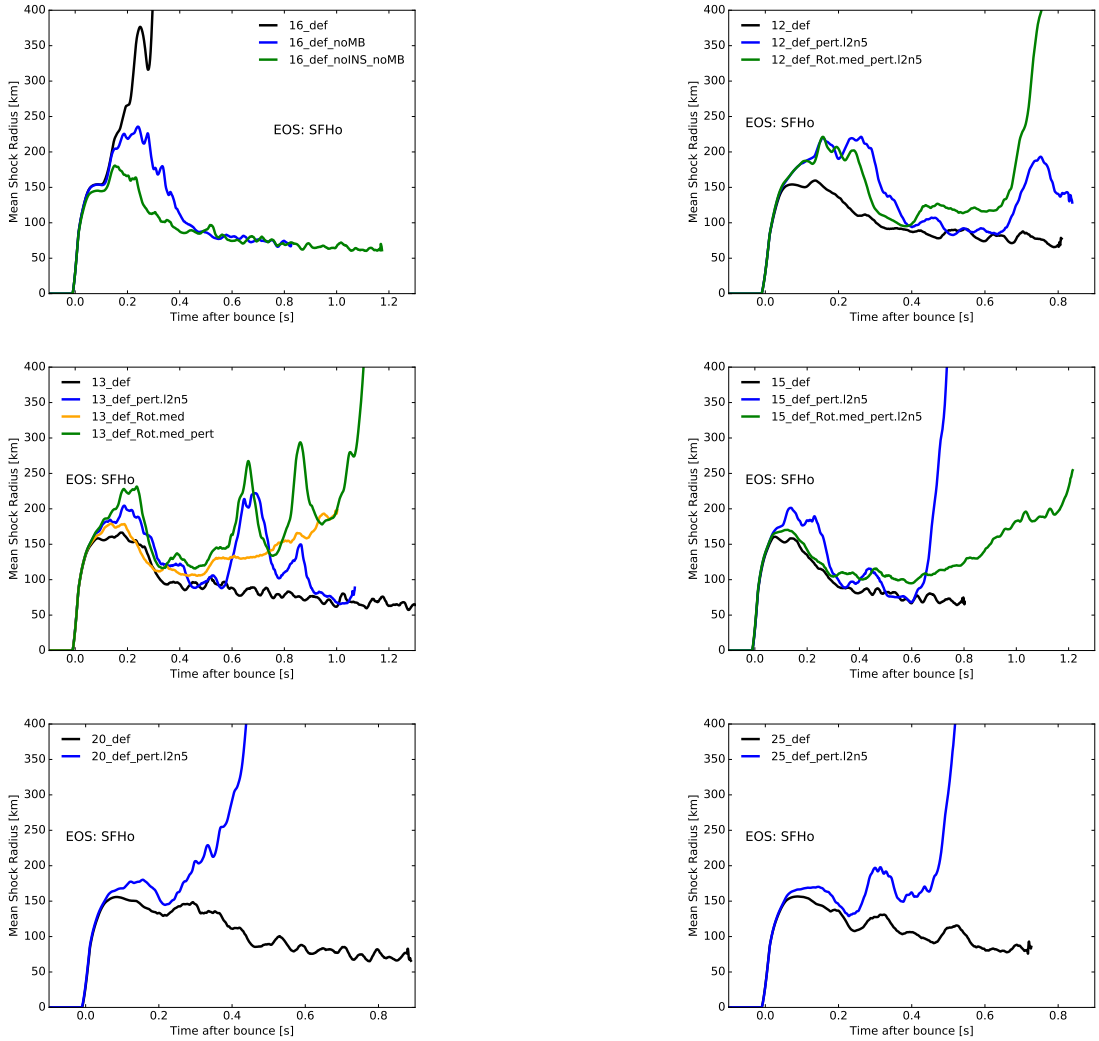

Figure 3.9: Mean shock radius (in km) versus time after bounce (in seconds) illustrating the role of both microphysical (**top left**, 16-$M_\odot$) as well as macrophysical inputs (**remaining five panels**) in prompting explosion. For the latter, we show that the non-exploding models of Fig. 3.1 (12-, 13-, 15-, 20-, and 25-$M_\odot$) explode with perturbations to the infall velocities (indicated 'pert.l2n5', blue) and moderate rotation (indicated with 'Rot_med', green). In the top left panel, we illustrate the role of inelastic scattering off nucleons (INS), as well as the neutral current many-body effect (MB), in driving the stalled shock radius further out and to explosion, respectively. However, these additions prove insufficient to explode the remaining five models shown. We follow Müller & Janka (2015) in implementing spherical harmonic perturbations to velocities on infall over three regions, extending to 6000 km. All regions have $l = 2, n = 5$ and maximum velocity of 1000 km s^{-1}. We further implement modest cylindrical rotation (Rot_med) where indicated (see 13-$M_\odot$ for a model with rotation alone, orange), with $\Omega_0 = 0.2$ radians s^{-1} along the pole and a characteristic half-radius of 10,000 km. Note that, while rotation is essential for explosion (e.g., for the 12- and 13-$M_\odot$ progenitor), it delays explosion for the 15-$M_\odot$ progenitor.

4000 km, and 4100-6000 km. The inner region was chosen to be just outside our core at the start of the simulation and the outer region was approximated by the radial extent of matter that would be accreted during the first half-second after bounce, by which time the default models have exploded. We find that the outcome is crucially sensitive to when these perturbed regions are accreted.

For our rotation prescription, we assume a cylindrical rotational profile following Eriguchi & Müller (1985). Our rotational angular frequency along the pole is a moderate 0.2 radians s^{-1}, corresponding to a period of just over 30 seconds. The characteristic radius, over which the frequency drops to half this value, is 10,000 km, much larger than normally assumed. We find that moderately rotation near the center that remains high at large radii is most promising for explosion (see Vartanyan et al. 2018b, in prep.).

We plot our results in Fig. 3.9. The 15-, 20- and 25-$M_\odot$ progenitors explode with only the addition of perturbations to infall velocities. However, the 12- and 13-$M_\odot$ models require the further inclusion of moderate rotation to explode. Note, however, that the 13-$M_\odot$ progenitor explodes with rotation alone (orange curve in third panel of Fig. 3.9. For comparison, we also add rotation to the 15-$M_\odot$ progenitor and find, quaintly enough, that rotation delays explosion here by roughly 400 ms. The non-monotonic affect of rotation on explosion outcome will be further explored in Vartanyan et al. (2018b).

3.4.4 Electron Fraction Distribution

We study the ejecta mass distribution (with the ejecta defined as the gravitationally unbound mass) with Y_e at the end of our default simulations. Figure 3.10 illustrates a histogram of these results with Y_e bin resolution of 0.003. Independent of progenitor mass, all models show a peak near $Y_e = 0.5$, with a tail extending to $Y_e = 0.6$. Only the lowest mass progenitor, 16 $M_\odot$, shows a tail extending to lower Y_e values.

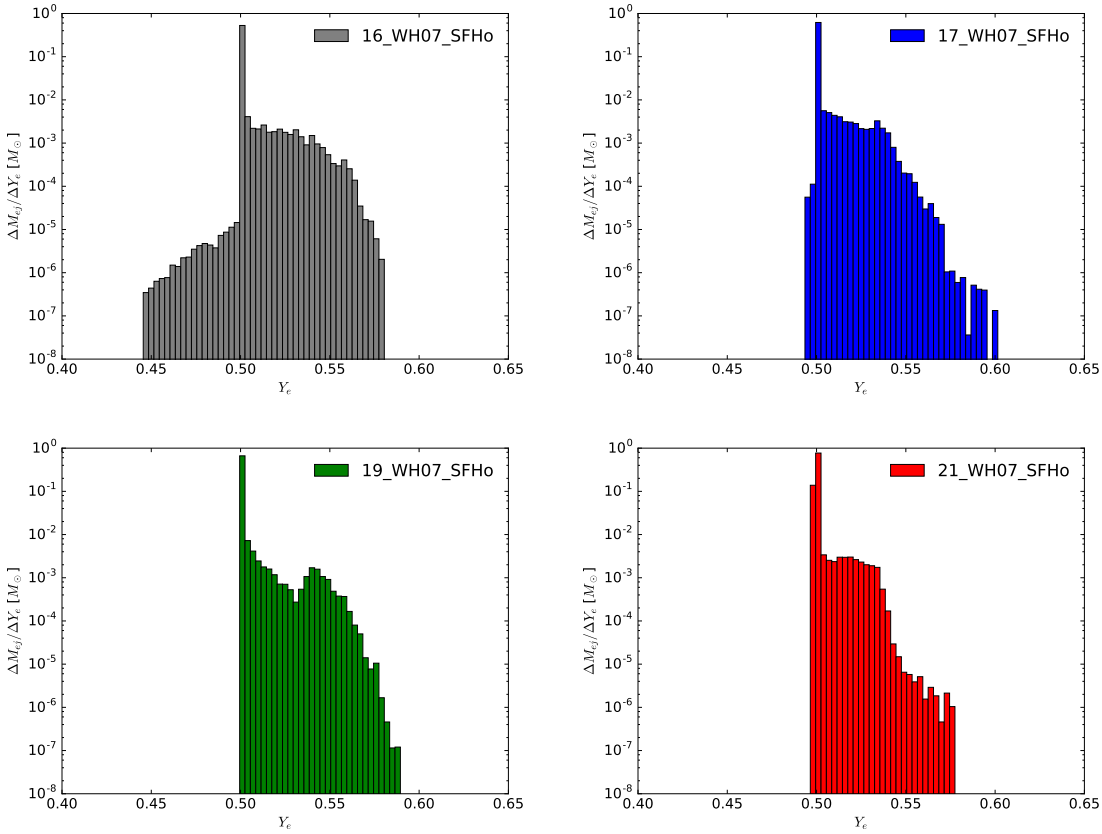

Figure 3.10: Histograms illustrating the ejecta mass distribution function of Y_e for our four default exploding models at the end of the evolution evaluated when the shock reaches the outer edge of the grid. The bins have width 0.003 Y_e. Surprisingly, all the models except the 16-$M_\odot$ show a similar distribution of Y_e, with a peak near 0.5 and distribution skewed towards larger values of Ye.

Recently, Wanajo et al. (2018) found that, for their sample of four low-mass progenitor supernovae, lower-mass progenitors had more neutron-rich ejecta due to faster shock growth and, hence, less dwell time of the neutron-rich ejecta for neutrino processing. This holds true for the lower-mass progenitors, which are relatively isotropic in explosion. However, we find little correlation between the shock velocities of our more massive models (see Fig. 3.2) and the ejecta distribution, Fig. 3.10, where perhaps multidimensionality and ejecta anisotropies play a bigger role. For instance, our 16-$M_\odot$ progenitor is the only model with outflow concentrated in the southern hemisphere (see Fig. 3.6), which we suggested earlier could lead to a correspondingly

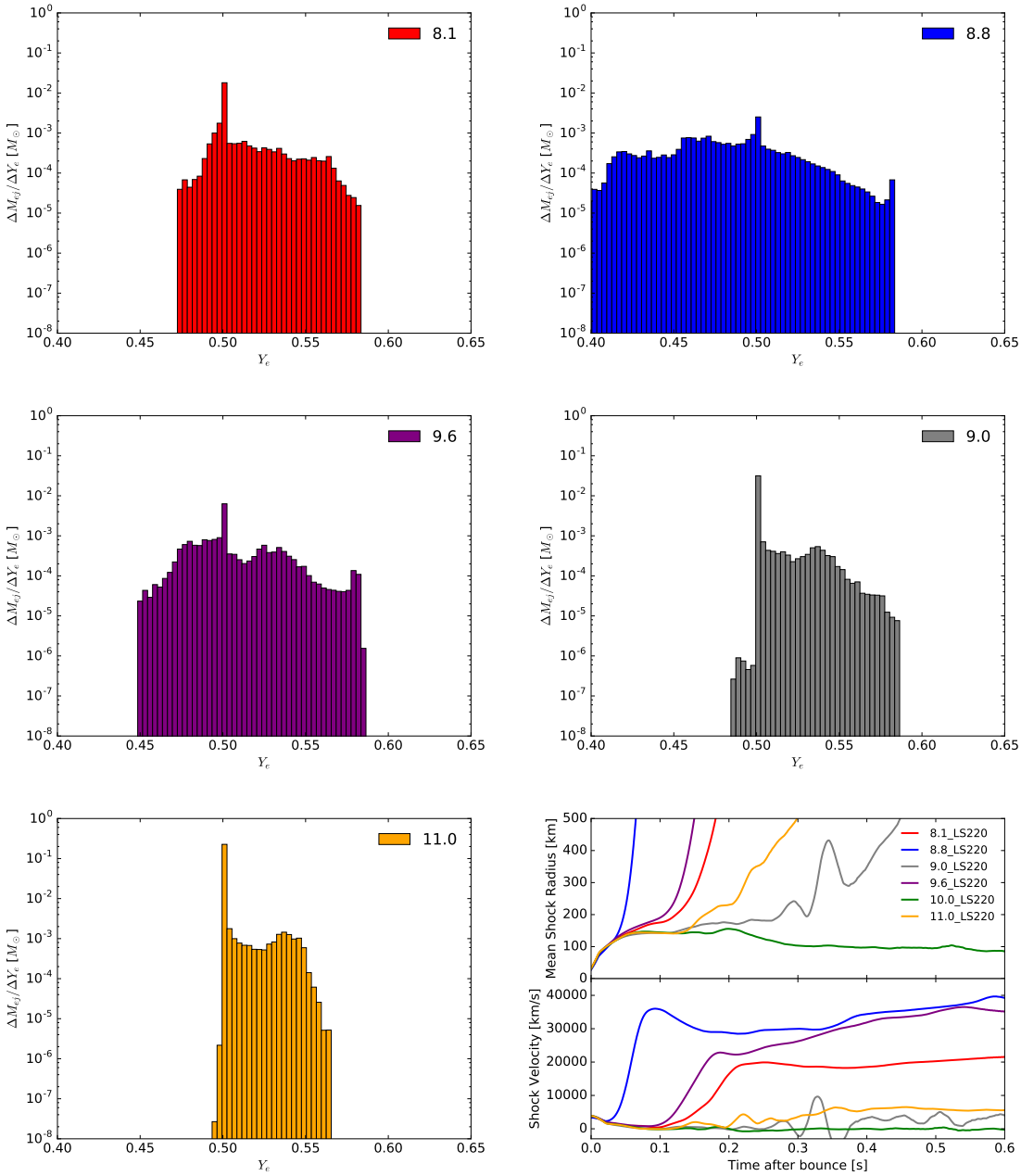

Figure 3.11: Histogram (**first five panels**) illustrating the ejecta mass distribution function of Y_e for the five exploding models models from Radice et al. (2017) evaluated when the shock reaches the outer edge of the grid. The lower-mass progenitors with ejecta mass distributions extending to lower Y_e, namely the 8.1-, 8.8-, and zero-metallicity 9.6-$M_\odot$ progenitors, all have significantly higher mean shock velocities as seen in the **bottom right panel**, illustrating the mean shock radii (in km) and mean shock velocity (in km s^{-1}) as a function of time after bounce (in seconds). These are also the models that explode earlier. Note that the 10-$M_\odot$ progenitor does not explode, even with the many body correction. All models were evolved with the LS220 equation of state.

smaller explosion energy. Such an anisotropic explosion would also leave neutron-rich material in the northern hemisphere relatively untouched, possibly explaining the low-Y_e tail for the 16-$M_\odot$ model seen in Fig. 3.10.

To explore this claim, we add in Fig. 3.11 the Y_e distribution of the ejecta mass for a set of low-mass progenitors from Radice et al. 2017, which we note uses the LS220 and not the SFHo EoS, as per our calculations (all else equal). We look at an 8.8-$M_\odot$ model (Nomoto 1984; Nomoto 1987); an 8.1-$M_\odot$ model (Müller et al. 2012a); an initially metal-free 9.6-$M_\odot$ model (Müller et al. 2013); and 9-, 10-, 11-$M_\odot$ models (Sukhbold et al. 2016), using the Lattimer-Swesty (LS220) equation of state with nuclear incompressibility of 220 MeV (Lattimer & Swesty 1991). Radice et al. (2017) find that all models except for the 10-$M_\odot$ progenitor explode with the inclusion of inelastic scattering off electrons and nucleons as well as the Horowitz et al. (2017) many-body correction (the 10-$M_\odot$ model explodes with the further addition of perturbations to infall velocities). We plot in the final panel of Fig. 3.11 the mean shock radii (km) and shock velocities (km s^{-1}) as a function of time post bounce (in seconds) for these six low-mass progenitors. Note that the shock velocities show a bimodal clumping: 1) those weakly explosive models (9- and 11-$M_\odot$) with shock velocities less than 10,000 km s^{-1} (together with the non-exploding 10-$M_\odot$ progenitor), and 2) the three more robust explosions with shock velocities spanning 20,000 to 40,000 km s^{-1} (the 8.1-, 8.8-, and 9.6- $M_\odot$ progenitors). In our Y_e histograms in Fig. 3.10, we see that these three lower mass ECSN progenitors have more low-Y_e ejecta together with greater shock velocities, in agreement with Wanajo et al. (2018). For comparison, all four of our more massive exploding models have smaller shock velocities, asymptoting at roughly 7000 km s^{-1} (see Fig. 3.2), and the association between shock velocity and ejecta mass is less clear for these more massive progenitors, where we argue explosion anisotropies play a more decisive role in Y_e-ejecta mass distribution.

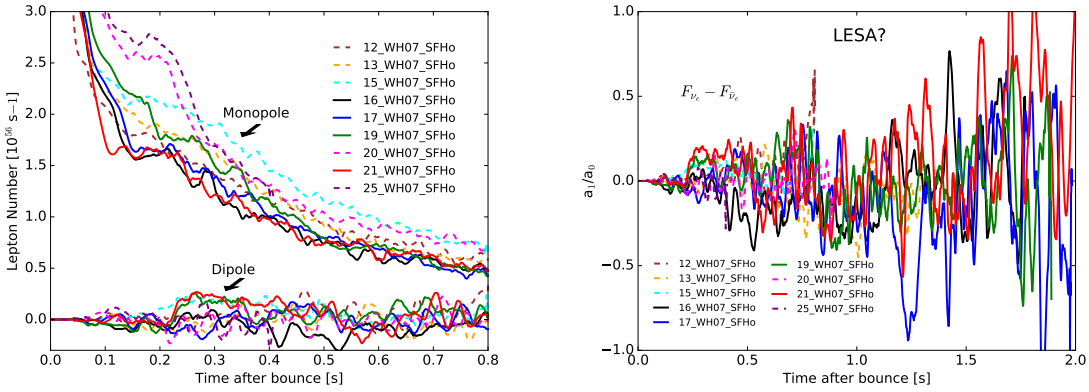

Figure 3.12: Following Tamborra et al. (2014a), we plot the ratio of the dipole and monopole (**top panel**) of the differences in lepton number fluxes at 500 km and their ratios (**bottom panel**) as a function of time after bounce (in seconds). Note the different x-axis scales. We find our dipole term to be an order of magnitude smaller, at least for the first several hundred milliseconds than Tamborra et al. (2014a) (who perform the simulations in 3D with the ray-by-ray plus approximation but find no explosions). This is in agreement with Dolence et al. (2015), though we find our dipole component to be slightly larger. Furthermore, even when the dipole term is of the same order as the monopole term (around one second post-bounce, when the latter has decayed sufficiently), the amplitudes are oscillating and not sustained. Only for the 21-$M_\odot$ model (red) do we find a sustained dipole term from 200 to 500 ms post-bounce, but even this is smaller by an order of magnitude than the results found by Tamborra et al. (2014a) for their progenitor suite. See text for more details.

3.4.5 LESA

Following Tamborra et al. (2014a), we look for evidence for the Lepton-number Emission Self-sustained Asymmetry (LESA), a neutrino-hydrodynamical instability that may set in shortly before explosion. In Fig. 3.12, we plot (top panel) the dipole and monopole moments of the neutrino number asymmetry (defined as the number flux of electron-type neutrinos minus anti-electron type neutrinos, $F_{\nu_e} - F_{\bar{\nu}_e}$,) and the ratio of the two (bottom panel). Relative to Tamborra et al. (2014a) (who perform the simulations in 3D with the ray-by-ray plus approximation but find no explosions), we find our dipole term to be an order of magnitude smaller, at least for the first several hundred milliseconds. This is in agreement with Dolence et al. (2015), though we find our dipole component to be slightly larger. Furthermore, even when the dipole

term is of the same order as the monopole term (around one second post-bounce, when the latter has decayed sufficiently), the amplitudes are oscillating and not sustained. Only for the 21-$M_\odot$ model (red) do we find a sustained dipole term from 200 to 500 ms post-bounce, but even this is smaller by an order of magnitude than the results found by Tamborra et al. (2014a) for their progenitor suite. Thus, we conclude that we do not find evidence for lepton-emission self-sustained asymmetry (LESA), at least in 2D. However, we emphasize that thorough analysis requires performing the simulation in 3D with correct neutrino transport.

3.5 Neutron Star Properties

Here, we provide a few of the properties of the remnant proto-neutron star in our model suite. We identify the proto-neutron star (PNS) radius where the density first drops below 10^{11} g cm^{-3}, though the radius is quite insensitive to the precise density cutoff near this value.

In Fig. 3.13 and Fig. 3.14, we study both the dependence upon progenitor mass and the detailed microphysics on PNS mass (top panel) and radius (bottom panel) for two sets of models: all nine progenitors in 2D, and the four exploding progenitors in 2D and their 1D counterparts. For the former, we also plot the gravitational mass following the approximate fit of Timmes et al. (1996). Since the density drops sharply at the PNS surface, the PNS radii are insensitive to the ambient pressure external to the core and, hence, to the progenitor mass (see also Radice et al. 2017), and we find that all PNS radii converge to the same mass by 1.5 seconds post-bounce for all the progenitors in 2D. However, we find that the PNS radii are sensitive to the dimensionality, with the 1D models' PNS radii roughly 20% smaller than the 2D counterparts. Radice et al. (2017) find a similar result for their set of low-mass progenitors, attributing the larger radii in 2D to convection in the PNS.

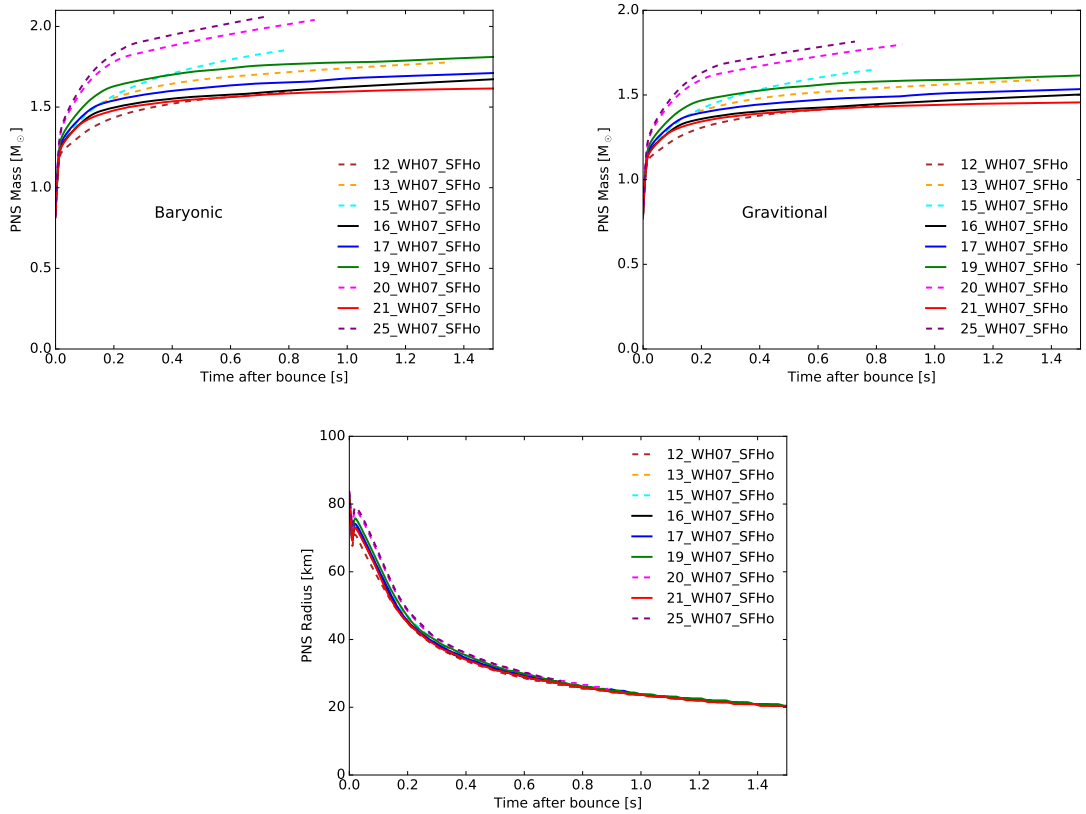

Figure 3.13: PNS baryonic (**top left**) and gravitational masses (**top right**) in $M_\odot$, and PNS radii (**bottom**) in km for our nine progenitors plotted against time after bounce (in seconds), with the PNS surface at a density of 10^{11} g cm^{-3}. The two most massive non-exploding progenitors, 20- and 25-$M_\odot$, reach almost 2 $M_\odot$ in baryonic PNS mass only half a second after bounce, whereas the others are clustered between 1.6 and 1.8 $M_\odot$. The PNS masses for the non-exploding models (dashed) increase monotonically with progenitor mass, whereas they increase in order of explosion time (and thus accretion history) for the four exploding models (solid). The PNS radii evolve to be independent of progenitor mass within one second of bounce.

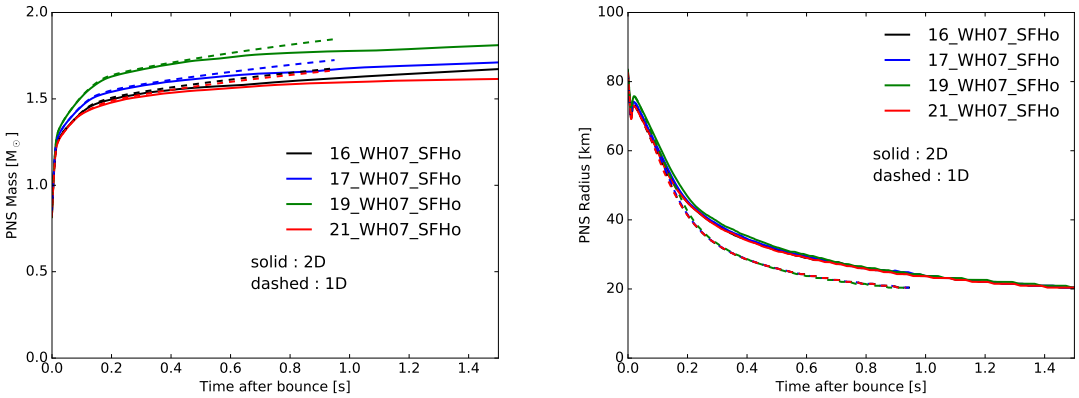

Figure 3.14: PNS masses (**left**) in $M_\odot$ and radii (**right**) in km, defined as where the density is above 10^{11} g cm^{-3}, for our four default exploding progenitors in 2D (solid) and corresponding 1D (dashed) as a function of time (in seconds) after bounce. The PNS masses are roughly correlated with progenitor masses and indicate their respective accretion history, hence the higher PNS mass for the non-exploding 1D models. Note that the PNS radii all converge to a similar mass regardless of progenitor mass, as determined by the equation of state. The larger PNS radii in 2D is attributed to inner PNS convection.

The PNS baryon mass evolution on the other hand, simply tracks accretion history. For the non-exploding (dashed) models in Fig. 3.13, this is monotonic with progenitor mass, spanning from ∼1.6 to ∼2.0 $M_\odot$ for the 12 to 25-M⊙ progenitors, respectively, and correlates roughly monotonically with progenitor mass. For the 20- and 25-$M_\odot$ progenitors, the PNS exceeds 2.0 $M_\odot$ as early as 0.6 seconds post-bounce. Unlike the four exploding models, the non-exploding models have not yet asymptoted by the end of the calculation. Figure 3.14 illustrates the mass evolution comparing 1D and 2D. The latter explodes, reverting accretion, and hence, leaves behind a smaller PNS mass.

3.5.1 Effect of Microphysics on PNS Masses

Due to the reduced neutrino opacities, we find that the many-body effect leads to a faster PNS contraction rate and a smaller PNS radii by ∼5%, as was found to be the case for low-mass progenitors by Radice et al. (2017). Furthermore, because the

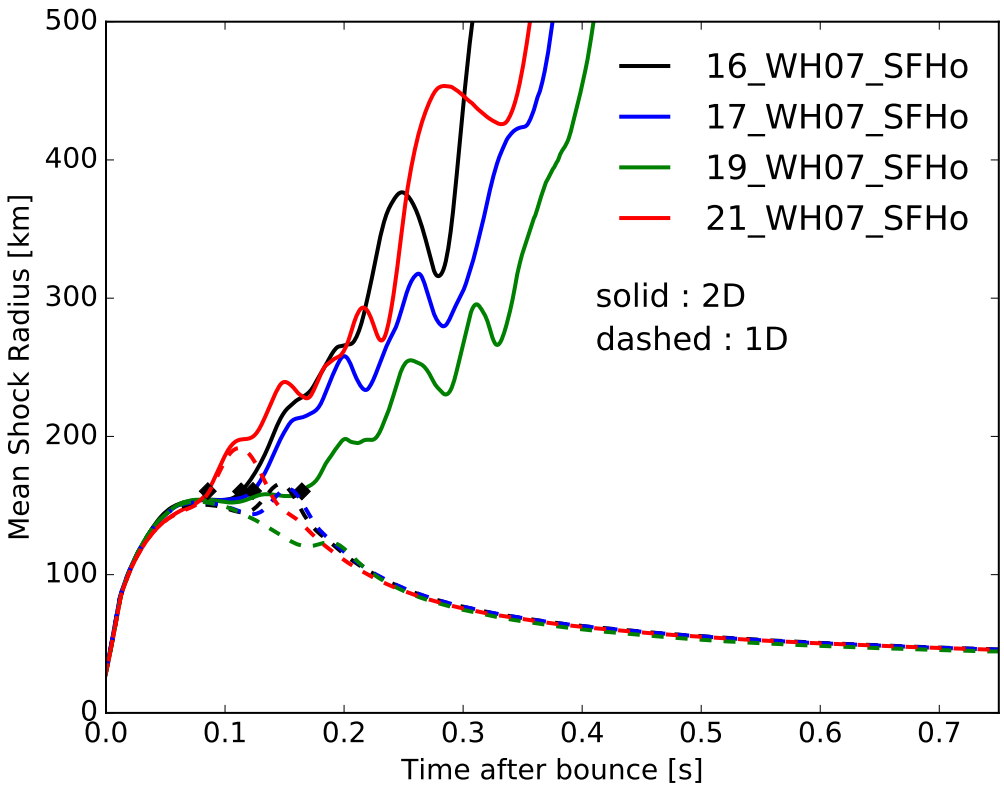

Figure 3.15: Mean shock radii (in km) against time after bounce (in seconds) of the exploding models in 2D (solid) and their non-exploding 1D counterparts (dashed). The 1D counterpart evolve similarly until roughly 100 ms post-bounce, even featuring analogous bumps in shock radii with the same time ordering as the 2D models. None of the 1D models explodes but all asymptote to roughly 40 km at late times.

model with the many-body correction prompts an earlier explosion, it leads to smaller PNS masses because of the shorter accretion history.

3.6 1D Comparison

Here, we compare one-dimensional counterparts to the four models that explode in two dimensions. The shock radii (in km) for these eight models are shown in Fig. 3.15 as a function of time after bounce (in seconds). None of these models explodes by the end of our simulations, spanning at least 700 milliseconds post-bounce.

Figure 3.16 depicts the luminosities (in 10^{52} erg s^{-1}) and RMS energies (MeV) as a function of time after bounce (in seconds) for the 2D models and their 1D counterparts. The electron and anti-electron luminosities dip after explosion for the former as accretion is reversed. However, the 2D models have consistently higher "ν_μ" luminosities by $\sim$50%, which is in agreement with Radice et al. (2017) and O'Connor & Couch (2018b), who cite increases in heavy-neutrino luminosities due to PNS convection in multi-dimensional simulations (see also Burrows & Fryxell 1993; Keil et al. 1996; Dessart et al. 2006). In Fig. 3.6, we see an inner convective region for the 2D models driven by a negative Y_e gradient developing in the PNS as early as 100 ms post-bounce. Indeed, since our 1D models do not explode and accretion continues for longer, we may be underestimating the effects of convection in our comparison.

In Fig. 3.17, we compare gain region properties for the four exploding models (solid) in 2D to their counterparts in 1D (dashed). Up to 100 ms post-bounce, the gain region mass, heating rate, and heating efficiency are quite similar for the two cases. The similarities are short-lived at later times, the gain mass, heating rates, and heating efficiency of the 1D models plummeting to values much smaller than their 2D counterparts. Hence, dimensionality of the simulation is directly reflected in the energetics of the exploding models.

3.7 Conclusions

We have presented a series of 2D radiation-hydrodynamic simulations for nine progenitors with inelastic scattering processes off electrons and nucleons, as well as the many-body correction to neutrino-nucleon scattering opacities over a grid extending out to 20,000 km. We find that four of these models (16-, 17-, 19-, and 21-$M_\odot$ from Woosley & Heger 2007) explode in this default configuration. These four models have Si/O interfaces featuring a significant density drop which reduces the accretion rate

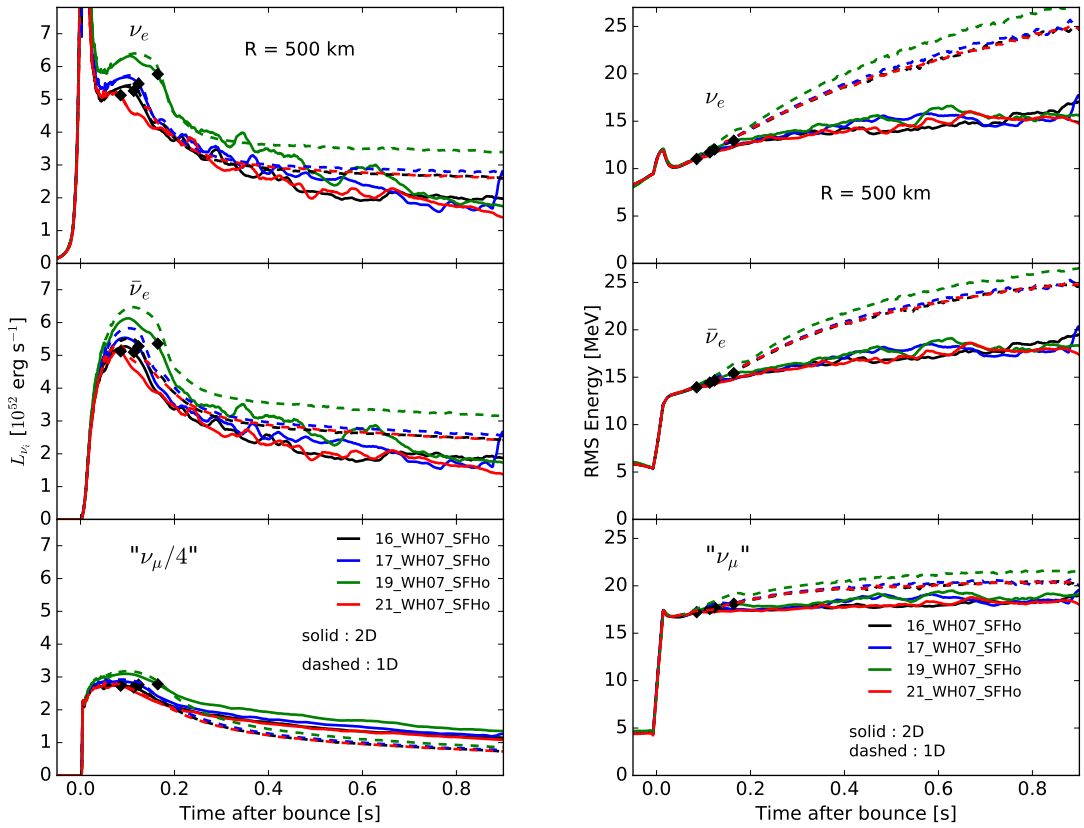

Figure 3.16: Same as Fig. 3.4, but now comparing the exploding models in 2D (solid) to their non-exploding 1D counterparts (dashed). The 2D models have lower electron- and anti-electron type neutrino luminosities, but higher heavy-type neutrino luminosities associated with PNS convection. Furthermore, peak neutrino luminosities are monotonically increasing with progenitor mass. All 1D RMS energies are consistently higher than their 2D counterparts.

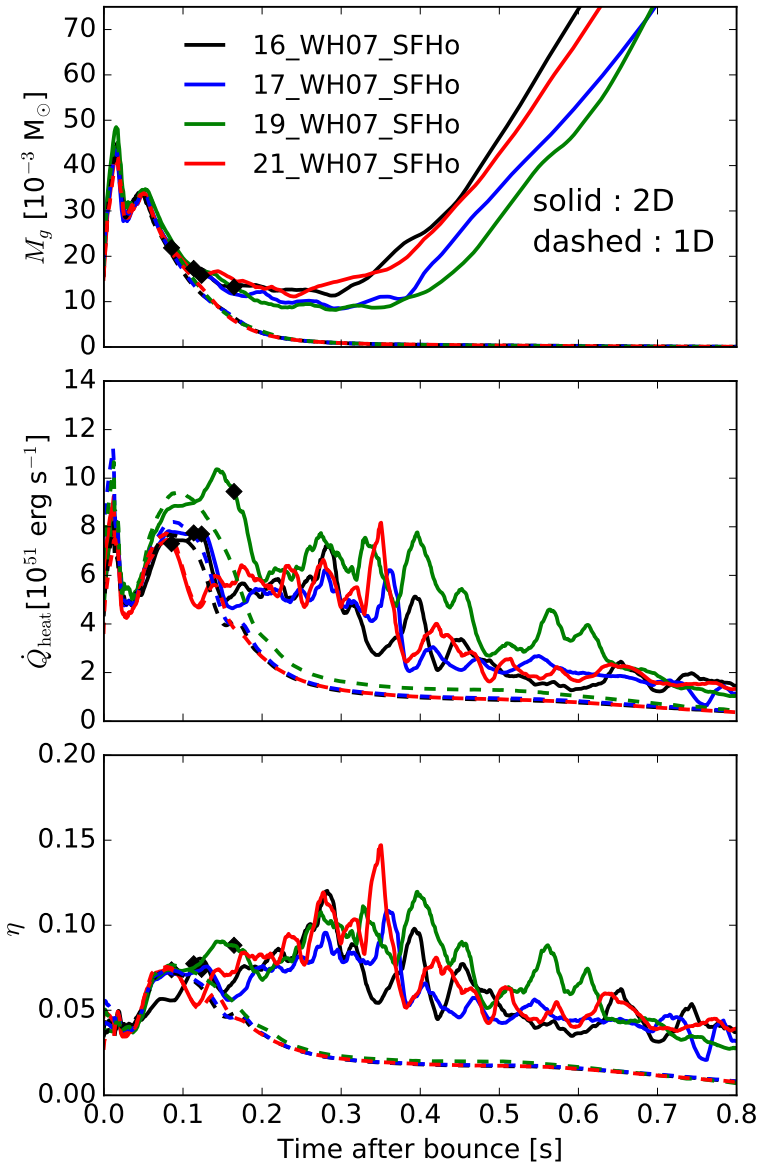

Figure 3.17: Same as Fig. 3.8, except comparing exploding models (solid) in 2D to their counterparts in 1D (dashed), none of which explodes. Up to 100 ms post-bounce, these diagnostics of the gain region − mass, heating rate, and heating efficiency − are quite similar for the two cases. After explosion, the gain mass, heating rates, and heating efficiency of the 2D models rise to values much higher than their 1D counterparts. Dimensionality of the simulation is directly reflected in the energetics of the exploding models.

near the stalled shock and prompts early explosion. All four models explode within 200 milliseconds of bounce. The remaining five models do not have a prominent Si/O interface (12-, 13-, 15-$M_\odot$), or have one further out (20-, 25-$M_\odot$), suggesting that the timing of the accretion and dip at the Si/O interface could be critical to explosion. However, with the addition of moderate rotation and perturbations to infall velocities, even these five non-exploding models explode, suggesting that all progenitors are close to criticality for explosion. We also explore the microphysical dependence for the 16-$M_\odot$ progenitor, finding that it does not explode if either IES, INS, or MB is not included. Even removing the many-body correction prevents explosion. However, in Burrows et al. (2018), we show that inclusion of the Fischer (2016) correction to the nucleon-bremsstrahlung and reducing the electron capture rate on heavy nuclei (Juodagalvis et al. 2010) leads to explosion, corroborating our proposal that all models are near criticality and that modest changes to inputs can lead to explosion.

We calculate explosion energies for the four exploding models, summing kinetic, internal, and gravitational energies over our grid and substracting the absolute value of nuclear binding energy. We correct for the binding energy of the exterior overburden. All but the 21-$M_\odot$ progenitor have positive explosion energies at the end of our simulation of order a few $\times 10^{50}$ ergs, and rising. The 17- and 19-$M_\odot$ progenitors are far from asymptoting and feature a corresponding rise in kinetic energy, suggesting the need to carry these calculations out on larger grids and for longer times to estimate final explosion energies. Furthermore, we see that the more energetically explosive models have multiple convective plumes with larger solid angles. Together with the rise in kinetic energy, this suggests that more isotropic morphology of outflow is significant in producing larger explosion energies. The gain region properties of exploding models further distinguish them from the non-exploding models, with the former growing in gain mass following explosion with correspondingly higher heating efficiencies.

Together with the low-mass progenitors models from Radice et al. (2017), we show that lower-mass progenitors tend to have higher shock velocities and consequently, less dwell time of the neutron-rich ejecta for neutrino processing. This produces Y_e-ejecta mass histograms skewed towards lower Y_e for the lower mass progenitors. We also find no evidence for Lepton-number Emission Self-sustained Asymmetry (LESA), finding rather that the dipole moment of the net neutrino number is an order of magnitude smaller than found in Tamborra et al. (2014a).

We find that PNS masses track accretion history and are systemically larger for non-exploding or later-exploding models. PNS radii, however, are largely insensitive to input physics, but are sensitive to dimensionality, with 1D models asymptoting to a smaller PNS radii than their 2D counterparts. Radice et al. (2017) found similar behavior for their set of low-mass progenitors, citing convection in the PNS in 2D for the larger PNS radii. Including the many-body effect, however, does lead to a faster PNS contraction rate.

We concluded by exploring 1D comparisons to our four exploding models in 2D. None of the models explodes in 1D. The electron- and anti-electron-type neutrino luminosities dip in 2D post-explosion, as accretion is reversed. The "ν_μ"-type neutrino luminosities, however, are consistently higher, attributed to inner convection in the PNS. Mass, heating rate, and heating efficiency rise post-explosion for the exploding 2D models, but not for their 1D counterparts.

In the near future, we will explore these progenitor models in 3D using Fornax. Early multi-group 3D simulations either did not explode, or exploded later; more recent simulations illustrate that 3D progenitors are only slightly less explosive (see review by Müller 2016). The inclusion of detailed microphysics, including the many-body effects, together with multi-dimensional neutrino transport, may bridge this gap. Moreover, we will explore whether 3D simulations produce more isotropic explosions and larger explosion energies that closely reproduce what we see in Nature.

Chapter 4

CCSNe in 3D: Towards Full-Fidelity Models

4.1 Introduction

The neutrino mechanism of core-collapse supernovae (CCSNe) was proposed more than fifty years ago (Colgate & White 1966), but due to the complexity and exotic character of the environment in which it occurs and the realization that hydrodynamic instabilities and turbulence are crucial to explosion in all but a small subset of progenitor stars, credible confirmation of this mechanism and its observational validation have been frustratingly slow. Along with the requirement to incorporate nuclear and particle physics that does justice to the wide range of relevant neutrino-matter interactions and to the equation of state of dense nuclear matter, the centrality of turbulent convective and shock instabilities that break spherical symmetry has necessitated performing theoretical simulations in multiple spatial dimensions. The two-dimensional (2D) simulations (axisymmetric) of the 1990's lacked detailed neutrino physics, but demonstrated the relevance of neutrino-driven convection (Herant et al. 1994; Burrows et al. 1995). The early years of this millenium introduced an-

other instability (the standing-accretion shock instability, Blondin et al. 2003) and subsequent work built on previous 2D efforts by incorporating general relativity (GR, at various levels of approximation), improving the physical fidelity of the neutrino interactions embedded into the codes, enhancing the spatial resolution of the calculations, and carrying simulations out to later physical times. Summaries of some of this history can be found in reviews by Janka (2012), Burrows (2013), Müller (2016), and Janka et al. (2016). In fact, progress in understanding the CCSN mechanism has paralleled progress in both physics and computational capability, and such progress has spanned decades. It is only recently that fully three-dimensional (3D) simulations with multi-group neutrino transfer that address all the physical terms and effects, employ state-of-the-art nuclear equations-of-state, and calculate for a physically significant duration have emerged. Though there is still much work to do, the recent advent of codes that address the full dimensional and physics requirements of the CCSN problem represents a watershed in the theoretical exploration of the supernova mechanism. In this Chapter, we present one such modern simulation of the explosion in 3D of a 16-$M_\odot$ star, using our new supernova code Fornax (Skinner et al. 2016; Radice et al. 2017; Vartanyan et al. 2018b; Burrows et al. 2018; Morozova et al. 2018b).

State-of-the-art calculations in 3D exploring the mechanism of CCSN explosions have undergone significant evolution and improvement over the years. Sixteen years ago, Fryer & Warren (2002, 2004) used a smooth-particle hydrodynamics code SNSPH to explore the differences between 2D and 3D simulations and the possible role of rapid rotation. They found their 2D and 3D simulations were similar and that rapid rotation modified the driving core neutrino emissions. However, these simulations employed gray radiation, did not include inelastic energy redistribution nor velocity dependent transport effects, and ignored GR effects. Parameterized studies in 3D (Nordhaus et al. 2010; Dolence et al. 2013; Hanke et al. 2012; Couch & O'Connor

2014; Couch & Ott 2015) disagreed on the relative difficulty of explosion in 3D vs. 2D. However, these simulations, while boasting improved hydrodynamics algorithms and resolution, used "lightbulb" neutrino driving and did not employ competitive neutrino transfer and microphysics. Using ZEUS-MP on a low-resolution 3D grid, Takiwaki et al. (2012) witnessed the explosion of a 11.2-$M_{\odot}$ progenitor (Woosley et al. 2002). However, these authors used the sub-optimal IDSA scheme neutrino transport approach (Liebendörfer et al. 2009), which ignores velocity-dependence, GR, and inelasticity, stitches together the opaque and transparent realms in an ad hoc fashion, uses the problematic "ray-by-ray" approach to multi-D transport, and either neglects "heavy" neutrinos or incorporates them in a "leakage" format. The ray-by-ray approach used by many early and current studies performs multiple one-dimension transport calculations, in lieu of truly multi-D transport, and thereby ignores the important effects of lateral transport (Skinner et al. 2016).

Using the CHIMERA code, Lentz et al. (2015) witnessed the explosion of a 15-$M_{\odot}$ progenitor star (Woosley & Heger 2007) ∼300 milliseconds (ms) after bounce, ∼100 ms later than their 2D simulation. These authors used state-of-the-art microphysics and approximate GR, but used multi-group flux-limited diffusion and the reduced-dimension ray-by-ray approach and evolved the inner 6-8 kilometers (km) in spherical symmetry. In addition, they employed the LS220 equation of state (EOS) (Lattimer & Swesty 1991), now known to be inconsistent with known nuclear systematics.

Early low-resolution 3D simulations using the Prometheus-Vertex code (Hanke et al. 2013; Tamborra et al. 2014a) found that the 11.2-, 27- (Woosley et al. 2002), and 25-$M_{\odot}$ (Woosley & Heger 2007) non-rotating progenitors did not explode in 3D, while their 2D counterparts did. Prometheus-Vertex uses state-of-the-art neutrino microphysics, a multi-group variable Eddington factor transport algorithm with approximate GR (Marek et al. 2006), but uses the ray-by-ray+ approximation to neutrino transport. Later, this group (Melson et al., 2015b) witnessed the explosion

of a zero-metallicity 9.6-$M_\odot$ progenitor in 3D, a model that explodes easily in 1D (Radice et al. 2017). By making a large strangeness correction to the axial-vector coupling constant in Prometheus-Vertex, Melson et al. (2015a) were able to generate an explosion in 3D of the non-rotating 20-$M_\odot$ progenitor that did not otherwise explode. However, such a large correction may be inconsistent with nuclear experiment (Ahmed et al. 2012; Green et al. 2017). Recently, this group (Summa et al. 2018) has found that rapidly rotating progenitor models (Heger et al. 2005) explode shortly after the accretion of the silicon-oxygen (Si/O) interface. They argue, as do Takiwaki et al. (2016), that a strong non-axisymmetric spiral mode facilitates explosion in the rapidly-rotating context. However, with their default neutrino physics, this group has yet to witness the explosion in 3D of any non-rotating models using Prometheus-Vertex. Moreover, their 3D models were all calculated using the LS220 EOS.

Using the Coconut-FMT code in 3D, Müller (2015) witnessed the explosion of the 11.2-$M_\odot$ progenitor of Woosley et al. (2002) in 3D employing the LS220 nuclear EOS. However, Coconut-FMT employs simplified multi-group neutrino transport, the ray-by-ray approximation, neglects both velocity dependence in the neutrino sector and inelastic scattering, and cuts out the proto-neutron star (PNS) core. Its virtue is that it incorporates conformally-flat GR. Using Coconut-FMT and a 3D 18-$M_\odot$ initial progenitor to provide perturbations, Müller et al. (2017) witnessed what they interpret as a perturbation-aided explosion and the simulation was carried out to an impressive $\sim$2.5 seconds after bounce.

It is only recently that codes with truly multi-dimensional, multi-group transport, without the ray-by-ray compromise and with state-of-the-art microphysics and approximate or accurate GR, have been constructed and fielded. Roberts et al. (2016) used the adaptive-mesh-refinement (AMR) Cartesian code Zelmani with full GR, the M1 moment closure approach, the SFHo nuclear EOS (Steiner et al. 2013), but

without velocity dependence in the transport sector or inelastic scattering, to evolve the 27-$M_\odot$ progenitor of Woosley et al. (2002). Using the same code, Ott et al. (2018) explored the 12-, 15-, 20-, 27-, and 40-$M_\odot$ progenitor models of Woosley & Heger (2007). This team witnessed the low-energy explosion of all models, save the 12-$M_\odot$ model. More recently, Kuroda et al. (2016b) have developed a multi-group radiation-hydrodynamic CCSN code with M1 closure, detailed microphysics, and full GR. However, their recent CCSN simulations (Kuroda et al. 2016a) of 11.2-, 40- (Woosley et al. 2002), and 15-$M_\odot$ (Woosley & Weaver 1995) progenitors were done with gray transport and none of their models exploded. A related code using the FLASH architecture, AMR, state-of-the-art microphysics, approximate GR, and M1 transport more recently witnesses no explosion for a 20-$M_\odot$ progenitor, but noted large asymmetries in the Si and O shells that might dynamically aid explosion (O'Connor & Couch 2018a).

We present the first results in a series of 3D simulations that employ our new code FORNAX (Skinner et al. 2019). FORNAX is a multi-group, velocity-dependent neutrino transport code that employs the M1 two-moment closure scheme. It incorporates state-of-the-art neutrino microphysics, approximate GR (with gravitational redshifts), inelastic energy redistribution via scattering, and does not employ the ray-by-ray simplification. Furthermore, it uses a dendritic grid that deresolves in angle upon approach to the core, while maintaining good zone sizes. This allows us to include the stellar center while employing a spherical grid but without incurring an onerous Courant time step penalty. We find that the 16-$M_\odot$ progenitor (Woosley & Heger 2007) explodes in 3D, and does so shortly before its 2D counterpart.

Throughout this Chapter, we explore the dimensional dependence (2D vs. 3D) of the explosion properties. We organize the Chapter as follows: In §4.2, we outline the setup of our simulation. We explore the basic explosion properties in the beginning of §4.3 and the shock evolution in §4.3.1. In §4.3.2 and 4.3.3, we explore the explosion

energetics and heating rates and the luminosities and mean energies, respectively. We look at the ejecta composition in §4.3.4, and study PNS convection in §4.3.5. We comment in §4.3.6 on the possibility of the lepton-number emission self-sustained asymmetry (LESA; Tamborra et al. 2014a) in our 3D simulation and the lack of the standing accretion-shock instability (SASI). In §4.4, we conclude with summary comments and observations.

4.2 Numerical Setup and Methods

The progenitor upon which we focus is the 16-$M_\odot$ model of Woosley & Heger (2007) (which was studied in 2D in Vartanyan et al. 2018b), and we employ the state-of-the-art multi-D, multi-group radiation/hydrodynamic code Fornax (Skinner et al. 2018). Earlier supernova work using Fornax includes Wallace et al. 2016 (neutrino breakout burst detection), Skinner et al. 2016 (shortcomings of the ray-by-ray approximation in core-collapse simulations), Radice et al. 2017 (low-mass CCSNe), Burrows et al. 2018 (the role of microphysics in CCSNe), Morozova et al. 2018b (gravitational wave signatures of CCSNe), Vartanyan et al. 2018b (CCSNe from 12-25 $M_\odot$), and Seadrow et al. 2018 (neutrino detection of CCSNe).

Fornax is a multi-dimensional, multi-group radiation hydrodynamics code originally constructed to study core-collapse supernovae and its structure, capabilities, and variety of code tests are described in Skinner et al. (2019). In 2D and 3D, Fornax employs a dendritic grid which deresolves at small radii and in 3D along the ϕ axis to avoid overly-restrictive CFL time step limitations, while at the same time preserving cell size and aspect ratios. Our method of deresolving near the polar axis for 3D simulations allows us to partially overcome axial artifacts seen conventionally in 3D simulations in spherical coordinates (see, e.g. Lentz et al. 2015; Müller et al. 2017). Fornax solves the comoving-frame velocity-dependent transport equations to order

O(v/c). The hydrodynamics uses a directionally-unsplit Godunov-type finite-volume scheme and computes fluxes at cell interfaces using an HLLC Riemann solver. For the 3D simulation highlighted here, we employ a spherical grid in r, θ, and ϕ of resolution 608×128×256. For the comparison 2D simulation, the axisymmetric grid has resolution 608×128. The radial grid extends out to 10,000 kilometers (km) and is spaced evenly with $\Delta r \sim 0.5$ km for r $\lesssim$ 50 km and logarithmically for r $\gtrsim$ 50 km, with a smooth transition in between. The angular grid resolution varies smoothly from $\Delta\theta \sim 1.9^\circ$ at the poles to $\Delta\theta \sim 1.3^\circ$ at the equator, and has $\Delta\phi \sim 1.4^\circ$ uniformly. For this project, we used a monopole approximation for relativistic gravity following Marek et al. (2006) and employed the SFHo equation of state (Steiner et al. 2013), which is consistent with all currently known nuclear constraints (Tews et al. 2017).

We solve for radiation transfer using the M1 closure scheme for the second and third moments of the radiation fields (Vaytet et al. 2011) and follow three species of neutrinos: electron-type (ν_e), anti-electron-type ($\bar{\nu}_e$), and "ν_μ"-type (ν_μ, $\bar{\nu}_\mu$, ν_τ, and $\bar{\nu}_\tau$ neutrino species collectively). We use 12 energy groups spaced logarithmically between 1 and 300 MeV for the electron neutrinos and to 100 MeV for the anti-electron- and "ν_μ"-neutrinos.

Here, we initially evolve collapse in 1D until 10 ms after bounce, and then map to higher dimensions. After mapping, we impose velocity perturbations (for the 2D and 3D, but not 1D, simulations) following Müller & Janka (2015) in three spatially distinct regions ($50 - 85$ km, $90 - 250$ km, and $260 - 500$ km), with a maximum speed of 500 km s^{-1} and harmonic quantum numbers of $l = 2$, $m = 1$, and $n = 5$ (radial), as defined in Müller & Janka (2015). These perturbations were motivated by Müller et al. (2016b), who evolve the last minutes of a 3D progenitor and find convective velocities of almost 1000 km s^{-1} at the onset of collapse (with a corresponding Mach number of 0.1) in the O-shell around 5000 km with a prominent $l = 2$ mode.

Our 3D simulation was evolved to 677 ms after core bounce, and required a total resource burn of ∼18 million CPU-hours on the NERSC/Cori II machine using 16256 cores in parallel. [1]

We note that the 16-$M_\odot$ progenitor was studied in Ch. ch:2DVartanyan et al. (2018b), but with a different setup. There, we did not include initial velocity perturbations, had 20 (instead of 12) energy bins per neutrino species, and employed an angular resolution of 256 polar cells (instead of 128). We also did not map from 1D to 2D 10 ms after bounce, but evolved entirely in 2D. Our grid then extended to 20,000 km (not 10,000 km). For the 2D comparison model, we maintain these differences to mimic the setup we use for our concurrent 3D run. However, we obtain the same overall results for the 16-$M_\odot$ progenitor seen in Vartanyan et al. (2018b).

4.3 Explosion Properties

We find that the 16-$M_\odot$ progenitor of Woosley & Heger (2007) explodes in both the corresponding 2D and 3D simulations, at ∼100 and ∼120 ms after bounce, respectively. The corresponding 1D simulation does not explode. The explosions in 2D and 3D are abetted by the inclusion of detailed microphysics − in particular, inelastic scattering off electrons, nucleons, and the associated energy redistribution, and the decrease in the neutral-current neutrino-nucleon scattering rates due to the many-body effect (Burrows et al. 2018; Horowitz et al. 2017) − as well as a steep density gradient at the silicon-oxygen interface located deep within the progenitor, near an interior mass of ∼1.5-$M_\odot$ (Vartanyan et al. 2018b; Ott et al. 2018). Unlike in many recent 3D simulations, we use the SFHo equation of state in this work.

At the end of our 3D simulation, ∼677 ms after bounce, the maximum shock radius has reached ∼5000 km, with an asymptotic velocity of ∼10,000 km s^{-1}. The

[1] For comparison, some earlier 3D simulations (e.g., Summa et al. 2018 for a model with slightly lower resolution, but with rotation.) required ∼50−100 million CPU-hours to evolve to 0.5 seconds after bounce.

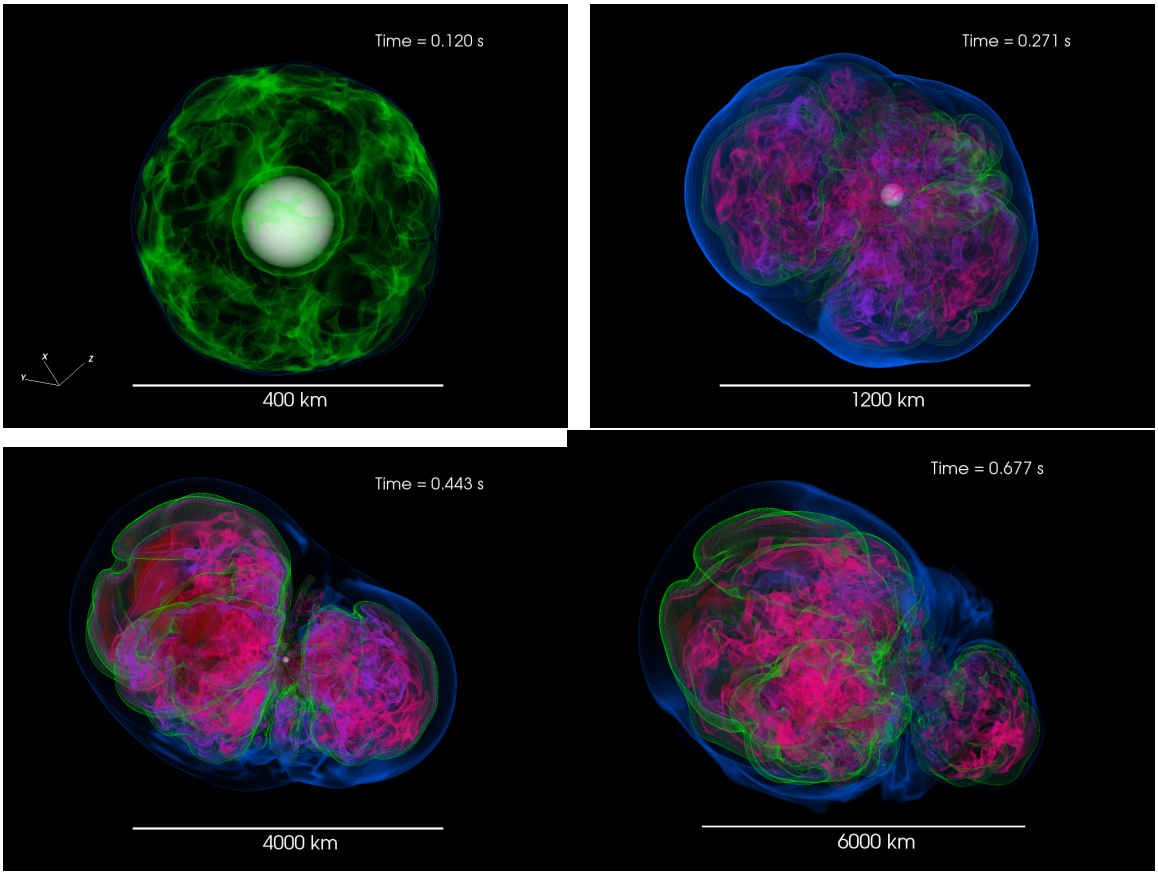

Figure 4.1: Time sequence of the entropy of the 16-$M_\odot$ progenitor. Note the different spatial scales. The inner white sphere is a 10^{11} g cm^{-3} isosurface that roughly delineates the PNS, and the blue veil traces an entropy contour of 4-k_b/baryon, a proxy for the shock radius. Note the bifurcated cerebral structure of the explosion plumes, with one dominant hemisphere (on the left in this projection). Several "fingers" are also visible along the axis, though these are accreted shortly after. Note the high-entropy regions (dark red) both along the outer cusps of the plumes and in the interior as matter is funneled onto the PNS.

diagnostic explosion energy is $\sim$1.7$\times$10^{50} erg by this time. The mass of the core ejecta, defined as neutrino-processed gravitationally unbound material, is $\sim$0.08 $M_\odot$ and growing. The corresponding gravitational PNS mass is $\sim$1.42 $M_\odot$ and the mean PNS radius $\sim$29 km. These features are explored in greater detail in the later sections and compared to the results in 2D. In all regards, we find that integrated 3D metrics are significantly less variable with time than their 2D analogs.

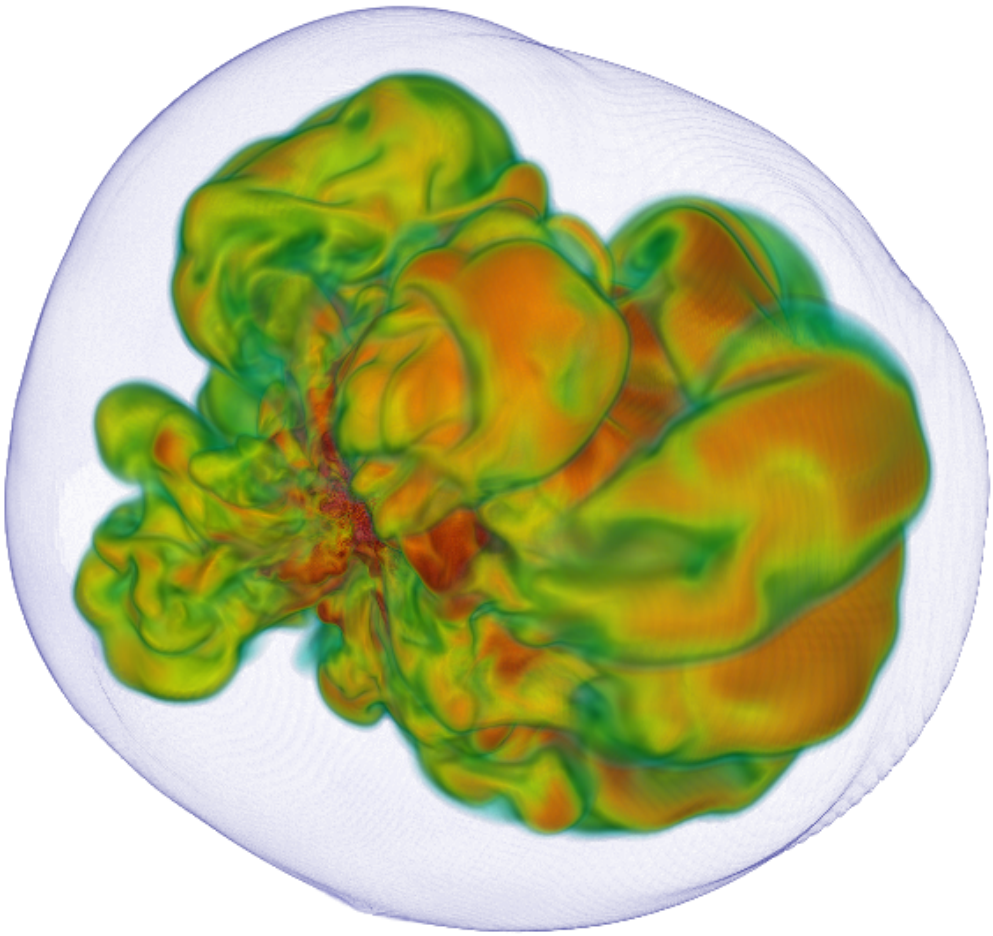

Figure 4.2: Volume rendering of the entropy per baryon showing the morphology of the explosion of the 11-$M_\odot$ progenitor from Sukhbold et al. (2018). The snapshot is taken at ∼690 ms after bounce, when the shock wave (blue outer surface in the figure) has an average radius of ∼3500 km. The shock is expanding quasi-spherically, however accretion continues on one side of the PNS, while neutrino-driven winds inflate higher-entropy bubbles on the other side.

In Fig. 4.1, we show a time sequence of the entropy of the 3D simulation, illustrating the highly non-axisymmetric nature of the explosion. By ∼100 ms after bounce, shock expansion and explosion are underway, with the outflow initially constituting bubbles interior to the shock. The explosion assumes a bi-cameral structure, with the two hemispheres separated by a plane oriented with θ ∼40° and ϕ ∼50° in spherical coordinates. Unlike in 2D, the explosion does not orient around any coordinate axis and there is no axial sloshing; any explosion axis that emerges does so naturally and is not imposed. Indeed, the explosion is not isotropic, but has a preferred direction, clockwise-orthogonal to the dividing plane. The left hemisphere (in this projection) dominates and we see some fingers along the axis at ∼443 ms (3rd panel), but these are accreted soon after. The electron fraction distribution follows the entropy distribution, with high Y_e ($Y_e > 0.53$) concentrated along the outer cusps of each plume (see §4.3.4). We see high-Y_e material in both plumes as well as in the interior.

We show in Fig. 4.2 a volume rendering of the entropy per baryon showing the morphology of the explosion of the 11-$M_\odot$ progenitor from Sukhbold et al. (2018) from an upcoming paper (Burrows et. al, 2018). The snapshot is taken at ∼690 ms after bounce, when the shock wave (blue outer surface in the figure) has an average radius of ∼3500 km. The explosion behaves similarly to that of the 16-$M_\odot$ progenitor we evolve. The shock is expanding quasi-spherically; however, accretion continues on one side of the PNS, while neutrino-driven winds inflate high-entropy bubbles on the other side.

In Fig. 4.3, we illustrate a time sequence of entropy slices for the 3D simulation of the 16-$M_\odot$ progenitor along the x-y plane (top). At early times, shock breakout is driven by multiple smaller bubbles in 3D, as opposed to a few large plumes in 2D. The shock evolution in 3D transitions from quasi-spherical expansion to expansion along an axis, with the axis randomly chosen. By ∼300 ms after bounce, the plumes in 3D have merged into two distinct larger-solid-angle bubbles oriented along a clear

axis. We see matter cross and accrete through this axis at earlier times before the explosion settles into the final configuration (see panels 3-5 of Fig. 4.3). At late times in the 3D simulation, we see the larger plume growing relative to the smaller, leaving a dominant driving plume. This is similar to the behavior in 2D. A persistent wind that emerges ∼300 ms after bounce is present in both the large and small explosion plumes, and finally in the dominant plume alone. We see simultaneous explosion and accretion − the smaller plume in Fig. 4.3 growing relatively in size. Even up to the end of our simulation, some material partially circumnavigates the explosion plumes, plunges inward in a sheet that seems to pinch off the larger from the smaller plume, and is accreted onto the PNS. This accretion pinching in the early explosion phase between the two differently-sized exploding plumes resembles a wasp's waist and may be a common feature of some CCSN explosion morphologies. The smaller plume is more prominent in 3D than in 2D, for which at late times the opposing explosion plume's volume ratio is significantly smaller than in 3D.

An inner structure with two counter-ejected large lobes such as we see in this simulation, with one demonstrably larger than the other, crudely resembles the iron ejecta pattern inferred from XMM X-ray observations of the supernova remnant (SNR) Cas A (Willingale et al. 2003). This is suggestive, but the remnant structure in any SNR depends upon its entire propagation history through the star's matter field and any apparent morphological association between early and late ejecta patterns could be happenstance. This remains to be determined. However, the rough similarity between our preliminary debris field morphology and the inferred inner mass density and composition patterns from X-ray data is indeed intriguing.

The 3D simulation has lower maximum entropies at late times by ∼4.5 units (Boltzmann constant (k_B) per baryon) than its 2D counterpart. However, the entropy averaged over the shocked region (defined where the specific entropy is greater than 4 k_B per baryon) is comparable for both simulations. This is because the 3D simulation

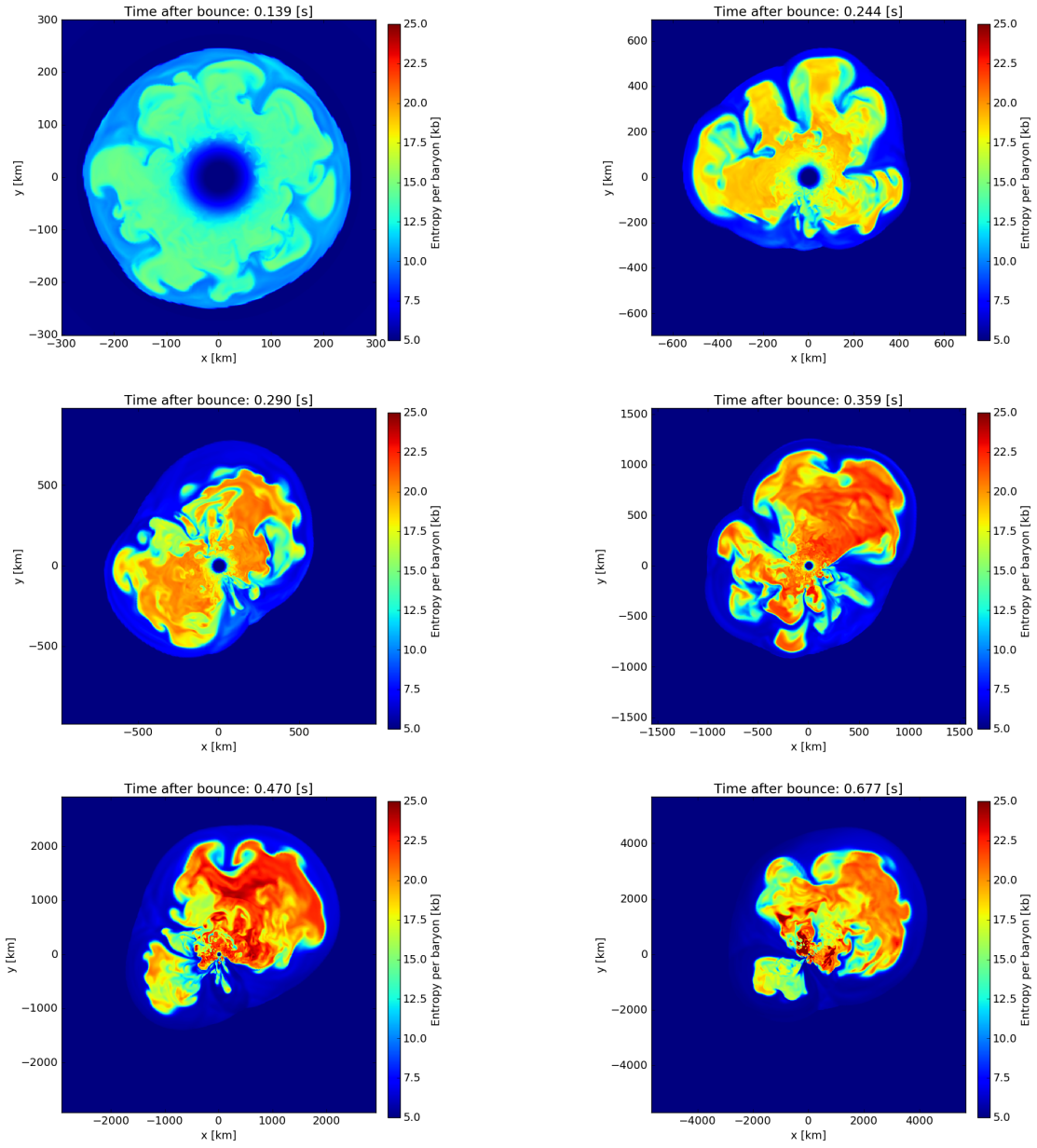

Figure 4.3: Time sequence slices in the x-y plane illustrating the entropy of the 3D simulation of the 16-$M_\odot$ progenitor. Note the changing spatial scales with time. At early times, shock expansion is driven by multiple bubbles, which coalesce into larger plumes. At approximately 300 ms after bounce, we note the development of a dividing axis with two dominant plumes in this slicing. At late times, a single dominant explosion plume emerges, seemingly at the expense of the secondary plume. A persistent wind is present in both plumes initially, and finally, only in the dominant plume. The secondary plume persists and grows, with a characteristic scale of $\sim$2000 km, half the size of the primary plume at the end of our simulation. We see simultaneous explosion and accretion. The shock evolution transitions from quasi-spherical expansion to axial expansion, with the axis arbitrarily chosen. See the text for a discussion.

maintains a more 'isotropic' explosion in that even the subdominant plume subsists, producing comparable mean entropies over the shocked region despite the higher entropies along the dominant axial plume in 2D.

4.3.1 Shock Wave Evolution

We find, perhaps surprisingly (Hanke et al. 2012, 2013; Dolence et al. 2013) that our 3D model explodes roughly 50 ms earlier than the corresponding 2D model. In the top panel of Fig. 4.4, we plot the angle-averaged shock radius versus time after bounce for the 2D (dashed, blue swath) and 3D (solid, green swath). The colored-in areas indicate the radial spread of the shock location, from minimum to maximum. At the end of our 3D simulation, the mean shock radius has reached beyond ∼5000 km. The 2D model remains roughly spherical in expansion for the first ∼120 ms, whereas the 3D model deviates from spherical symmetry earlier. We show in the inset a zoomed-in plot of the average shock radii at early times. The shock radii for the 2D and 3D simulations diverge around ∼50 ms after bounce. The shock of the 3D model barely stalls, while the shock for its 2D counterpart stalls for ∼50 ms.

In the bottom panel of Fig. 4.4, we plot the first four spherical harmonics of the shock radius as a function of time after bounce. We take the norm over all orders m and compare 3D (solid) with 2D (dashed). We use the approach outlined in Burrows et al. (2012) to decompose the shock surface $\mathrm{R}_s(\theta, \phi)$ into spherical harmonic components with coefficients:

$$a_{lm} = \frac{(-1)^{|m|}}{\sqrt{4\pi(2l+1)}} \oint R_s(\theta, \phi) Y_l^m(\theta, \phi) d\Omega \,, \tag{4.1}$$

normalized such that $a_{00} = a_0 = \langle R_s \rangle$ (the average shock radius) and a_{11}, a_{1-1}, and a_{10} correspond to the average Cartesian coordinates of the shock surface $\langle x_s \rangle$, $\langle y_s \rangle$,

and $\langle z_s \rangle$, respectively. The orthonormal harmonic basis functions are given by

$$Y_l^m(\theta,\phi) = \begin{cases} \sqrt{2} N_l^m P_l^m(\cos\theta)\cos m\phi & m > 0\,, \\ N_l^0 P_l^0(\cos\theta) & m = 0\,, \\ \sqrt{2} N_l^{|m|} P_l^{|m|}(\cos\theta)\sin|m|\phi & m < 0\,, \end{cases} \tag{4.2}$$

where

$$N_l^m = \sqrt{\frac{2l+1}{4\pi}\frac{(l-m)!}{(l+m)!}}\,, \tag{4.3}$$

$P_l^m(\cos\theta)$ are the associated Legendre polynomials, and θ and ϕ are the spherical coordinate angles. We plot the norm,

$$P_\ell = \frac{\sqrt{\sum_{m=-\ell}^{\ell} a_{\ell m}^2}}{a_{00}}\,. \tag{4.4}$$

Up to ∼70 ms after bounce, the $\ell = 2, 4$ moments dominate, the former due to the initial quadrupolar velocity perturbations imposed. From ∼100 to ∼200 ms, all moments are comparable in magnitude. Note that the dip in the quadrupole moment at ∼300 ms corresponds to the dip in mean shock radius seen in the left panel. Shortly afterwards, the shock surface of the 2D simulation rapidly expands, catching up with that of the 3D simulation. At late times, the large-scale, lower ℓ moments dominate. Up to $\ell = 11$ (not shown), we find that the moment magnitudes decrease monotonically with increasing ℓ (and decreasing angular scale). We witness a transition from small structures at early times, coalescing into large-scale structures at later times. As the explosion commences, the 3D simulation evinces larger deviations from spherical symmetry than the 2D simulation, as indicated by the larger magnitudes of the respective moments. However, at late times the 2D simulation begins to manifest larger asymmetries than its 3D counterpart, indicated by the larger magnitude of the lower-order moments. Both simulations have similar asymptotic shock velocities

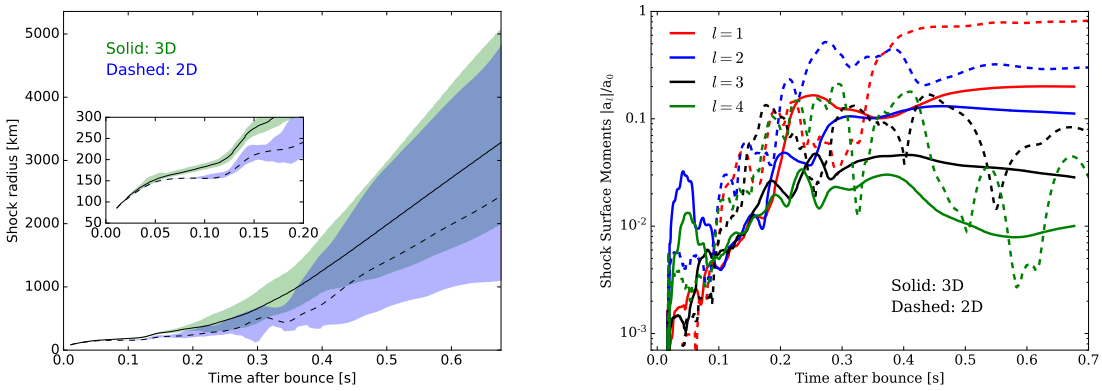

Figure 4.4: **Left**: The shock radius (km) vs. time after bounce (in seconds) for the 2D (dashed, blue swath) and 3D (solid, green swath). The colored-in regions indicate the range of the shock location, from minimum to maximum. The 3D simulation explodes slightly earlier. At the end of our simulation, the shock achieves ∼5000 km. The shock of the 3D model barely stalls in radius, while the shock for its 2D counterpart stalls for ∼50 ms. We show in the inset a zoomed-in plot of the average shock radii at early times. The mean shock radii for the 2D and 3D simulations have diverged by ∼50 ms after bounce. **Right**: The first four spherical harmonic moments of the shock radius as a function of time (in seconds) after bounce, normalized to the mean shock radius (the $\ell = 0$ component). We take the norm over all orders m and compare 3D (solid) to 2D (dashed). Up to ∼70 ms after bounce, the $\ell = 2, 4$ moments dominate, the former due to the initial quadrupolar velocity perturbations imposed. From ∼100 to ∼200 ms, all reduced moments are comparable in magnitude. At late times, the large scale, lower-ℓ moments increase in significance. Up to $\ell = 11$ (not shown), we find monotonically decreasing relative moment magnitudes with increasing ℓ (and decreasing angular scale). We see a transition from small structures at early times to large structures at later times. Up to explosion, the 3D simulation evinces much larger deviations from spherical symmetry. At late times, however, the 2D simulation shows much larger asymmetries than the 3D simulation, indicated by the larger magnitude of the reduced moments.

and maximum shock radii (at a given post-bounce time), though the 2D simulation minimum and average shock radii are roughly ∼1000 km smaller.

In Fig. 4.5, top panel, we track the dipole orientation of the shock with time. Early on, the shock dipole vector changes sporadically (but does not simply jump up and down as in 2D), but at later times it settles to an axis seemingly chosen arbitrarily. The randomly chosen axis is a defining feature of 3D non-rotating simulations (see, e.g. Fig. 3 in Burrows et al. 2012). We also see pronounced azimuthal structures in the 3D simulation (as opposed to rings in 2D). Along with the $\ell = 0$ explosion mode, the $\ell = 1, m = -1$ dipolar mode dominates at late times, and we see such a structure in the 3D explosion maps (Fig. 4.1).

In Fig. 4.5, bottom panel, we show Mollweide projections of the accretion rate for the 3D and 2D models. The spatial variations for the 3D simulation for the accretion rate contrast sharply with that for the 2D simulation, in which we see a dominant dipole component only in the southern hemisphere.

4.3.2 Energetics

Before explosion, the energy deposited in the gain region, that thick shellular volume interior to the shock wave where neutrino heating rate exceeds the cooling rate, is most relevant for driving turbulence and establishing the potential for explosion. The larger the energy deposition rate, the closer a given progenitor model is (with its mass accretion rate) to explosion (Burrows & Goshy 1993). However, the total energy deposited in advance of explosion is not related to the explosion energy (Burrows et al. 1995). The matter heated in the gain region is subsequently advected into the PNS, where it first reradiates a fraction of the acquired energy and then merges with the radiating PNS. It is only after the explosion commences that the deposited energy might be retained to contribute to the asymptotic explosion energy. However, even though explosive expansion leads to diminished cooling as the matter temperatures decrease,

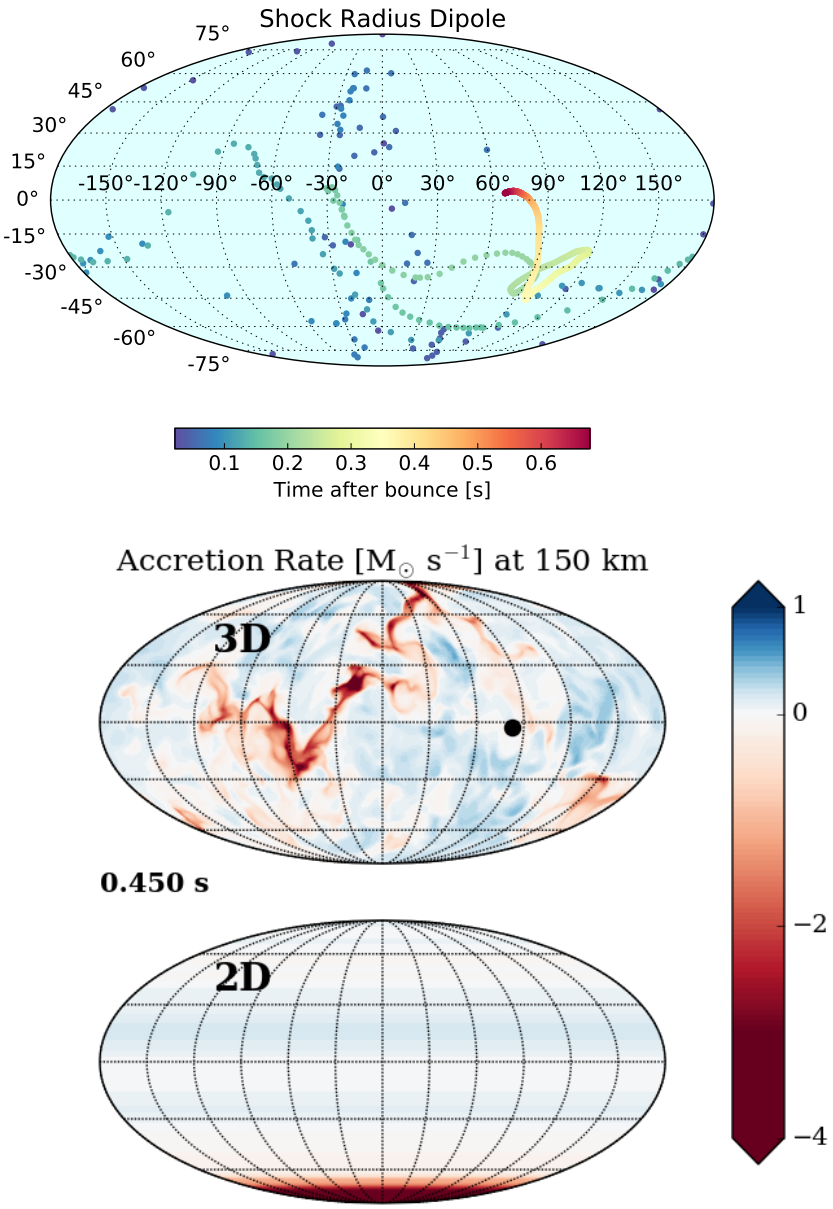

Figure 4.5: **Top**: A Mollweide projection of the direction of the shock dipole as a function of time (in seconds) after bounce, color-coded. Early on, the shock dipolar direction is changes sporadically before settling at late times to a randomly chosen axis. See Fig. 3 of Burrows et al. (2012) for a comparison. Note that, in a 2D simulation, the dipole axis is required to lie along the z-axis; this is not the case in a 3D simulation. **Bottom**: Mollweide projections of the accretion rate for the 3D and the 2D simulations at 450 ms after bounce. The spatial variation of accretion rate in the 3D simulation is in sharp contrast with the accretion rate in the 2D simulation, where we see only a dominant dipole component in the southern hemisphere.

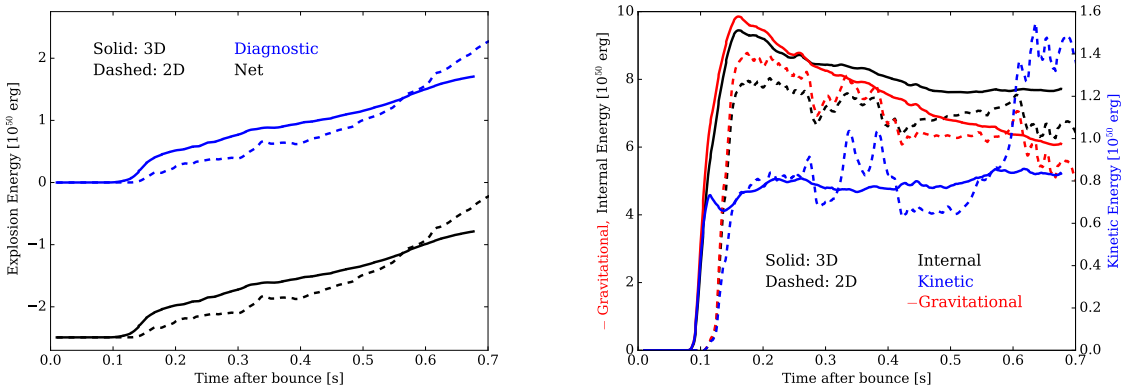

Figure 4.6: **Left**: Diagnostic (blue) and net (black) explosion energies (in 10^{50} erg) for the 16-$M_\odot$ progenitor as a function of time after bounce (in seconds). **Right**: Internal (blue, left y-axis) and kinetic (green, right y-axis) energies (in 10^{50} erg) as a function of time after bounce (in seconds). Solid indicates the 3D model and dashed the corresponding 2D model for both figures. The diagnostic energy (left, green) does not account for the gravitational overburden of $\sim 2.5 \times 10^{50}$ erg exterior to our simulation grid (outer boundary 10,000 km). The total explosion energy (blue) is not yet positive for the 3D simulation (at 677 ms after bounce), though the 3D simulation explodes slightly earlier. The 3D simulation maintains a higher internal energy, by $\sim$15%, through the end of the simulation, and a higher explosion energy, but similar kinetic energies, until $\sim$550 ms after bounce. The subsequent rise in explosion energy for the 2D model corresponds with the steep rise in its kinetic energy, also seen in Vartanyan et al. (2018b) for the same 16-$M_\odot$ progenitor, but with a different initial setup. Such a sharp rise in kinetic energy is not seen in our 3D simulation.

there continues to be some neutrino cooling. More importantly, the exploding matter expands against gravity, so that much of the ongoing neutrino energy deposited is used to lift the matter out of the deep potential well. This explains why the neutrino heating rates even during explosion are larger than the accumulation rate of the supernova blast energy in the first seconds of the explosion phase. Recombination of the nucleons into nuclei will provide a boost ($\sim$9 MeV per baryon) to the asymptotic kinetic energy of the supernova ejecta, but the associated recombining mass is generally not large (here $\sim$0.08 $M_\odot$). Moreover, the associated total energy is comparable to the gravitational binding term. As a result, it appears that the supernova will take many seconds to achieve its final energy. Therefore, even though our 3D simulation of this 16-$M_\odot$ progenitor's core has been conducted farther post-bounce than any

other simulation with state-of-the-art numerics and microphysics, we have captured only the early stages of an explosion that will need to be followed numerically for a few more seconds to witness the asymptoting of the explosion energy (Müller 2016; Müller et al. 2017).

The total energy we plot in Fig. 4.6 is comprised of the kinetic energy, the thermal energy, the recombination energy, and the gravitational energy of the ejecta. The so-called "diagnostic" energy ignores the binding energy (thermal plus gravitational) of the progenitor exterior to the computational domain. Here, the total energy quoted includes this penalty, different for every progenitor and outer computational boundary radius; including this term is required to assess the true supernova explosion energy.

We calculate diagnostic energies for our 16-$M_\odot$ progenitor in 3D and 2D, summing the kinetic, thermal, gravitational, and nuclear binding energies interior to our 10,000-km simulation grid where the matter parcel's Bernoulli term is positive. We correct for the gravitational binding energy of 2.5×10^{50} erg exterior to our grid, and plot both the diagnostic (blue) and net (black) explosion energies in the left panel of Fig. 4.6. In the right panel, we plot the thermal (blue, left y-axis), gravitational (red, left y-axis) and kinetic (green, right y-axis) energies (in 10^{50} erg) as a function of time after bounce (in seconds). Solid indicates the 3D model and dashed the 2D analog for both figures.

The 3D model explodes slightly earlier and initially has a higher explosion energy than its 2D model counterpart (Fig. 4.6). At the end of the simulation, 677 ms after bounce, the 3D model has a diagnostic explosion energy of 1.7×10^{50} erg. Accounting for the gravitational overburden, the total explosion energy (blue) is not yet positive for the 3D simulation (-0.8×10^{50} erg). Before $\sim$550 ms after bounce, the 3D simulation maintains similar kinetic energies and a higher internal energy by $\sim$15% than its 2D analog. Thenabouts, the 2D model explosion energy overtakes that of the 3D model, with the rise in explosion energy corresponding to a steep rise in its

kinetic energy at a growth rate of $\sim 5 \times 10^{50}$ erg s^{-1}. Such a rise, also at $\sim$550 ms after bounce, is seen in Vartanyan et al. (2018b) for the same 16-M$_\odot$ progenitor, but with a different initial setup. It is not seen in our 3D simulation. We conjecture that the stronger dipole and quadrupole moments of the 2D simulation (Fig. 4.4, right) relative to those of the corresponding 3D model at late times contribute to this divergence in kinetic energy. At the end of our simulation, the explosion energy for the 3D model is climbing at a rate of approximately 2.5×10^{50} erg s^{-1}, half that of the 2D case. Similar energy growth rates are found for the 3D simulations in the literature (see, e.g. Müller et al. 2017) and necessitate continuing 3D simulations for several seconds.

In Fig. 4.7, top panel, we illustrate the heating rates and the gain mass as a function of time after bounce for the 3D (solid) and 2D (dashed) simulations of the 16-M$_\odot$ progenitor. Just prior to explosion, at $\sim$100 ms, the heating rate for the 3D simulation is $\sim$30% (2 Bethe s^{-1}) higher than for the corresponding 2D model. The gain mass is also slightly higher for the 3D model, exceeding 0.12 M$_\odot$ at the end of our simulation). After $\sim$150 ms post-bounce, we see more variability in the heating rate for the 2D simulation than for the 3D simulation. Through almost $\sim$700 ms after bounce, the growth rate of the explosion energy is less than 20% of the heating rate, the difference due to the work done against gravity by the ejecta. It is not until late times that the growth rate of the explosion energy is expected to be close to the heating rate. In the middle panel, we show the spread of the inner boundary of the gain region a function of time after bounce, defined here where the net heating (heating minus cooling) is greater than 10% of the heating alone. The 3D simulation (green, solid) maintains a much larger variation in radial boundary throughout the evolution, extending almost twice as far at late times as the 2D model. In the bottom panel, we show the heating efficiency η, defined as the heating rate divided by the luminosity entering the gain region,

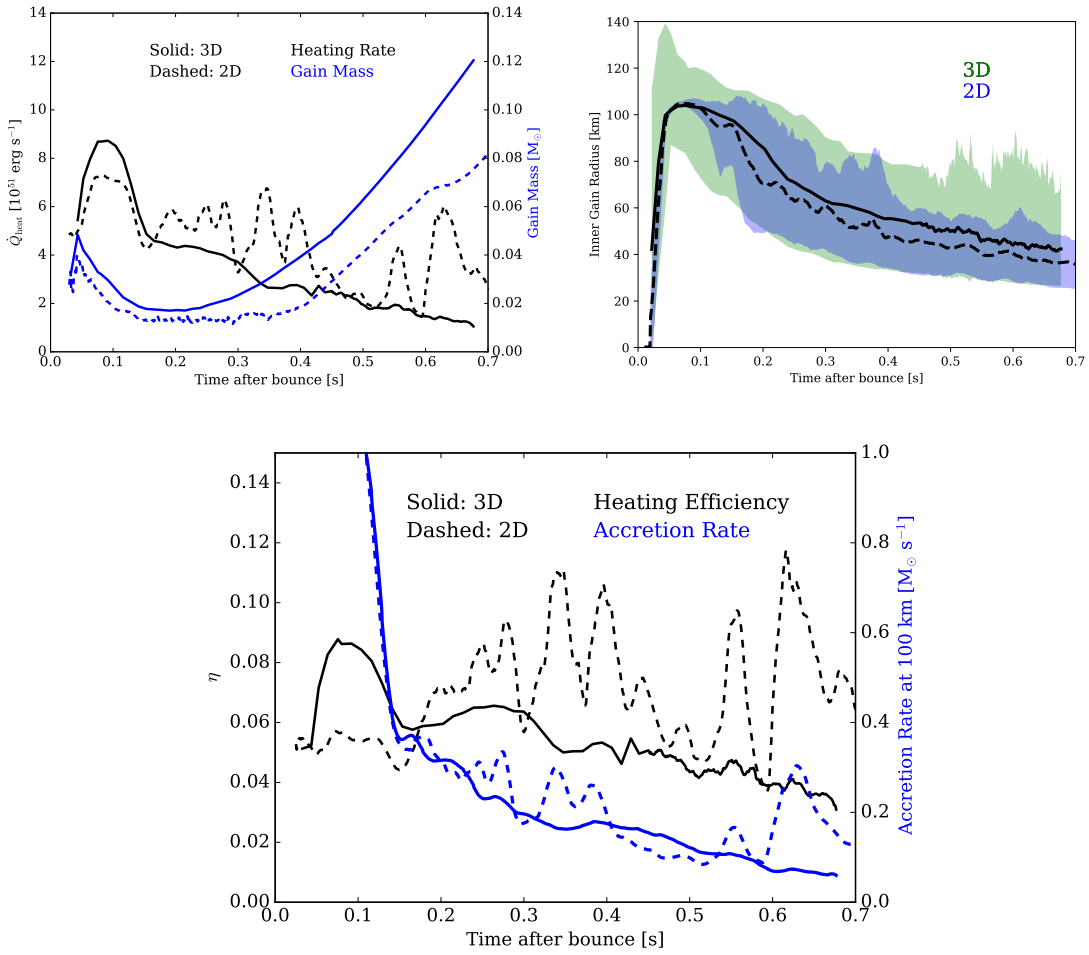

Figure 4.7: **Top left**: We illustrate the heating rates (blue, 10^{51} erg s^{-1}), and the gain mass (black, in 10^{-3} M$_\odot$) as a function of time after bounce (in seconds) for the 3D (solid) and 2D (dashed) simulations of the 16-M$_\odot$ progenitor. Prior to explosion ($\sim$100 ms), the heating rate for the 3D simulation is $\sim$30% higher than for the 2D simulation. The gain mass is also slightly higher for the 3D model, exceeding 0.12 M$_\odot$ at the end of our simulation. **Top right**: Inner boundary of the gain region (in km) as a function of time after bounce (in seconds). Black lines depict the mean positions of the inner gain region (solid for 3D, dashed for 2D). The 3D simulation (green, solid) maintains a much larger variation of the inner boundary of the gain region throughout the evolution. **Bottom**: Heating efficiency η (black), defined as the gain-region heating rate divided by the sum of the ν_e and $\bar{\nu}_e$ luminosities entering the gain region, and the accretion rate at 150 km (blue, in M$_\odot$ s^{-1}). Through the first $\sim$150 ms, the 3D simulation (green) has a heating efficiency $\sim$40% higher than the 2D (blue) simulation. However, after $\sim$200 ms, the 2D simulation overtakes the 3D simulation, and showcases a high degree of variability over $\sim$50-ms time scales. Note the correlation between jumps in accretion rate and jumps in heating rates (and efficiencies) in the 2D simulation.

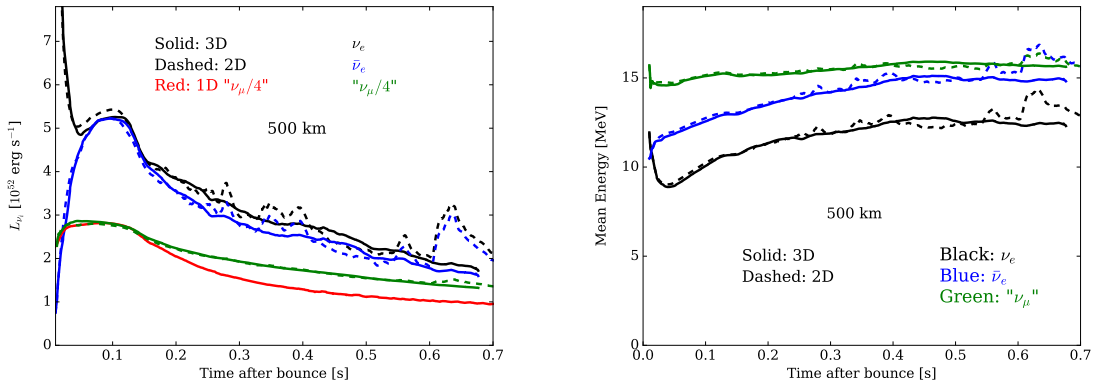

Figure 4.8: Neutrino luminosity (**left**, 10^{51} erg s^{-1}), and average neutrino energy (**right**, MeV) as a function of time after bounce (in seconds) at 500 km. Note that the luminosities and average energies for 2D and 3D are remarkably similar and show a significant difference only after 600 ms after bounce.

$$\eta = \frac{\dot{Q}_{heat}}{L_{\nu_e} + L_{\bar{\nu}_e}} \,. \tag{4.5}$$

Through the first ∼150 ms, the 3D simulation has a heating efficiency of ∼0.09, 40% higher than the corresponding 2D model. However, after 200 ms, the efficiency of the 2D simulation overtakes that of the 3D simulation, and showcases a high degree of variability with a time scale of ∼50 ms.

4.3.3 Luminosity and Mean Energies

In Fig. 4.8, we plot the luminosity (left) and mean energies (right) at a radius of 500 km as a function of time after bounce. Note that the luminosities and average energies for the 2D and 3D models are remarkably similar and show significant difference only beyond ∼600 ms after bounce. We note, however, key differences in the electron-neutrino luminosities through the first ∼150 ms, with the 2D simulation boasting a luminosity ∼7% larger than that for the 3D simulation. Furthermore, the 'heavy'-neutrino luminosity is ∼3% smaller for the 2D simulation than for the 3D

simulation over the same time period. We explore this more in Sec. 4.3.5. Here, we remark that the interplay between the greater electron-neutrino luminosity and the smaller 'heavy' neutrino luminosity in the critical first one-hundred ms of our 2D simulation (compared to our 3D model) impede earlier explosion revival in the 2D case. The former strips the gain region of energy deposition by neutrinos (since the electron-type neutrinos have a much higher absorption opacity than the 'heavy'-type neutrinos). Furthermore, the greater 'heavy'-neutrino luminosity in the 3D simulation may act in the same direction as the axial-vector many-body correction to produce a harder electron-neutrino spectrum and facilitate explosion (Burrows et al. 2018). The culmination of these effects is visible in Fig. 4.7, top panel, where a small difference in the respective luminosities translates into a significantly smaller heating rate in the 2D simulation compared to the analogous 3D simulation.

4.3.4 Ejecta Composition

Our calculations follow the evolution in space and time of the electron fraction, Y_e. This quantity is an essential determinant of subsequent nucleosynthesis. While we do not in this Chapter derive the detailed elemental composition of our ejecta, the distributions of the entropies and Y_es in the inner explosion debris provide qualitative information on the likely character of the emergent element burden. In our previous 2D simulations (Vartanyan et al. 2018b), histograms of the ejecta Y_e were derived. What we found was that much of the ejecta have Y_es above 0.5, implying that the ejected matter has been processed by differential ν_e and $\bar{\nu}_e$ absorption that has made some of it proton-rich. This is what we witness in this 3D simulation, though whether this is a generic outcome remains to be determined. Proton-rich ejecta could be a site of the p- and νp-processes (Pruet et al. 2006; Fröhlich et al. 2006; Wanajo et al. 2011) and might be the context for the production of some of the first peak of the

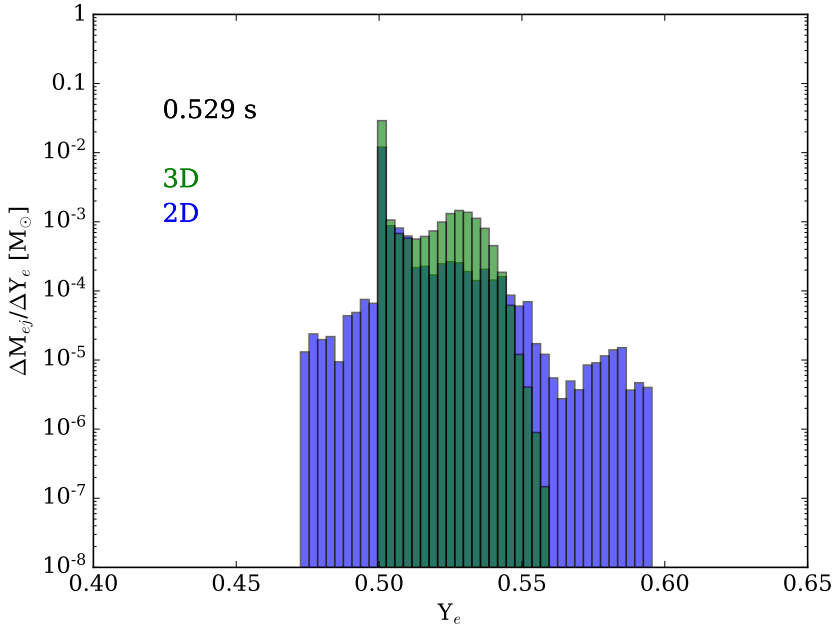

Figure 4.9: Histogram of ejecta mass distribution by Y_e at 0.529 seconds) after bounce. The green bars indicate the results of the 3D simulation, and the blue those for the 2D simulation. We find the interesting result that the ejecta mass distribution in 2D has a tail extending out to both higher (> 0.55) and lower (< 0.5) Y_e than the 3D simulation at a given time.

r-process (Hoffman et al. 1996; Pruet et al. 2006; Fröhlich et al. 2006; Wanajo et al. 2011; Frebel 2018; Bliss et al. 2018).

In Fig. 4.9, we provide a histogram of the ejecta mass distribution in Y_e at 0.529 seconds after bounce. The green bars indicate the results of the 3D simulation, and the blue bars that of the 2D simulation. Though both models peak at $Y_e = 0.5$, we find the interesting result that the ejecta distribution in the 2D model has a wider tail extending out to both higher (> 0.55) and lower (< 0.5) Y_e than the 3D simulation at any given time. For much of the evolution, the ejecta of the 3D simulation spans Y_e $\sim$0.5$-$0.55, whereas the ejecta in the 2D simulation encompasses $Y_e\sim$0.45$-$0.6.

Only at late times does the 3D simulation have significant low-Y_e ejecta at large radii (see the violet tail in Fig. 4.10). [2]

In Ch. ch:2D (on 2D models, Vartanyan et al. 2018b), we found that only the 16-$M_\odot$ progenitor had an ejecta-Y_e distribution that extended to lower Y_e, among the four progenitors considered. We claimed that an anisotropic explosion, with much of the outflow directed toward one hemisphere, would leave the opposite hemisphere with relatively untouched neutron-rich material. We see a similar result here. The 3D simulation, on the other hand, produces a more omnidirectional explosion − leaving little matter untouched. The achievement of higher Y_e in 2D can similarly be understood − the concentration of explosion in one direction in the 2D simulation allows ample neutrino processing of the ejecta to higher Y_e.

We illustrate the 3D distribution of Y_e in the ejecta in Fig. 4.10 at ∼667 ms after bounce. The white "veil" illustrates a Y_e of 0.5, just interior to the location of the shock radius. The high-Y_e plumes correspond to the high-entropy plumes of Fig. 4.1, with the blue plumes indicating Y_e's that span $0.5 - 0.52$, and the red blobs Y_e greater than 0.52. The latter is concentrated along the exterior cusps of the plumes, and in the interior where accretion is funneled onto the PNS. Note the resemblance of the high-Y_e distribution in Fig. 4.10 to the entropy distribution in Fig. 4.1.

4.3.5 Inner PNS Convection

The original delayed explosion mechanism of Wilson (1985) was facilitated by the enhancement of the driving neutrino luminosities by what he termed "neutron-finger" convection. This was a doubly-diffusive instability, akin to salt-finger convection in the oceans, that was suggested to result in an otherwise stably-stratified PNS. A Ledoux-stable balance of Y_e and entropy gradients was thought to be undermined

[2] We provide here the Y_e distribution in ejecta (defined as gravitationally unbound mass) beyond 1,000 km. We also looked at the Y_e mass distribution of ejecta beyond 100 km. Our conclusion that our 3D simulation has a narrower Y_e span than the 2D model, remains unchanged.

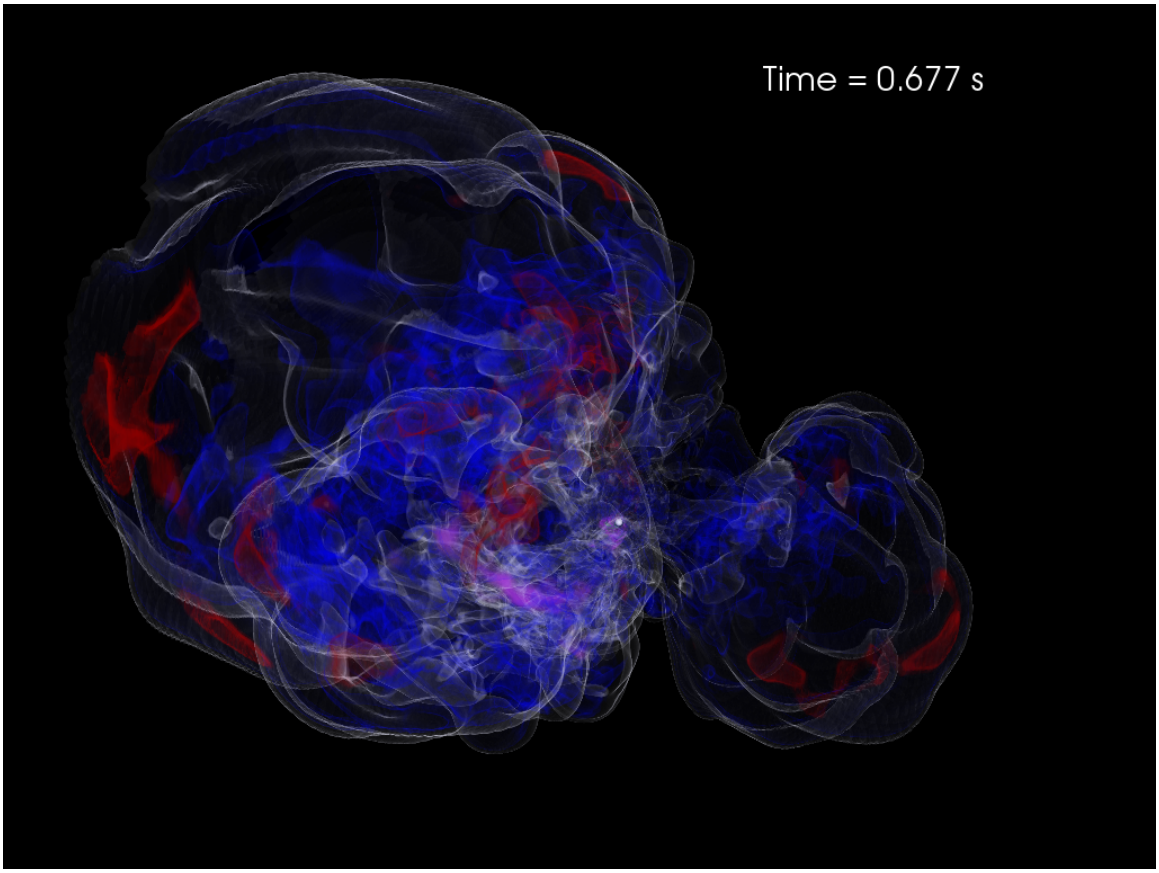

Figure 4.10: Y_e distribution at ∼677 ms after bounce. The white "veil" encompasses the expanding plumes, just interior to the shock radius, at a Y_e of 0.5. The blue plumes indicate a Y_e spanning the interval 0.5 - 0.52, and the red caps a Y_e greater than 0.52. The latter is concentrated along the exterior cusps of the plumes, and interior where accretion is funneled onto the PNS. Note the resemblance of the high-Y_e distribution to the entropy distribution in Fig. 4.1. The violet tail shows the low-Y_e (< 0.5) ejecta seen in Fig. 4.9. This trailing 'tail' is also visible in the density evolution of the progenitor.

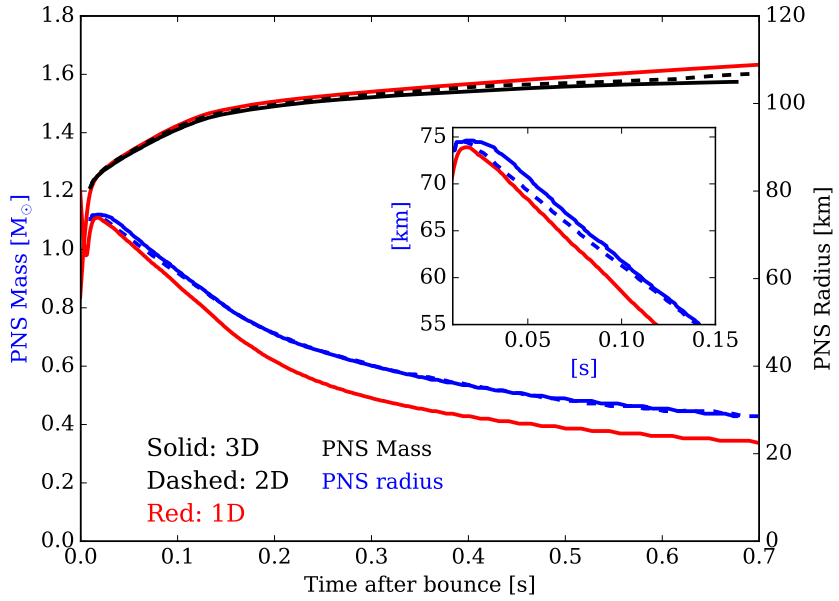

Figure 4.11: The PNS mass (in $M_\odot$, blue) and radius (in km, black) as a function of time after bounce (in seconds) for the 3D (solid), 2D (dashed), and 1D (red) simulations of the 16-$M_\odot$ progenitor. At late times, the PNS radii for the 2D and 3D simulations are virtually identical, but significantly smaller in the 1D case. The larger PNS mass in 1D than 2D, and in 2D than 3D, is due to the longer accretion history than in 3D, where we see early explosion. In the inset, we show the PNS radius zoomed in for the first 150 ms after bounce. Until ∼140 ms after bounce, the PNS radius in the 2D simulation is as much as ∼3% smaller than for the 3D simulation.

by the more rapid diffusion of energy vis à vis lepton number. Wilson captured this effect in 1D spherical models of explosion with a mixing-length-like diffusive flux, and the ν_e and $\bar{\nu}_e$ luminosities were thereby augmented by ∼25%. Without this effect, Wilson's models did not explode. However, Bruenn & Dineva (1996) showed that the core was not unstable to such "neutron-finger" convection, and this was confirmed by Dessart et al. (2006) using 2D simulations. However, after bounce, there is a region in the PNS between ∼10 and ∼30 kilometers that is in fact unstable to classical convection, driven mostly by negative Y_e gradients. This PNS convection is a feature in all modern multi-dimensional simulations of CCSN. In their study, Dessart et al. (2006) noticed that this overturning convection increased the emergent luminosities, but by the end of their simulation ∼200−300 ms after bounce this increase was not

large. In addition, inner PNS convection and the outer neutrino-driven convection interior to the stalled shock did not merge into one large convective zone. Given this, Dessart et al. (2006) concluded that PNS convection was not centrally important to the neutrino mechanism of CCSNe.

On the contrary, in their study of the lowest-mass progenitor stars, Radice et al. (2017) found that the contribution of a PNS convection boost to the emergent neutrino luminosities grew with time after bounce, and could reach significant fractions. This was particularly true for $\bar{\nu}_e$ and ν_μ neutrinos, for which the respective neutrinospheres are deepest. Here, we explore the corresponding effects and numbers for our 3D simulation of the 16-$M_\odot$ progenitor of Woosley & Heger (2007), and compare them to the 2D case.

We plot in Fig. 4.11 the PNS mass (in $M_\odot$, blue) and mean radius (black) as a function of time after bounce for the 3D (solid), 2D (dashed), and 1D (red) simulations of the 16-$M_\odot$ progenitor. The PNS surface here is defined where the density is 10^{11} g cm^{-3}. The baryonic PNS mass in our 3D simulation at $\sim$677 ms after bounce is $\sim$ 1.57 $M_\odot$ (1.6 $M_\odot$ in the 2D model, 1.63 $M_\odot$ in the 1D model), corresponding to a gravitational mass of 1.42 $M_\odot$ (1.44 $M_\odot$ in the 2D model, 1.47 $M_\odot$ in the 1D model). The PNS mass reflects the disruption of net accretion onto the PNS. Interestingly, we find that the difference between the PNS mass for the 1D and 2D models is roughly comparable to the difference in the same quantity between the 2D and the 3D models at late times, despite the absence of explosion in the 1D model and the correspondingly lengthier accretion history. Furthermore, at late times, the mean PNS radii in the 2D and 3D simulations are virtually identical ($\sim$29 km) but are significantly smaller in the 1D case ($\sim$23 km). A similar dependence of the PNS radii on simulation dimension was found in Radice et al. (2017) and Vartanyan et al. (2018b). Here, we have the opportunity to compare such quantities to that of a 3D simulation. In the inset, we show the PNS radius zoomed in for the first 150 ms

after bounce. Until ∼140 ms after bounce, the PNS radius in the 2D simulation is as much as ∼3% smaller than in the 3D model, lying between the PNS radii in the 3D simulation and in the 1D simulation. Simultaneously, as shown in Fig. 4.8, the "heavy"-neutrino luminosity is slightly smaller in the 2D simulation than in the 3D simulation. At later times, both the "heavy"-neutrino luminosity and the PNS radius in the 1D simulation are significantly lower than in the multidimensional simulations (see also Radice et al. 2018; Vartanyan et al. 2018b). On time scales greater than ∼200 ms, PNS convection boosts the "heavy"-neutrino luminosities in the 2D and 3D simulations. Furthermore, the shrinking PNS radius comes into close contact with the inner convective region after 200 ms (see Fig. 4.12), explaining the larger PNS radii in multi-dimensional simulations. However, electron-type neutrino luminosities are higher in 1D than in multidimensional simulations simply because that model does not explode, and accretion power remains significant.

In Fig. 4.12, we provide a space-time diagram of the standard deviation over angle of the radial velocity within the inner 100 km through 300 ms after bounce for the 3D (left) and 2D (right) models. Both convective regions are visible here as the bright regions − the interior convective band is similar to that seen in Dessart et al. (2006), and the exterior, neutrino-driven convection recedes to ∼50 km by ∼300 ms. The interior convective zone in the 2D simulation is a few kilometers wider and has higher convective velocities than its 3D counterpart. Furthermore, we see more variation in the radial location of the convective zones in the 2D simulation. However, in the 3D simulation, the exterior, neutrino-driven convective region is located deeper in at early times, reaching ∼80 km by ∼50 ms after bounce in the 3D simulation (by comparison, the exterior convective region in the 2D case reaches 80 km more than 100 ms after bounce). Through the first ∼150 ms, this exterior convection reaches down into the PNS region in the 3D (but not the 2D) simulation. This may explain the slightly increased neutrino luminosities and shock radii in the 3D simulation seen

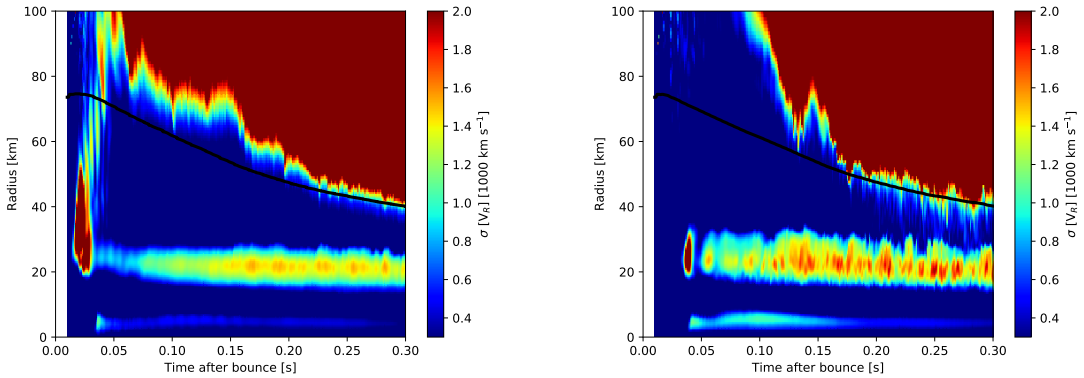

Figure 4.12: A space-time diagram of the standard deviation $\left(\sqrt{\langle(v_r - \langle v_r\rangle)^2\rangle}\right)$ over angle of the radial velocity within the inner 100 km through 300 ms after bounce for the 3D (left) and 2D (right) models. Note that it is significantly smaller in 3D than in 2D (see also Fig. 4.13). Both the outer and inner (PNS) convective regions are visible here, and the interior convective zone is a band in velocity similar to that seen in Dessart et al. (2006). The black lines illustrate the mean PNS radius, which in 3D, and not 2D, is sampled by the outer neutrino-driven convection through the first 120 ms after-bounce. By ∼300 ms after bounce, the exterior convective zone has receded to ∼50 km. In the 2D simulation, the interior convective zone is a few km wider and has higher convective velocities by several hundred km s^{-1} than its 3D counterpart. Furthermore, we see more variation in the radial location of the convective zones in the 2D simulation, with the outer convective zone making excursions almost to the inner convective zone by ∼300 ms after bounce. See the text for further discussion.

in Fig. 4.8 and Fig. 4.11 at these earlier times. Lastly, we see a turbulent "teardrop" in the 3D simulation extending from ∼20 to ∼80 km in the first ∼40 ms after bounce, trailing off to both the inner and outer convective regions by ∼60 ms after bounce. By comparison, this feature is much smaller in extent and delayed to ∼40 ms after bounce in the 2D model. The PNS convective zone has a characteristic size of ∼10 km, a turnover time of ≤10 ms, and convective velocities of ∼1000 km s^{-1}. This is a manifestation of the stronger turbulence within 100 km at early times in the 3D simulation.

We explore the convective differences in the 2D and 3D simulations in Fig. 4.13. We show velocity vectors (white) on a Y_e colormap depicted on an x-y slice of the 3D simulation (left) and an x-z slice of the 2D simulation (right) at ∼57 (top), ∼304

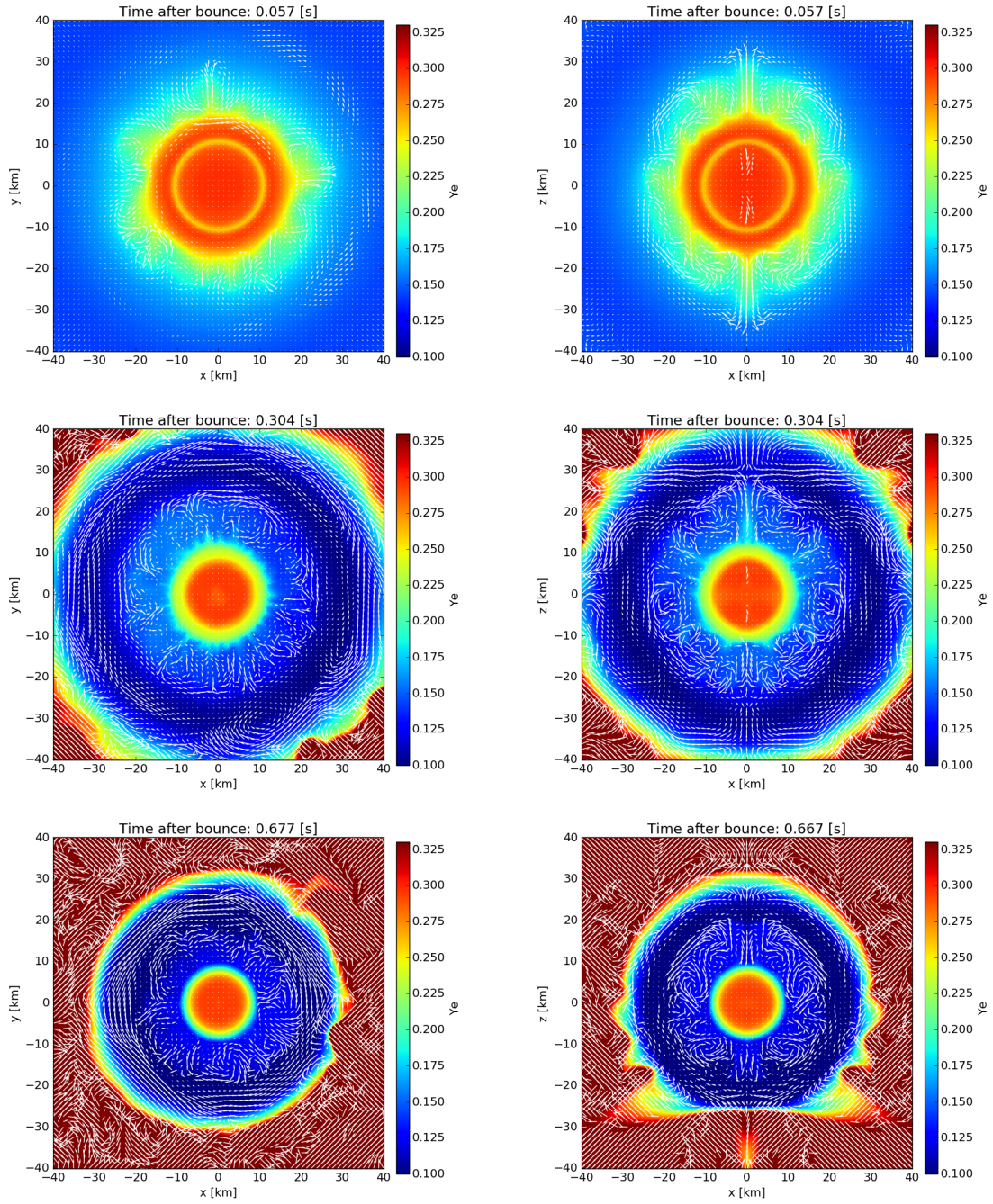

Figure 4.13: Velocity vectors (white) on a Y_e colormap depicted on an x-y slice of the 3D simulation (**left**) and an x-z slice of the 2D simulation (**right**) at ∼57 (**top**), ∼304 (**middle**), and ∼667 (**bottom**) ms after bounce to illustrate the evolution of inner-PNS convection. The velocity vector lengths are scaled to velocity and saturate at 2000 km s^{-1}. Note the characteristic convective whorls forming within the first ∼60 ms after bounce. The region of inner convection (with Y_e ∼0.15-0.2) shrinks with the PNS, and at later times the exterior, neutrino-driven convective region (with Y_e $\gtrapprox$0.3) is visible beyond ∼30 km, with low-Y_e "flares" traversing the boundary.

(middle), and ∼667 (bottom) ms after bounce to illustrate the evolution of inner PNS convection. The vectors lengths are scaled to velocity and made to saturate at 2000 km s^{-1}. Note the characteristic convective whorls forming within the first ∼60 ms after bounce.

4.3.6 On the Possible Presence of the LESA and the SASI

The lepton-number emission self-sustained asymmetry (LESA) was proposed in Tamborra et al. (2014a) as a neutrino-hydrodynamical instability resulting in $\nu_e - \bar{\nu}_e$ asymmetry. In an earlier work (Vartanyan et al. 2018b, Ch. 3), we explored the possibility of LESA by examining the dipole harmonic component, a_{10}, of the net lepton number flux. There, we concluded that, at least in 2D, the effect was negligible and speculated that the inference of LESA may be a consequence of the use of the ray-by-ray approximation to multi-dimensional neutrino transport.

We now extend our exploration of the possible presence of the LESA, using for the first time an exploding 3D model with full physical realism. In Fig. 4.14, left panel, we depict the monopole and dipole components of the lepton asymmetry ($F_{\nu_e} - F_{\bar{\nu}_e}$) as a function of time after bounce at 500 km for both our 3D and 2D simulations. Here, we follow O'Connor & Couch (2018a) and plot instead the dipole magnitude,

$$A_{\rm dipole} = 3 \times \sqrt{\sum_{i=-1}^{1} a_{1i}^2}, , \tag{4.6}$$

using the normalization scheme of Burrows et al. (2012). The net effect is to increase the strength of the dipole term relative to the monopole term by a factor of ∼1.73 ($3/\sqrt{3}$). We conclude that we do indeed find a LESA (see also O'Connor & Couch 2018a) effect, and that (at least for these models) it is stronger in 3D than in 2D. However, the magnitude of the fluctuations in the lepton asymmetry is larger in 2D than in 3D. In addition, whereas Tamborra et al. (2014a) find that the dipole term

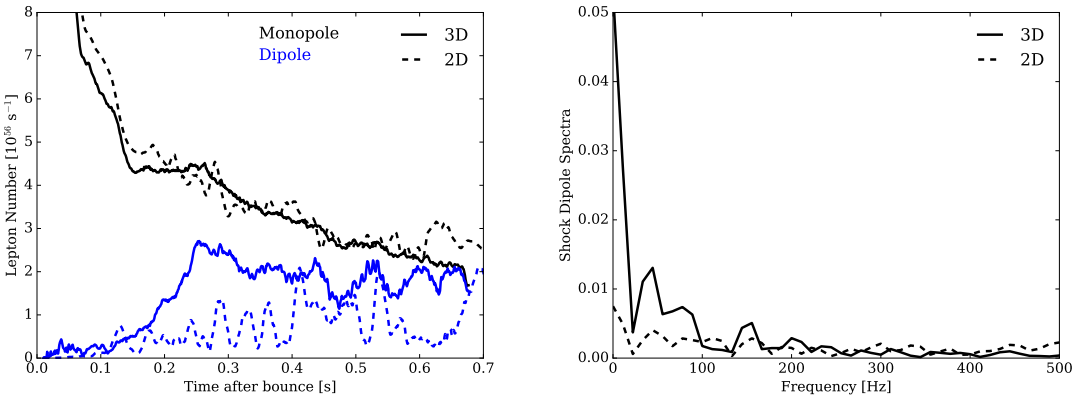

Figure 4.14: **Left**: We plot the monopole (black) and dipole (blue) of net lepton number asymmetry $F_{\nu_e} - F_{\bar{\nu}_e}$ (in units of 10^{56} s^{-1}) as a function of time after bounce (in seconds) at 500 km to explore the possible appearance of the "LESA" phenomenon. Solid indicates the 3D model and dashed the 2D model. We do see the LESA effect, and the dipole term in the 3D simulation is larger and less variable than in the corresponding 2D model. However, the dipole term becomes comparable in magnitude to the monopole term only after ∼650 ms. **Right**: We plot the Fourier decomposition of the shock radius dipole component as a function of frequency (in Hz) for the first 100 ms after bounce for the 3D (dashed) and 2D (solid) simulations. Note that while the dipole component is insignificant for both models early on, it is larger for the 3D model during the first ∼100 ms. This is also as seen in Fig. 4.4 (solid red line, right panel).

overtakes the monopole term as early as ∼200 ms after bounce, we find that only after ∼650 ms after bounce does the dipole component of the LESA become comparable to the monopole term. We continue to suggest that the ray-by-ray approach leads to a larger LESA, but this remains to be tested with a comparison of 3D ray-by-ray and multi-angle simulations.

We have also studied our 3D simulation for the possible presence of the standing accretion shock instability (SASI) (Blondin et al. 2003) during any phase of its evolution. If present, this should manifest in a narrow and obvious frequency peak in various power spectra. Recent work in 3D (Walk et al. 2018) found pronounced peaks in the electron anti-neutrino power spectrum at ∼60 and ∼110 Hz that the authors associated with the SASI. In addition, Kuroda et al. 2017 and Kuroda et al. 2016a suggested that softer equations of state manifest the SASI, with its gravita-

tional wave signature lasting for an interval of ∼100 ms (a fraction of their simulation time) at frequencies of ∼50-200 Hz. Figure 4.14, right panel, portrays the Fourier decomposition of the dipole moment of the shock radius in both our 3D simulation and the associated 2D simulation out to 200 ms after bounce. We find no clear peak at these frequencies, either by this metric or in the gravitational wave emissions (not shown here). Moreover, a glance at Fig. 4.4 reiterates that we see in the 3D run no significant dipole term in the shock radius until after explosion. [3] Therefore, we conclude that we have no evidence for the SASI in our 16-$M_\odot$ simulations. However, since we find an early explosion in both the 3D and 2D simulations, perhaps the SASI may have had insufficient time to develop. It is important to note, however, that O'Connor & Couch (2018a) likewise did not see a SASI for their 3D simulation (which was carried out to ∼600 ms after bounce, and did not explode) of a 20-$M_\odot$ progenitor when incorporating velocity dependence. Note that the small bump at ∼40 Hz in Fig. 4.4 corresponds to small-amplitude oscillations of the shock dipole in the first ∼100 ms after bounce. This feature is easily associated with the characteristic large-scale advective and convective time scales in the region between the shock and the PNS.

We summarize here some of the catalysts to explosion in 3D. The 16-$M_\odot$ progenitor model (Woosley & Heger 2007) upon which we focus in this Chapter has a steep density dropoff interior to 1.7-$M_\odot$ due to its Si/O interface. Such a sharp density drop has been shown to faciliate explosion in models incorporating turbulence (be they 2D or 3D) (Vartanyan et al. 2018b) and we witnessed the explosion of this model in our previous 2D study. In addition, our inclusion of the many-body effect on the neutrino-nucleon scattering cross sections (Burrows et al. 2018) and the introduction of the significant velocity perturbations to the progenitor are both conducive to explosion.

[3] However, the dipole term is slighter stronger in the first ∼100 ms for the 3D simulation than for its 2D counterpart.

These aspects, in addition to the effects of GR and heating due to inelastic neutrino-electron and neutrino-nucleon scattering, seem to be some of the agents of "success."

4.4 Conclusions

We have presented one of the first non-rotating, state-of-the-art, full-microphysics simulations in three spatial dimensions to explode as a supernova. The explosion of a 16-$M_\odot$ progenitor is fully underway by $\sim$200 ms after bounce and at the end of the simulation is accumulating energy at a rate that if continued would reach $\sim$0.5 Bethes (0.5×10^{51} erg) within two seconds. However, what its final asymptotic energy will be remains to be seen. The gravitational mass of the remaining neutron star is $\sim$1.42 $M_\odot$. The morphology of the emerging debris field has a roughly dipolar structure, with two asymmetric wide-angle lobes (one large, one small), whose axis emerged randomly. Whether slight rotation would impose an axis for the ejecta, or what rotation rate would be necessary to bias the emergent explosion axis, is not here determined. By the end of the simulation, an exploding debris field is accompanied by simultaneous inward accretion between the expanding lobes of some of the inner-progenitor matter, partly responsible for maintaining a driving neutrino luminosity (Burrows et al. 2007c). Interestingly, the majority of the ejecta of this supernova are proton-rich, with Y_e between 0.5 and 0.56. This will have interesting consequences for the associated nucleosynthesis, with the potential to explain in part the first r-process peak and p-process yields (Hoffman et al. 1996; Pruet et al. 2006; Fröhlich et al. 2006; Wanajo et al. 2011; Frebel 2018; Bliss et al. 2018).

It has been shown in the past that vigorous turbulent convection behind the temporarily stalled shock is essential to ignite an explosion for almost all anticipated progenitor structures. Only the rare progenitors at the lowest ZAMS masses with very steep density profiles exterior to the collapsing Chandrasekhar core explode in

spherical symmetry (Kitaura et al. 2006; Burrows et al. 2007a; Radice et al. 2018). The turbulent motions, boasting as they do a large effective 'γ' connecting kinetic energy with pressure/stress, are one agency. Another is the consequently larger gain region in the multi-D turbulent context. A third could be the longer dwell times in the gain region occasioned by the non-radial motions (Murphy & Burrows 2008). Aside from the necessity in most cases of the turbulence enabled in the multi-D context, the specific progenitor density profile is a major determinant, though the dependence upon the associated "compactness" parameter (O'Connor & Ott 2013) of the "explodability" of a model is non-monotonic in subtle ways (Burrows et al. 2018). Models with the lowest compactness may explode even in 1D via a wind mechanism (Burrows 1987). However, models with slightly higher compactness have trouble exploding (Burrows et al. 2018; O'Connor et al. 2017), while models with even higher compactness (such as the 16-$M_\odot$ of this Chapter) explode rather easily. Clearly, the explodability's dependence upon progenitor density profile is not straightforward.

One aspect of this nuanced behavior is the role of the accretion through the shock of the silicon-oxygen interface (see Vartanyan et al. 2018b; Summa et al. 2018). The jump up in entropy at that interface is accompanied by a corresponding drop in mass density. If that drop is large and sharp, then when that interface is accreted through the stalled shock the confining ram pressure temporarily and abruptly declines, while not immediately altering the driving neutrino luminosities (emanating from the core) and heating rates. The consequence is often (as in the case studied here) a kick into explosion, which in the immediate term is generally irreversible due to the quick diminution of neutrino cooling occasioned by expansion and the maintenance of heating. However, the magnitude and radius of this interface and the overall density profile of the core at collapse are functions of stellar evolution (and stellar progenitor models), emphasizing the centrality to the viability and character of core-collapse supernova explosion phenomenology of these initial states.

Another progenitor determinant of explosion may be its initial seed perturbations. It has been shown (Couch & Ott 2013, 2015; Müller & Janka 2015; Müller 2016; Burrows et al. 2018) that if the seeds are of sufficient strength, then the ability of turbulence to ignite explosion is enhanced. In the simulation highlighted here, we imposed a modest physical perturbation to the accreted velocity field that may have helped or accelerated explosion. However, whether perturbations are important, or merely facilitators, has not been determined and the next generation of fully-3D progenitor models may illuminate this question (Couch et al. 2015; Müller et al. 2016b).

Those realistic physical processes that were conducive to the 3D explosion we witnessed in this Chapter include neutrino-driven turbulence (Burrows et al. 1995; Herant et al. 1994), the net effects of general relativity (Bruenn et al. 2001), the inclusion of inelastic scattering and energy redistribution via neutrino-electron and neutrino-nucleon scattering (Burrows et al. 2018; Vartanyan et al. 2018b; Just et al. 2018), the many-body correction to neutrino-nucleon scattering (Burrows & Sawyer 1998; Horowitz et al. 2017; Burrows et al. 2018), the accretion of a sharp silicon-oxygen interface at a propitious time (Vartanyan et al. 2018b), and the imposition of velocity perturbations in the progenitor. A major consequence of the many-body correction is the decrease in the scattering rate that increases the neutrino emission rates. This is particularly true for the ν_μs, and the resulting acceleration of core contraction leads to, among other things, the increase in the temperatures around the ν_e and $\bar{\nu}_e$ neutrinospheres. This leads to a slight hardening of the emergent ν_e and $\bar{\nu}_e$ spectra and an increase in the heating rate due to charged-current absorption on the free nucleons in the gain region. One of the most important future classes of investigations of direct relevance to the CCSN mechanism is the magnitude and role of many-body corrections to both the neutral-current and the charged-current (Burrows & Sawyer 1999; Roberts et al. 2012; Roberts & Reddy 2017) neutrino-matter

interaction rates. We note as well that even though the number of viable published nuclear equations of state is dwindling, the EOS dependence of the outcome of collapse has not been definitively addressed, nor well explained. This will be a necessity in the years to come as laboratory constraints become ever more stringent.

While the results presented here are quite encouraging, there remain a number of important caveats. Important among these are the dependence upon the spatial and energy-group resolutions. In 3D, a resolution study, even with modern codes such as FORNAX, is expensive, but will be necessary to determine both the quantitative and qualitative limitations of what we have presented here. The chaotic character of turbulent flow will make this a challenging endeavor for the community going forward. Moreover, we have conducted these calculations including the effects of general relativity in approximate fashion. Doing these calculations with full GR will be important and attempts in this direction have already been made (Roberts et al. 2016; Ott et al. 2018; Kuroda et al. 2018). To enable these forefront simulations, we still had to make approximations in the neutrino sector. Foremost among these is the use of the moment formalism and an analytic closure for the second and third moments. While recent tests of the accuracy of such an approach in the core-collapse context are encouraging (Richers et al. 2017; O'Connor et al. 2018), solving the full Boltzmann equation with neutrino angles in the full six-dimensional phase space will require a significantly more capable national and international computational infrastructure. Finally, it has been shown that explodability when near criticality and in multi-D is a sensitive function of details in the neutrino-matter interaction rates (Burrows et al. 2018) in a way not seen in 1D simulations. This puts a premium on implementing correctly the correct microphysics. All modelers aspire to this goal, but whether we or others actually have achieved this is, or should be, a constant worry.

The model we presented was non-rotating. We think that most collapsing cores, while they are certainly rotating, are not generically rotating at rates sufficient to make a qualitative difference most of the time (Emmering & Chevalier 1989; Faucher-Giguère & Kaspi 2006; Popov & Turolla 2012; Noutsos et al. 2013). However, this remains to be exhaustively explored. Rapid rotation can certainly effect the outcome, both directly and by providing significant free energy to feed large magnetic fields and enable the direct effects of magnetic stress, when strong, on the explosion dynamics (see, e.g., Burrows et al. 2007b; Mösta et al. 2015). In fact, rapid rotation alone can affect the dynamics and facilitate explosion even when the expected magnetic field amplifications are ignored (Fryer & Warren 2002, 2004; Marek & Janka 2009; Summa et al. 2018). Moreover, rapid rotation can also generate a non-axisymmetric spiral-arm mode, which resembles the SASI in the rotating context and might enlarge the gain region and, thereby, facilitate explosion (Takiwaki et al. 2016; Summa et al. 2018). Curiously, if the explosion is suitably delayed, such a mode may also grow in the non-rotating context (Blondin & Shaw 2007; Rantsiou et al. 2011; Guilet & Fernández 2014; O'Connor & Couch 2018a). This and other related issues are fruitful topics for future work.

However, we view the achievement of a 3D simulation that leads naturally to explosion, with competitive resolution, including all the relevant microphysics, using a state-of-the art simulation tool, and calculating significantly post-bounce as a major milestone in the decades-long quest to resolve the core-collapse supernova puzzle in quantitative detail. What remains in the near term is to determine the progenitor mass dependence of the outcome of collapse in 3D, to understand the possible roles of rotation, to explain the supernova energies and neutron star masses observed, and to explain the morphologies of the debris fields seen in supernova remnants. Furthermore, a major motivation of all supernova simulations is the detailed explanation of the explosive production of the elements. The ejecta we find are mostly proton-rich,

and this emerges naturally from the detailed simulations. What the consequences are of this finding will be one of the topics of our future studies as we continue our quest to understand one of the most persistent problems in stellar and nuclear astrophysics.

Chapter 5

Observations

5.1 Introduction

Recent supernova code developments (e.g., Skinner et al. 2019) running on a new generation of supercomputers have ushered in an era of unparalleled 3D simulations of core-collapse supernovae (CCSNe). For instance, our group is now able to produce over ten three-dimensional supernovae simulations in under a year, rivaling even the most comprehensive efforts in two-dimensions just a few years ago. With such a sample size, one can begin to perform preliminary statistics of explosion characteristics and outcomes.

The advent of such computational capability has been paralleled by novel astronomical detector capabilities. Recent discoveries of gravitational waves from astrophysical sources (Abbott et al. 2016b) and existing and upcoming neutrino detectors (SuperKamiokande (Abe et al. 2016), HyperKamiokande (Abe et al. 2011; Hyper-Kamiokande Proto-Collaboration et al. 2018), DUNE (Migenda 2018; Ankowski et al. 2016), JUNO (Lu et al. 2015), IceCube (Abbasi et al. 2011; Köpke & IceCube Collaboration 2011) motivate new efforts to scrutizine direct signatures of proto-neutron star formation and supernova explosion. Neutrino detection of a galactic supernova

will provide insight into both the dynamics of explosion and the physics of matter at nuclear densities (Müller 2019). In addition, Suwa et al. (2019) emphasize that, depending upon the neutron star mass, galactic supernova neutrinos can be observed for 30−100 seconds. Simultaneous observation of gravitational waves (GWs) will constrain PNS convection and g/f-mode oscillation (Morozova et al. 2018b; Hayama et al. 2018; Radice et al. 2019) as well as neutrino-driven convection and possibly the standing accretion shock instability (SASI) (Tamborra et al. 2013, 2014b; Kuroda et al. 2017; Walk et al. 2019). CCSN gravitational waves are detectable for galactic events via the LIGO/Virgo network, and even further with future third-generation detectors (Srivastava et al. 2019; Powell & Müller 2019).

Many groups are now capable of high-fidelity 3D simulations (Vartanyan et al. 2019b; Radice et al. 2019; Burrows et al. 2019; Nagakura et al. 2019a; O'Connor & Couch 2018a; Müller et al. 2017; Summa et al. 2018; Glas et al. 2019; Takiwaki et al. 2016; Yoshida et al. 2019; Nagakura et al. 2019c; Roberts et al. 2016; Ott et al. 2018). Our code Fornax is unique in its inclusion of detailed microphysics (including inelastic scattering), fast explicit transport with an implicit local solver (without the ray-by-ray approximation and with velocity dependence), respectable angular and radial resolution (Nagakura et al. 2019a), and static mesh refinement to obviate severe Courant limitations in the core and on the axis. The result is a code sporting the necessary realism that is five−ten times faster than previous 3D codes.

Using results from Fornax, we present in this Chapter the first study of variability and correlation to include a sample of almost a dozen state-of-the-art core-collapse supernovae simulations done with sophisticated neutrino physics and transport. The objective of this Chapter is to correlate CCSNe observables with physical quantities in the core to provide a basis for using neutrino and gravitational measurements to constrain the physical phenomena in the opaque CCSNe core. Earlier such work on correlations (Totani et al. 1998; Raffelt 2005; Brandt et al. 2011; Tamborra et al.

2013; Nakamura et al. 2016; Wallace et al. 2016; Kuroda et al. 2016a, 2017; Seadrow et al. 2018; Hayama et al. 2018; Walk et al. 2019) focused on far fewer models with either a sub-optimal suite of included physics or at lower dimensionality. We study the neutrino and gravitational wave signatures and temporal and spatial variations, as well as correlations with the CCSN progenitor, for a comprehensive suite of 11 progenitors spanning 9−60 $M_\odot$ evolved in 3D. These models, or a subset, were explored in three earlier works: Vartanyan et al. (2019b), where we investigated the explosion of a 16-$M_\odot$ in 3D; Burrows et al. (2019), where we studied the evolution of the 9-13-$M_\odot$ progenitors from this suite; in Radice et al. (2019), where we analyzed the gravitational wave signal of progenitors in this suite, and in Nagakura et al. (2019a), where we looked at the dependence of angular resolution on explosion outcome for the 19-$M_\odot$ progenitor. We save for an upcoming paper a broader study of the explosion characteristics and phenomenology of this large 3D model suite (Burrows et. al, in prep.).

We organize the Chapter as follows: In §5.2, we outline the physical and numerical setup of our simulation. In §5.3, we explore the temporal and spatial variations of neutrinos. We investigate the time series of neutrino emissions accessible to future neutrino detectors, and identify the associated physical processes driving the time variability. In §5.4, we repeat the process for gravitational waves. In §5.5, we comment on where and when the SASI might emerge. In §5.6, we explore the possible presence of the LESA (Tamborra et al., 2014a) in our 3D simulations. In §5.7, we look at correlations between observable gravitational and neutrino signals and the physics of CCSNe, such as neutron star convection, shock radius growth, and accretion rate. In §5.8, we conclude with summary comments and conclusions.

5.2 Numerical Setup

FORNAX is a multi-dimensional, multi-group radiation hydrodynamics code originally constructed to study core-collapse supernovae. Its design, capabilities, and a variety of core tests are detailed in Skinner et al. (2019). In 2D and 3D, FORNAX employs a dendritic grid which deresolves in angle at small radii to avoid restrictive CFL timestep limitations, while at the same time preserving cell size and aspect ratios. Our method of deresolving near the polar axis for 3D simulations allows us partially to overcome axial artifacts seen conventionally in 3D simulations in spherical coordinates (Lentz et al. 2015; Müller et al. 2017). FORNAX solves the comoving-frame velocity-dependent transport equations to order O(v/c). The hydrodynamics uses a directionally-unsplit Godunov-type finite-volume scheme and computes fluxes at cell interfaces using an HLLC Riemann solver. For all the 3D simulation highlighted here, we employ a spherical grid in r, θ, and ϕ of resolution 678×128×256 (608×128×256 for the 16-$M_\odot$ model). The radial grid extends out to 20,000 kilometers (10,000 for the 16-$M_\odot$ model) and is spaced evenly with $\Delta r \sim 0.5$ km for radii interior to 20 km and logarithmically for radii exterior to 50 km, with a smooth transition in between. The angular grid resolution varies smoothly from $\Delta\theta \sim 1.9°$ at the poles to $\Delta\theta \sim 1.3°$ at the equator, and has $\Delta\phi \sim 1.4°$ uniformly. For this project, following Marek et al. (2006) we used a monopole approximation for relativistic gravity and employed the SFHo equation of state (Steiner et al. 2013), which is consistent with all currently known nuclear constraints (Tews et al. 2017).

We solve for radiation transfer using the M1 closure scheme for the second and third moments of the radiation fields (Vaytet et al. 2011) and follow three species of neutrinos: electron-type (ν_e), anti-electron-type ($\bar{\nu}_e$), and "ν_μ"-type (ν_μ, $\bar{\nu}_\mu$, ν_τ, and $\bar{\nu}_\tau$ neutrino species collectively). We use 12 energy groups spaced logarithmically between 1 and 300 MeV for the electron neutrinos and to 100 MeV for the anti-electron- and "ν_μ"-neutrinos.

We study 11 progenitors in 3D, covering 9-, 10-, 11-, 12-, 13-, 14-, 15-, 16-, 19-, 25-, and 60-$M_\odot$ models. All models are initially collapsed in 1D through 10 ms after bounce, and then mapped to three dimensions. For all progenitors except the 16- and 25-$M_\odot$ models, we use Sukhbold et al. (2016). We use Woosley & Heger (2007) for the 16-$M_\odot$ progenitor, the same studied in Vartanyan et al. (2019b). For the 25-$M_\odot$ progenitor, we use Sukhbold et al. (2018). After mapping to 3D, we impose velocity perturbations following Müller & Janka (2015) within $200 - 1000$ km with a maximum speed of 100 km s^{-1} and harmonic quantum numbers of $l = 10$, $m = 1$, and $n = 4$ (radial), as defined in Müller & Janka (2015), for all models except the 16-$M_\odot$ progenitor, which is perturbed in three spatially distinct regions ($50 - 85$ km, $90 - 250$ km, and $260 - 500$ km), with a maximum speed of 500 km s^{-1} and harmonic quantum numbers of $l = 2$, $m = 1$, and $n = 5$ (radial). The details of the imposed perturbations are unlikely to make any qualitative difference in our conclusions.

In the left panel of Fig. 5.1, we plot the density profiles as a function of mass for the progenitors studied here. We highlight the accretion of the silicon-oxygen (Si/O) interface, often corresponding to a drop by several in density, with a colored diamond. Density profiles historically have been parametrized by compactness (O'Connor & Ott 2013), defined at a given mass (typically 1.75 $M_\odot$) and radius. However, we note the wide diversity of locations for the Si/O interfaces in this progenitor suite, from interior masses of 1.3 to 1.9 $M_\odot$. Accretion of this interface often coincides with explosion time, and its presence and significance would require a multi-dimensional parametrization of progenitor profiles.

In the right panel of Fig. 5.1, we illustrate the evolution of the mean shock radii for all our 3D models. All progenitors except for the 13-, 14-, and 15- $M_\odot$ models explode, where we see an island of non-explosion (Burrows et al. 2019) and a weaker Si/O interface. Previously, the 15-$M_\odot$ has either failed to explode in 2D simulations (Vartanyan et al. 2018b; O'Connor & Couch 2018b) or has exploded late (Summa

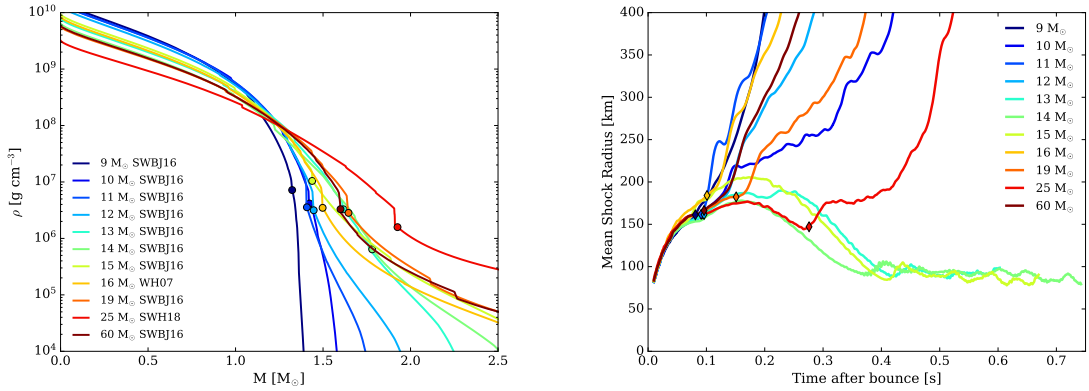

Figure 5.1: **Left**: Mass density profile (in g cm^{-3}) with interior mass (in $M_\odot$) for the 11 progenitors of this study from three different model sets, studied in this series. The labels SWBJ16, WH07, and SWH18 stand for the progenitor models of Sukhbold et al. (2016), Woosley & Heger (2007), and Sukhbold et al. (2018), respectively. The location of the sharp density drop at the silicon-oxygen interface, whose accretion often inaugurates explosion, is marked as a circle for each progenitor. **Right**: Mean shock radius (in km) as a function of time after bounce (in seconds) for the progenitors studied here. The diamonds indicate the approximate onset of explosion; all models except the 13-, 14-, and 15-$M_\odot$ progenitors explode. The 25-$M_\odot$ progenitor explodes latest, at ∼275 ms postbounce. Explosion time here corresponds closely with the accretion of the Si/O interface.

et al. 2016). We emphasize that the 13-, 14-, and 15-$M_\odot$ progenitors are definitely less explodable. However, those of our models that do not explode may do so with different physics or initial structure, such as an initially rotating progenitor, or at higher resolution (Nagakura et al. 2019a).

For specificity, we define explosion time as when the mean shock radius surpasses 150 km and undergoes an inflection point. Explosion sets in primarily between 100−200 ms after bounce except for the the 25-$M_\odot$ progenitor, which explodes near 275 ms after bounce, due to delayed accretion of the Si/O interface that is initially located further out. This model is unique in that we see shock revival at ∼275 ms, then a period of slow growth until ∼400 ms, after which the mean shock radius accelerates outwards. The explosion times we witness roughly correspond with the times of accretion of the Si/O interfaces (seen in Fig. 5.1), with a deeper steep Si/O interface predicting an earlier explosion time (Fryer 1999; Murphy & Burrows 2008). More

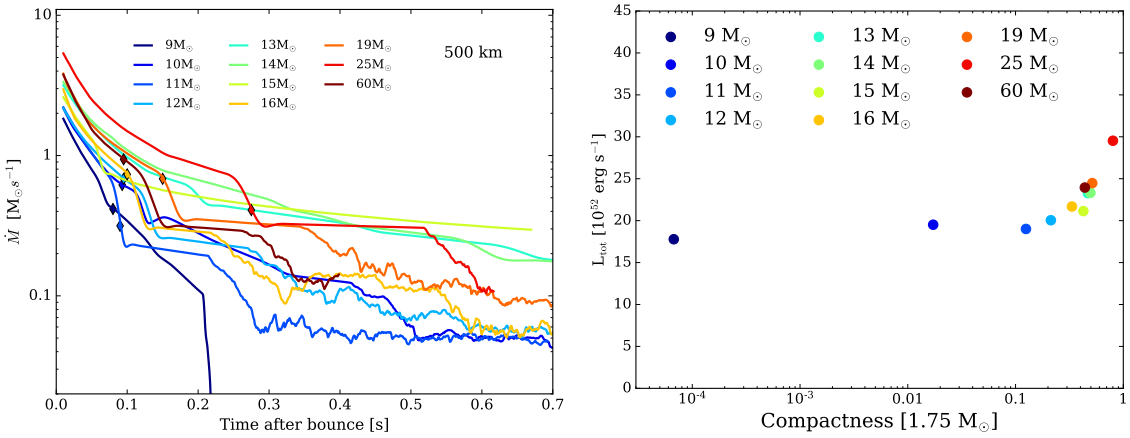

Figure 5.2: **Left**: The accretion rate ($M_\odot$ s^{-1}) at 500 km as a function of time after bounce (in seconds). The accretion rate increases in general with core compactness. The drop in the accretion rate corresponds to the sharp density drop at the infalling Si/O layer. The times of explosion are marked as diamonds. Note the steep drop in accretion rate for the 9-$M_\odot$ progenitor just after 200 ms. **Right**: Total neutrino luminosity (in 10^{52} erg s^{-1}) summed over all species measured at the post-breakout bump (see Fig. 5.3), between $70 - 100$ ms, for the various progenitors as a function of the compactness at 1.75 $M_\odot$. We note the linear trend towards higher peak luminosity with increasing compactness. The non-exploding models (13-, 14-, 15-$M_\odot$) lie slightly below the trend, indicating a lower luminosity for a given compactness. Compactness is just one measure of profile shallowness, which is a multi-dimensional quantity for which fits do not yet exist. We observe explosions for models with higher and lower compactness than the non-exploding 13-, 14-, 15-$M_\odot$ progenitors, and emphasize that compactness is not a criterion of explodability.

recent simulations have identified the importance of accretion of the Si/O interface in prompting earlier explosion in both 2D (Radice et al. 2017; Suwa et al. 2016; Vartanyan et al. 2018b) and 3D simulations (Hanke et al. 2013; Ott et al. 2018; Summa et al. 2018; Vartanyan et al. 2019b; Burrows et al. 2019).

5.3 Temporal and Directional Variation of Neutrino Emission

We now explore the neutrino emission in time and angle. In Fig. 5.2, left panel, we plot the accretion rates at 500 km as a function of time after bounce out to

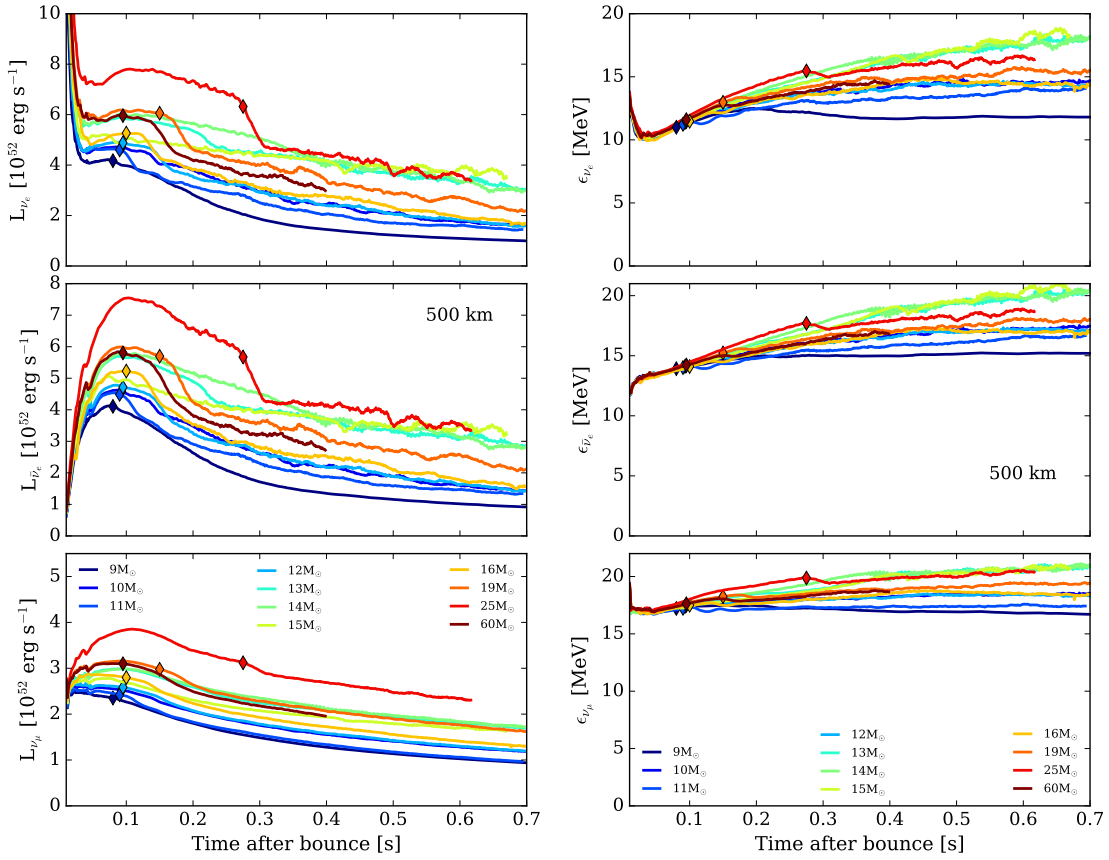

Figure 5.3: **Left**: Mean electron neutrino (top), electron anti-neutrino (middle), and the bundled heavy-neutrino (bottom) luminosities (in 10^{52} erg s^{-1}) as a function of time after bounce (in seconds). The accretion of the Si/O interface by the shock and ensuing explosion (diamonds) correspond to a sharp drop in the electron neutrino and anti-neutrino luminosities, with a more subdued drop in the heavy-neutrino luminosities. We note that the luminosity increases roughly with increasing progenitor mass (the 60-M$_\odot$ is an outlier) and closely with core compactness (see Fig. 5.2.) **Right**: Electron neutrino (top), electron anti-neutrino (middle), and the bundled heavy-neutrino (bottom) mean energies in MeV as a function of time after bounce (in seconds). The explosion time is marked in diamonds. The early turnover in the exploding models in neutrino energy corresponds to the accretion of the Si/O interface. Note that the non-exploding models have higher mean energies after ∼300 ms as a result of sustained accretion. The mean energies flatten out at late times.

700 ms for our suite of 3D models. In Fig. 5.3, we plot the solid-angle-averaged neutrino luminosities and mean energies, respectively, at 500 km as a function of time after bounce for all eleven models. The ν_μ, ν_τ neutrinos and anti-neutrinos are bundled into "heavy"-neutrinos in the plots. The heavy neutrinos have slightly higher mean energies ($\sim$5%) than the electron anti- neutrinos, which in turn have slightly higher neutrino energies ($\sim$15%) than the electron-neutrinos. The average neutrino luminosities are not in equipartition between species, nor do they exhibit a strict hierarchy by species. Furthermore, the summed electron-neutrino and anti-electron-neutrino luminosity is roughly equal to the total heavy-neutrino luminosity. (Raffelt 2005; Totani et al. 1998).

The models that fail to explode have a longer sustained accretion history and yield at late times, after $\sim$300 ms, higher accretion rates, mean neutrino energies, and neutrino luminosities, with observable consequences for neutrino detectors (Seadrow et al. 2018). The neutrino luminosities and mean energies flatten out at late times with the cessation of accretion. We note that the 9-$M_\odot$ progenitor − carried out to more than one second postbounce − is an outlier, with the accretion rate plummeting at $\sim$225 ms. The 60-$M_\odot$ progenitor loses most of its mass to winds early on, and behaves effectively like a lower mass progenitor. As will be discussed later, the low-mass 9-$M_\odot$ progenitor explodes more spherically (Burrows et al. 2019) than the more massive models studied, and for all intents and purposes, the 9-$M_\odot$ progenitor evolution is complete. We see a weak correlation between progenitor mass, accretion rates, and neutrino luminosities. The 25-$M_\odot$ progenitor is a clear example of this, with neutrino luminosities roughly 25% higher than for the 19-$M_\odot$ progenitor. The 60-$M_\odot$ progenitor is an outlier, with lower luminosities and accretion rates than the 19- and 25-$M_\odot$ progenitors. [1] The sharp drop in the accretion rate (Fig. 5.2) and corresponding sharp drop − by as much as 30% − in the electron-neutrino and anti-neutrino

[1]We note that in general the mean neutrino luminosity in 2D evinces greater temporal variation than in 3D.

luminosities (Fig. 5.3), driven by changes in mass accretion rate, correspond to the accretion of the Si/O interface. The heavy neutrino luminosity is more sensitive to PNS convection (Radice et al. 2017) and shows a more muted drop.

The 13-, 14-, and 15-$M_\odot$ progenitors lack a sharp Si/O interface (Fig. 5.1), and fail to explode. The 9-$M_\odot$ progenitor also lacks a sharp interface, but explodes by virtue of its steep density profile and low gravitational binding energy. We emphasize that compactness does not correlate with explodability, as models with both higher and lower compactness than the 13-, 14-, and 15-$M_\odot$ progenitors do explode, consistent with conclusions from earlier work in 2D (Vartanyan et al. 2018b; Radice et al. 2017) and 3D (Vartanyan et al. 2019b; Burrows et al. 2019). Compactness is just one measure of profile shallowness, which is a multi-dimensional quantity for which useful fits do not yet exist. Compactness does roughly correlate with peak neutrino luminosity (see Fig. 5.3) consistent with earlier studies (Horiuchi et al. 2017) and with mean accretion rate (see Fig. 5.2) for all the exploding models. In Fig. 5.2, right panel, we plot compactness at 1.75 $M_\odot$ against total neutrino luminosity measured at the post-breakout bump. We see that the non-exploding models are outliers and have a slightly smaller neutrino luminosity for a given compactness, and do at late times not strictly follow the trend of higher compactness with higher neutrino luminosity.

To explore the angle dependence of the neutrino luminosity, we decompose the lab-frame luminosity up to its monopole, dipole, and quadrupole moments, filtering out spurious higher-order terms that are not handled well with the M1 closure scheme at large radii and low optical depth. We obtain for the luminosity:

$$L_{\nu_i}(\theta,\phi,t) = A_0\,Y_{00} + \sum_{m=-1}^{1} A_{1m}\,Y_{1m}(\theta,\phi) + \sum_{m=-2}^{2} A_{2m}\,Y_{2m}(\theta,\phi)\,,$$

where

$$A_{ij}(t) = \int_\Omega r^2 F_r[t,r,\theta,\phi] \times Y_{ij}[\theta,\phi]\,d\Omega\,, \tag{5.1}$$

and where the terms on the right-hand-side corresponding to the monopole, dipole, and quadrupole terms, respectively, for each neutrino species i $\in \{\nu_e, \bar{\nu}_e, \nu_\mu\}$. F_r is the radial flux outwards at a given radius, here taken to be 250 km.

In Fig. 5.4, we plot the luminosity decomposition in angle for the 19-$M_\odot$ progenitor for the $\nu_e, \bar{\nu}_e$, and ν_μ neutrino species as a function of time after bounce, truncated at the quadrupole term. In the top panel, we plot the monopole, dipole, and quadrupole terms for each species, summed in quadrature over azimuthal moments m, and in the bottom two panels we plot the dipole and quadrupole terms for each moment m. The dipole and quadrupole terms are never greater than several percent of the monopole term, and the heavy-neutrinos have the smallest deviations from spherical asymmetry. We see the dipole undergo a small number phases of growth until ∼200 ms, where turbulence becomes significant and we see a steep rise in the luminosity dipole. For all our models, the dipole component of the neutrino luminosity for all species is never more than ∼5-6% of the angle-averaged luminosity. We note that angle asymmetries in the luminosity are much smaller than asymmetries in the shock radius.

In Fig. 5.5, we plot in 3D the fractional variation in the electron-neutrino luminosity as a function of viewing direction and at various times for the 25-$M_\odot$ progenitor. In the top of each panel, we color-code and contour the fractional variation, with color and contour redundant with each other. Cool-colored dimples indicate lower-than-average neutrino luminosities, and warm-colored protrusions indicate higher-

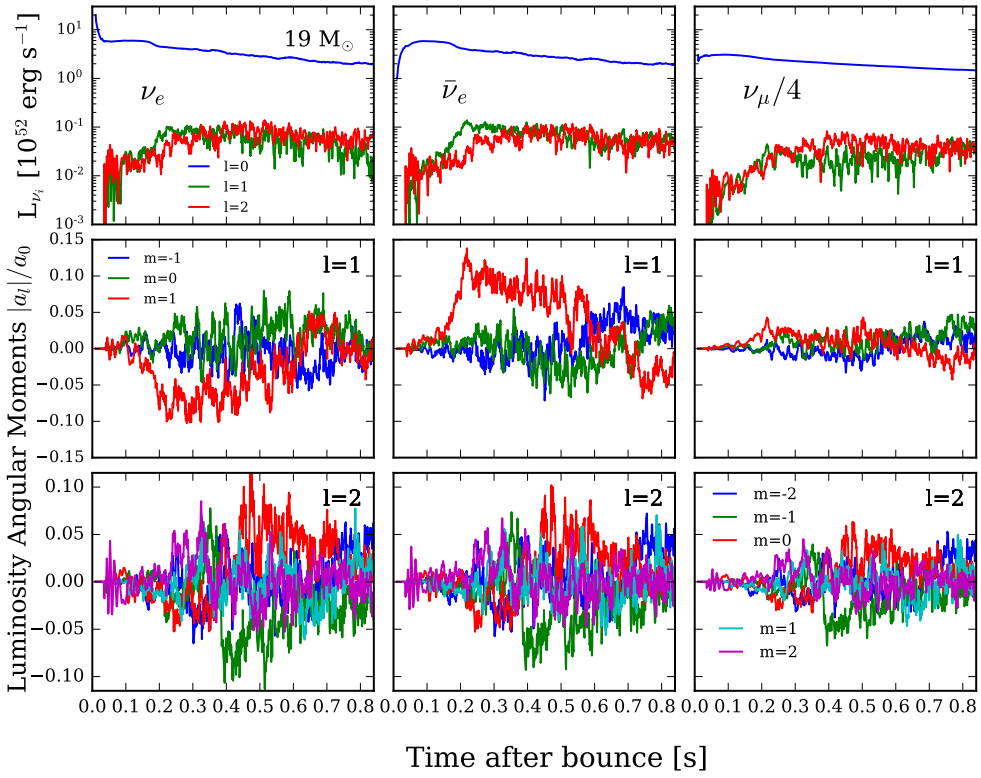

Figure 5.4: The luminosity decomposition by angle for the 19-$M_\odot$ progenitor for the ν_e, $\bar{\nu}_e$, and ν_μ species as a function of time after bounce (in seconds), truncated to the quadrupole term. In the top set of panels, we sum in quadrature over the ms. The dipole and quadrupole terms are never greater than several percent of the monopole term, and the heavy-neutrinos have the smallest angular deviations from spherical asymmetry. Fractional asymmetries in the neutrino luminosity are much smaller than fractional asymmetries in the shock radius. The middle, bottom horizontal panels provide the corresponding normalized angular moments of the neutrino luminosity for all the m components for $\ell = 1\,, \ell = 2$, respectively.

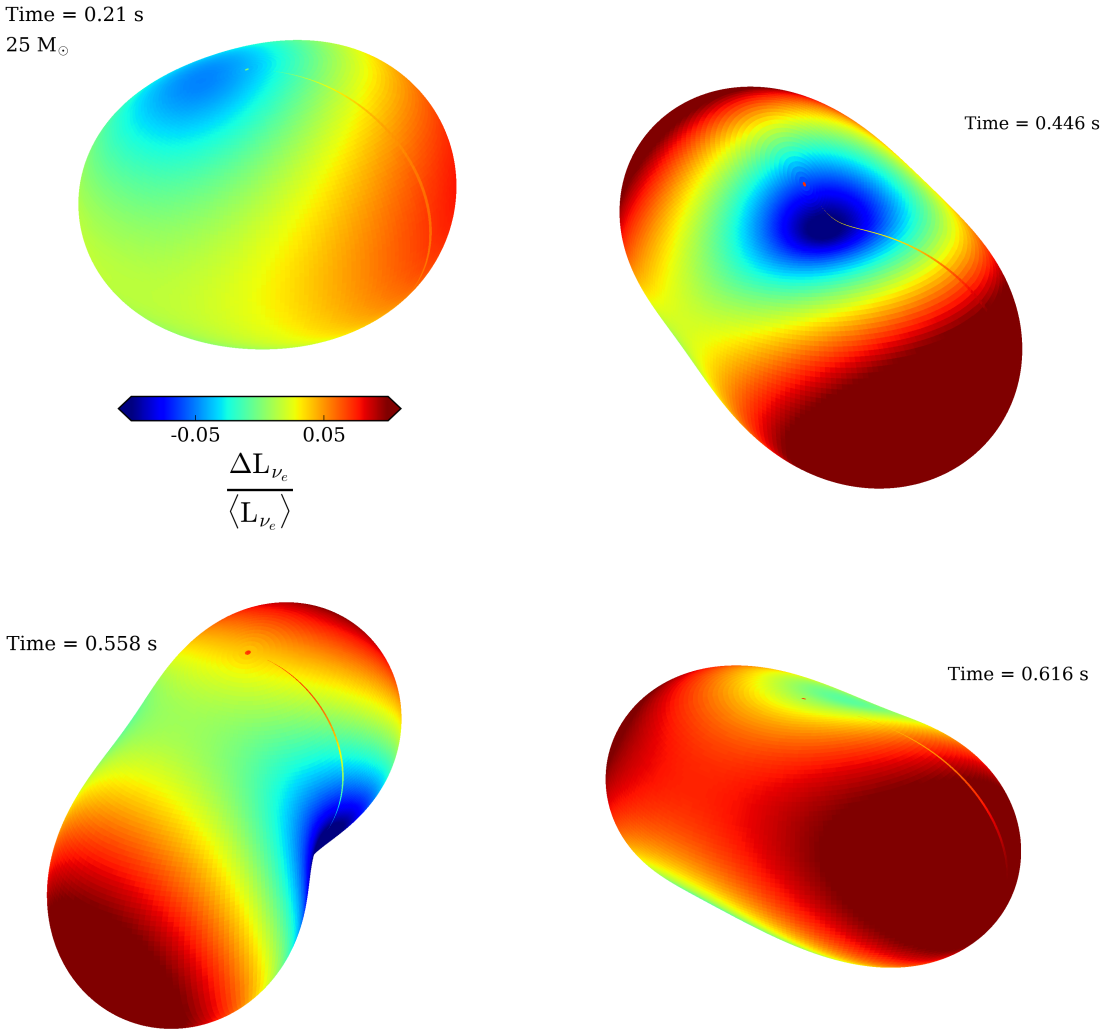

Figure 5.5: Fractional deviation from the mean in the ν_e luminosity as a function of viewing angle and at various times for the 25-$M_\odot$ progenitor. In the top of each panel. We color-code a region comensurate with the magnitude of the bulge, with color and radius are redundant. Cool-colored dimples indicate lower-than-average neutrino luminosities, and warm-colored protrusions higher-than-average. The stripe is the vestigial axis artifact.

than-average luminosities. The narrow stripe is the vestigial axis artifact. We see large-scale structure of the neutrino luminosity, with typical variations over viewing direction that increase with time to 5%−10%.

In Fig. 5.6, we plot histograms of the fractional emitting area at 250 km of the deviation from the mean neutrino luminosity for the three different species for several different progenitors. All models begin with isotropic neutrino emission and then evolve towards larger variations by viewing angle. Instantaneous neutrino emission can vary by as much as 40% over this sphere. We note that heavy-neutrinos typically show less angular variation in luminosity. The 15-$M_\odot$ progenitor, which does not explode, is consistently more isotropic in neutrino emission, even at later times.

We plot the corresponding solid-angle averaged RMS neutrino luminosity about its mean in Fig. 5.7 for the 19-$M_\odot$ progenitor. We see a hierarchy in fractional RMS neutrino luminosity by species; electron anti-neutrinos show the most variation, and heavy-neutrinos the least. The RMS variation increases with time; however, even at late times, the RMS variation is just ∼8%. Immediately after breakout, the variations are much smaller, roughly ∼1%. We see remarkable correlation between the different neutrino species in their RMS variation. This trend holds for all eleven models included in this study.

Given the small angular variation by direction in neutrino luminosities early on, future neutrino detections will not depend much on viewing angle after breakout and can be used to differentiate between core density structure and compactness (Fig. 5.3). Even up to 200−300 ms, variation by viewing angle will be dwarfed by the intrinsic differences in the luminosity by progenitor. Furthermore, observation of the ν_e and $\bar{\nu}_e$ neutrino luminosity can identify the presence and time of Si/O accretion.

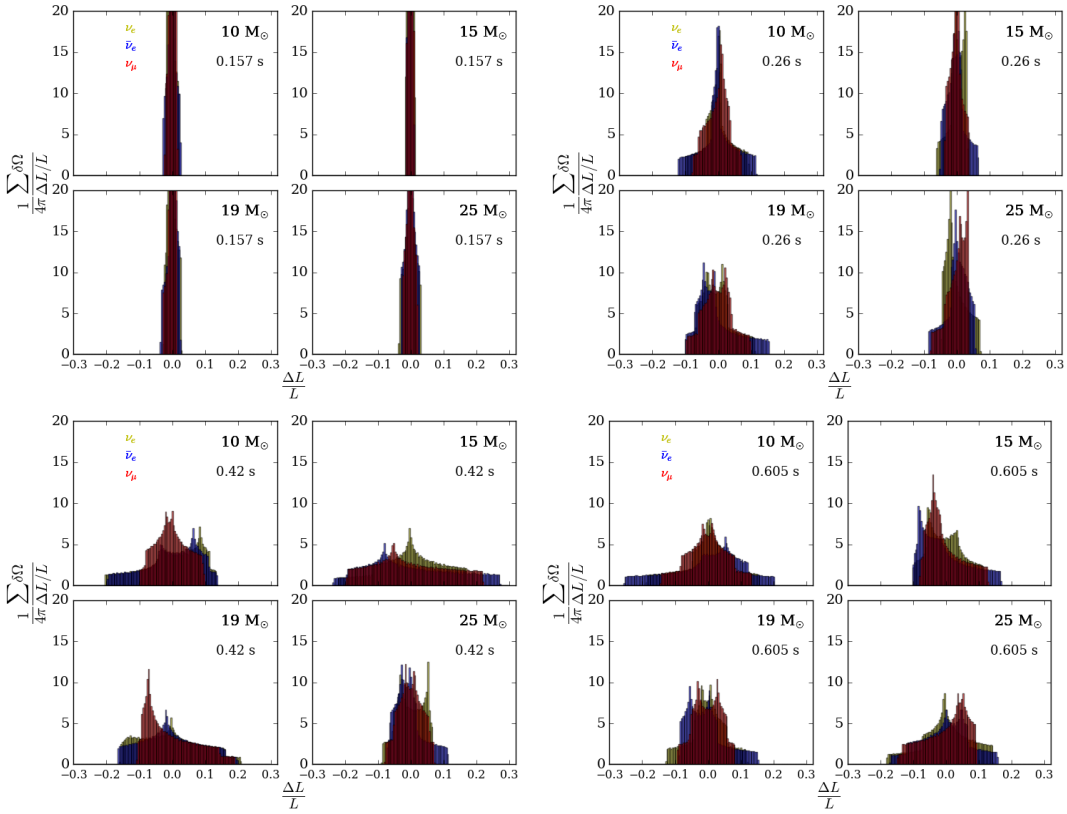

Figure 5.6: Histograms of the distributions of fractional deviation of the neutrino luminosity (of the three different species, yellow: ν_e, blue:$\bar{\nu}_e$, red: ν_μ) at 250 km from the mean ($\frac{\Delta L}{L}$) radiated into the 4π steradians of the sky for several different progenitors. The integral under each histogram curve is normalized to one. All models begin with isotropic neutrino emission then evolve towards larger variations with viewing angle. Instantaneous neutrino emission can vary by as much as 40% with viewing direction. We note that heavy-neutrinos typically show less temporal variation in luminosity. The 15-$M_\odot$ progenitor, which does not explode, is consistently more isotropic in neutrino emission, even at later times.

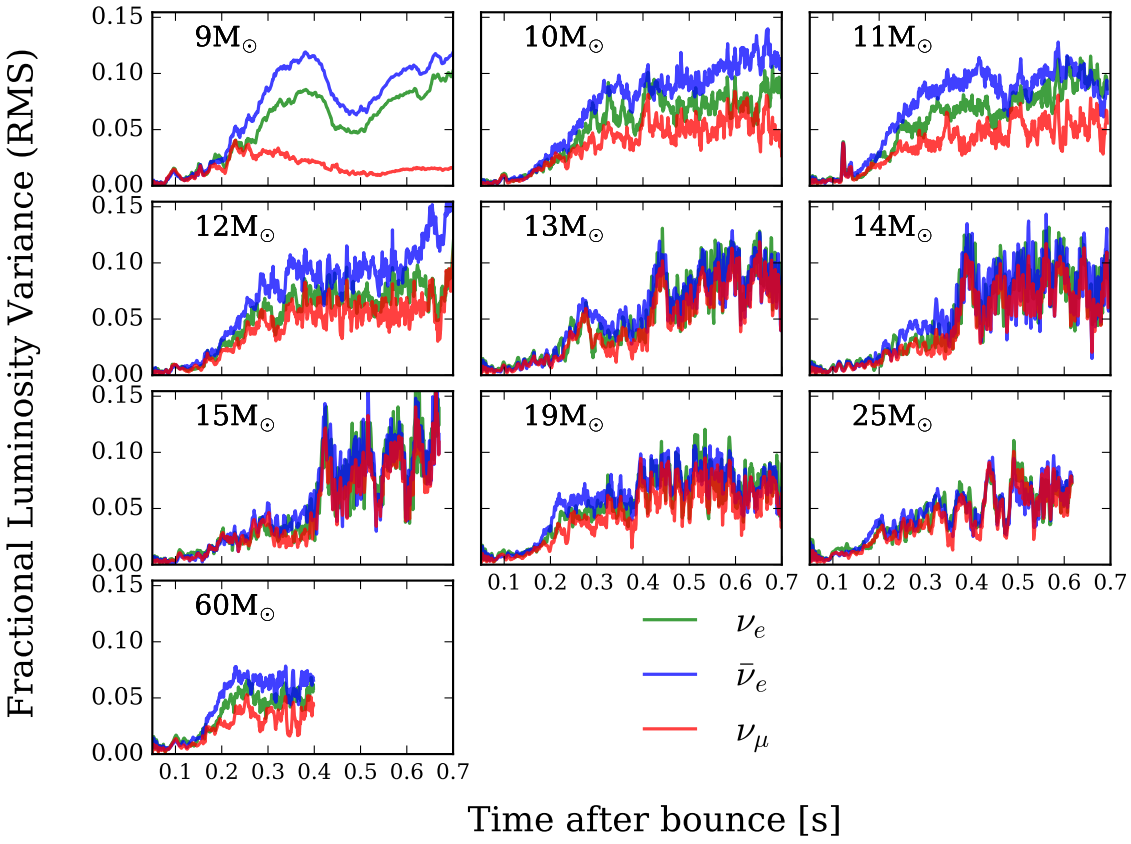

Figure 5.7: Root mean square (RMS) variation around the mean of the neutrino luminosities for the different neutrino species, normalized by the average neutrino luminosity for that species, as a function of time after bounce (in seconds). The fractional RMS is typically less than 8% of the neutrino luminosity, even at late times. Note the remarkable similarity in behavior for the different species. We observe a hierarchy in the fractional RMS, with the electron anti-neutrinos showing the greatest deviation from the mean, and the heavy-neutrinos the least. The 9-$M_\odot$ progenitor is the only progenitor that shows a drop in the RMS in the heavy-neutrino species just after $\sim$200 ms. This corresponds to the truncation of accretion and the end of the dynamic evolution of the 9-$M_\odot$ supernova - this model has asymptoted in explosion energy and all relevant diagnostics.

5.3.1 Neutrino Time Series

Here, we explore the time variability along an arbitrarily chosen viewing direction of the neutrino luminosity for the various species. We arbitrarily choose a viewing direction along $\theta = 49^\circ, \phi = 91^\circ$ in the spherical coordinate system of our simulated supernova. In the left panel of Fig. 5.8, we plot the neutrino luminosity of the different species as a function of time after bounce along this viewing direction (to be compared with Fig. 5.3, where we plot the angle-averaged neutrino luminosities). To probe the temporal variation, we subtract out the luminosity running average along the same viewing direction, using a window of 30 ms. We see a rough trend with progenitor mass of the neutrino temporal variations, with the 9-$M_\odot$ progenitor having less than 1% variations from the mean with time. The non-exploding models, 13-, 14-, and 15-$M_\odot$, show the greatest variation of all the models after 200 ms, with the development of the SASI manifesting as high-amplitude, high-frequency variations in the luminosity. These models show average temporal variation of $\sim$8%, with variations as high as 25%. By contrast, the exploding models show average temporal variation over $2-4\%$, with the 16-, 19-, 25-$M_\odot$ progenitors exhibiting variations as high as 10%.

Generally, the ν_e and $\bar{\nu}_e$ neutrino luminosities show the greatest temporal (and spatial) variation, while the ν_μ-neutrino luminosity exhibits the least temporal and spatial variation. In the right panel of Fig. 5.8, we plot the Fourier transform of the neutrino luminosity along the same viewing direction, subtracting out the running average along this same direction. The high-frequency components are associated with $\sim$few millisecond timescale PNS convection. The peaks in the heavier progenitors, around $\sim$10 Hz, indicate large scale explosion asymmetries. Note the 100 Hz peak in the non-exploding models, indicative of SASI, is absent in the exploding models.

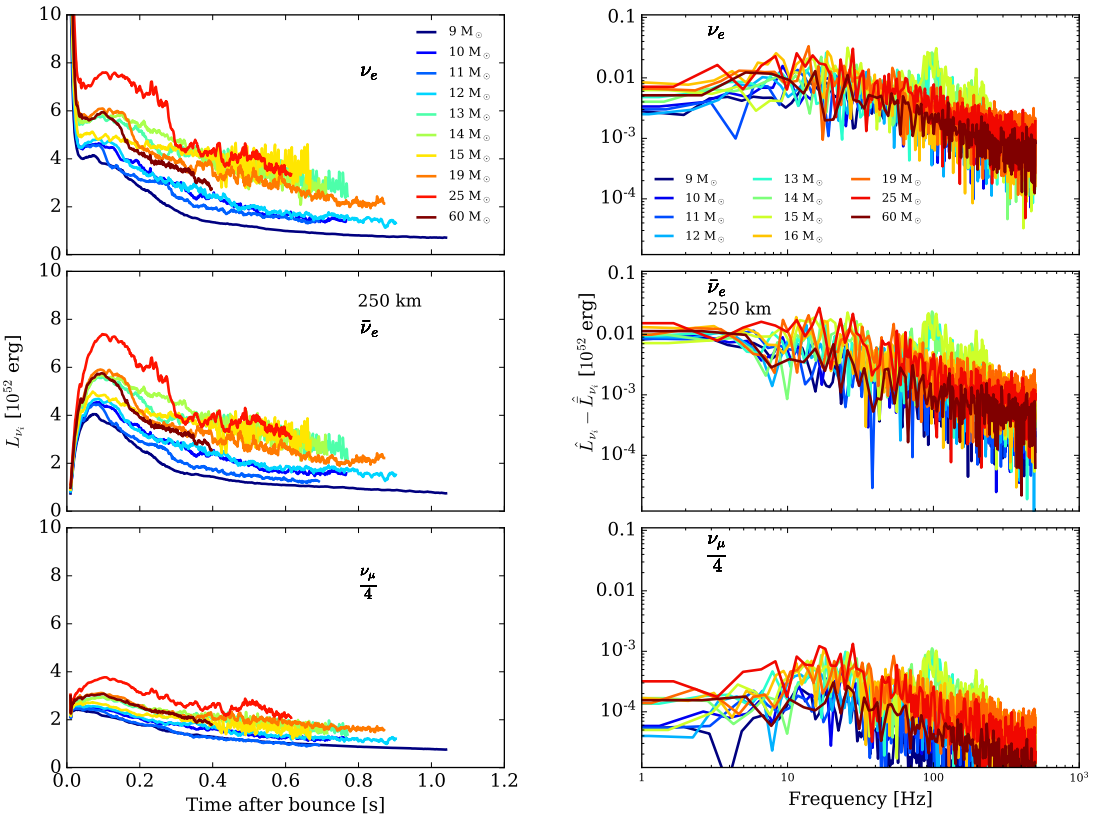

Figure 5.8: **Left**: The neutrino luminosity (in 10^{52} erg s^{-1}) as a function of time after bounce (in seconds) for the three species along an arbitrarily chosen viewing direction (selected as $\theta = 49°, \phi = 91°$ in the spherical coordinate system of the supernova, compare to the angle-average neutrino luminosity in Fig. 5.3). Note the greater variability for the non-exploding models. **Right**: The Fourier transform of the neutrino luminosities (in 10^{52} erg), subtracting out the running average over 30 ms, for the three species as a function of time after bounce (in seconds).

5.4 Temporal and Directional Variations of Gravitational Wave Emissions

In this section, we explore the spatial and temporal variations of the gravitational wave signatures of our suite of progenitors. We provide gravitational wave data for all models except the 16-$M_\odot$, for which we did not calculate the gravitational quadrupole moments. We follow Oohara et al. (1997) and Andresen et al. (2017), with the gravitational strain polarizations defined as

$$h_+ = \frac{1}{r}\left(\ddot{Q}_{\hat{\theta}\hat{\theta}} - \ddot{Q}_{\hat{\phi}\hat{\phi}}\right) \tag{5.2a}$$

$$h_\times = \frac{2}{r}\ddot{Q}_{\hat{\theta}\hat{\phi}} \tag{5.2b}$$

and the quadrupole moments defined as

$$\begin{aligned} Q_{\hat{\theta}\hat{\theta}} = {} & (Q_{xx}\cos^2\phi + Q_{yy}\sin^2\phi + 2Q_{xy}\sin\phi\cos\phi)\cos^2\theta \\ & + Q_{zz}\sin^2\theta - 2\left(Q_{xz}\cos\phi + Q_{yz}\sin\phi\right)\sin\theta\cos\theta \end{aligned} \tag{5.3a}$$

$$Q_{\hat{\phi}\hat{\phi}} = Q_{xx}\sin^2\phi + Q_{yy}\cos^2\phi - 2Q_{xy}\sin\phi\cos\phi \tag{5.3b}$$

$$\begin{aligned} Q_{\hat{\theta}\hat{\phi}} = {} & (Q_{yy} - Q_{xx})\cos\theta\sin\phi\cos\phi \\ & + Q_{xy}\cos\theta\left(\cos^2\phi - \sin^2\phi\right) + Q_{xz}\sin\theta\cos\phi\,. \end{aligned} \tag{5.3c}$$

In Fig. 5.9, we plot the gravitational wave strain times a distance (D) as viewed along the x-axis in the coordinate system of the supernova for the 10 models (neglecting the 16-$M_\odot$ model) and including both linear polarizations h_+ and $h_\times$. The strong prompt signal in h_+ (and absent in $h_\times$) in all models for the chosen viewing angle corresponds to the onset of prompt convection and indicates the symmetry of the imposed perturbations. The strain ramps up within the first $\sim$200 ms, and sub-

sequent to the prompt convection phase, both polarizations roughly follow each other in evolution. We see 'packets' in the strain lasting ∼50 ms corresponding to episodic accretion. Furthermore, in contrast with Pajkos et al. 2019, we find that the gravitational wave strain at core bounce, and throughout, generally increases with progenitor mass. We identify for all exploding models a direct correlation between the progenitor accretion rate and the magnitude of the gravitational strain, as concluded in Radice et al. (2019). The 9-, 10-, and 11-$M_\odot$ models have the lowest accretion rates, and correspondingly, the smallest strains, while the 19-, 25-, and 60-$M_\odot$ progenitors have the highest accretion rates and, correspondingly, the largest strains. For the 9-$M_\odot$, in particular, early cessation of the GW signal corresponds to the early cessation of accretion. This emphasizes the importance of carrying out simulations longer in 3D to understand their late-time behavior, through the end of the accretion phase, and the implications for observable signatures.

We note that the non-exploding 13-, 14-, 15-$M_\odot$ models have a weaker strain at later times despite sustained accretion. Furthermore, the gravitational strain for these non-exploding models grows for ∼200 ms, then is 'pinched' and decreases until ∼400 ms postbounce (when the spiral SASI develops), where it shows renewed growth.

In Fig. 5.10, we plot the spatial distribution of the gravitational strains h_+ D and $h_\times$ D, as dimples on a sphere of radius 5 cm, with the color and magnitude of the dimple corresponding redundantly to the strain. Hot colors and convex surfaces correspond to positive strain; cool colors and concave surfaces correspond to negative strain. The strain varies on sub-millisecond timescales with a dominant, large-scale quadrupolar morphology that differs between the different polarizations.

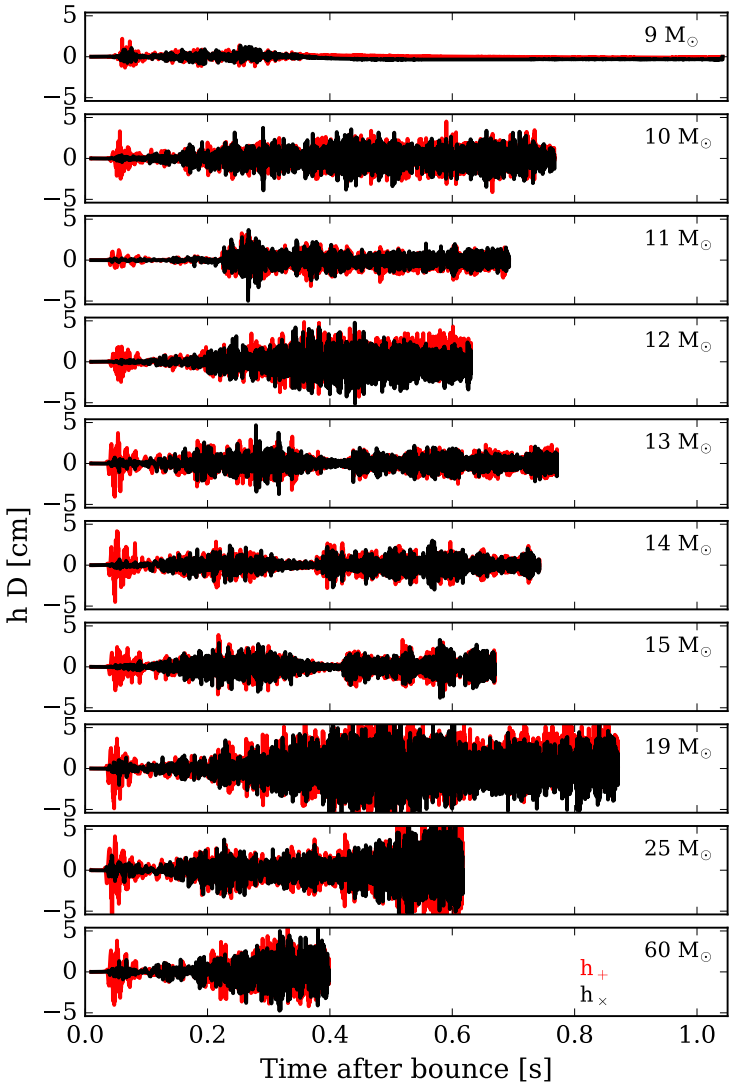

Figure 5.9: Gravitational wave strain $h_{+,\times}D$ (in centimeters, where D is the distance) as viewed along the x-axis in the coordinate system of the supernova as a function of time after bounce (in seconds) for the various models. The red lines show h_+ and the black lines $h_\times$. The strong prompt h_+ strain for the selected viewing angle, absent in $h_\times$, corresponds to prompt convection and is indicative of the symmetry of the perturbations implemented. Afterwards, the two polarizations roughly follow each other in evolution. Note the cessation in the GW signal for both polarizations for the 9-$M_\odot$ progenitor, shortly after accretion ends (Radice et al. 2019). For the remaining models, the strain ramps up within ∼200 ms, and its magnitude is approximately correlated with progenitor mass. For the non-exploding models (13-, 14-, and 15-$M_\odot$ progenitors), the accretion rate, after growing for ∼200 ms, is 'pinched' and drops until ∼400 ms postbounce (where we see the spiral SASI develop), when it is revitalized.

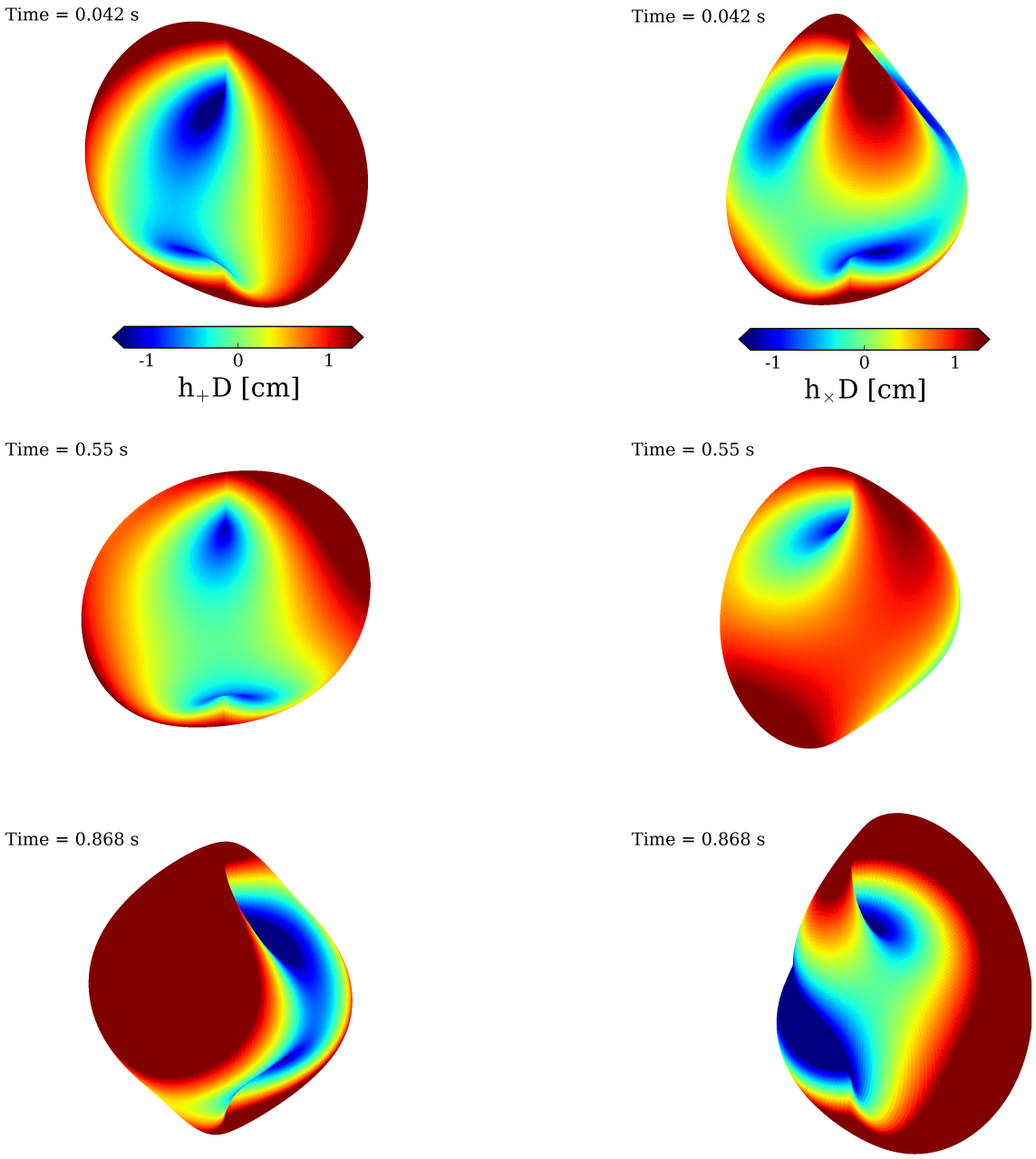

Figure 5.10: Gravitational strain $h_{+,\times}$ D in cm (h_+ **left**, $h_\times$ **right**) as a function of viewing angle and at various times for the 19-$M_\odot$ progenitor. The contours are overplotted on a surface of 5 cm to accentuate the variations. The color and contours are redundant, with hotter colors and convex surfaces indicating positive strains, and cooler colors and convex surfaces negative strains. We see variations in gravitational wave emission on sub-millisecond timescales associate with p-modes in the turbulent region and the frequency growth of the f-mode (see Fig. 5.11). The morphologies vary between the two polarizations, with the h_+ contour surface shaped like a pinched dumpling, and the $h_\times$ surface a guitar pick.

5.5 SASI

In this section, we provide an aside on the SASI. The standing accretion shock instability (SASI; Foglizzo 2002; Blondin et al. 2003; Blondin & Shaw 2007; Foglizzo et al. 2012), is a vortical-acoustic hydrodynamic instability in the post-shocked region manifested (when it appears) by non-radial oscillating motion. To identify the SASI, we search for a low-frequency ($100 - 250$ Hz) gravitational wave signature lasting several hundred milliseconds (Kuroda et al. 2016a; Andresen et al. 2019). We confirm the presence of the SASI by looking for a stately shock dipole in Fourier space at similar frequencies. We find evidence for the SASI in four of the models considered: the 13-,14-, and 15-$M_\odot$ progenitors (which do not explode), and the 25-$M_\odot$ progenitor (which explodes later, around 275 ms). All three of the non-exploding models also show an $m = 1$ spiral SASI mode (Blondin 2005) developing $\sim$400 ms postbounce, after the early SASI phase, when the stalled shock radius has receded. The spiral SASI is a three-dimensional feature observed in earlier simulations (Kuroda et al. 2016a; Summa et al. 2018; Andresen et al. 2019) and cannot be seen in axisymmetric two-dimensional simulations.

Earlier 2D, axisymmetric simulations (Scheck et al. 2008; Marek & Janka 2009; Hanke et al. 2012; Summa et al. 2016) have suggested that the SASI enhances neutrino energy deposition to promote explosion. However, comparisons with ray-by-ray and multi-dimensional neutrino transport (Skinner et al. 2016; Dolence et al. 2015; Glas et al. 2018) indicated that axisymmetric 2D simulations artifically enhance axial sloshing associated with the SASI to promote explosion.

We emphasize that the development of a SASI − in 3D as well as 2D − is mainly restricted to failed explosions, with a smaller shock radius favorable to a faster growth rate via the advective-acoustic cycle (Foglizzo 2002). This is congruent with earlier work (Vartanyan et al. 2019b) claiming that the SASI frequently appears in the context of delayed or failed explosions and more compact shock structures.

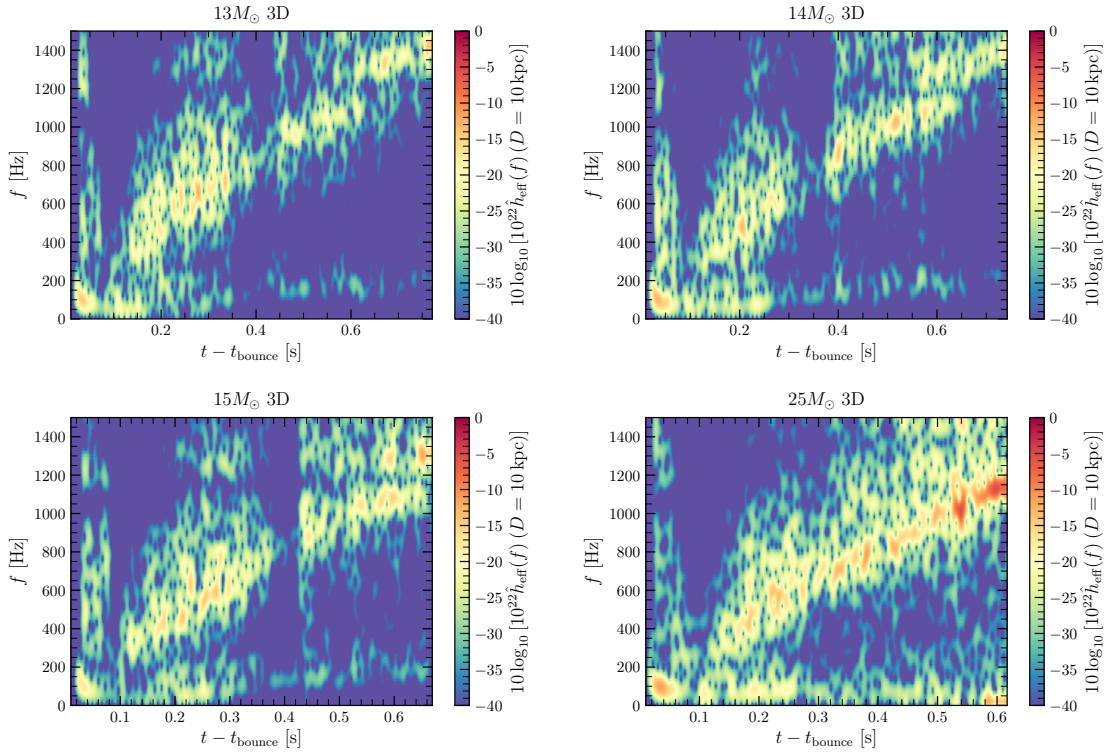

Figure 5.11: Gravitational wave spectrograms of the four models (13-, 14-, 15-, and 25-$M_\odot$) that exhibit some form of the SASI. Prior to 100 ms, we see the development of a low-frequency (less than 100 Hz) component associated with prompt convection. The fundamental mode frequency increases quadratically with time to 1 kHz by $\sim$500 ms postbounce (see also Morozova et al. 2018b). Up to $\sim$250 ms, we see the telltale $\sim$100 Hz gravitational wave signature for all four models indicating the development of the SASI. These models either fail to explode, or explode late. After $\sim$400 ms, we see the development of a higher-frequency spiral SASI – indicated by a gravitational wave signature at less than 200 Hz – in the 13-, 14, and 15-$M_\odot$ progenitors, all of which fail to explode. The low-energy, low-frequency component after $\sim$300 ms in the 25-$M_\odot$ progenitor does not correspond to the SASI, but is rather the linear memory due to an asymmetric explosion, and is visible in the spectrograms of all exploding models. The 25-$M_\odot$ progenitor explodes and shows no spiral SASI. The SASI signal is weaker than the f-mode frequency for all models considered. We see sub-millisecond power due to f- and p-modes in turbulent regions (visible in the spectrogram as power at frequencies greater than 1 kHz).

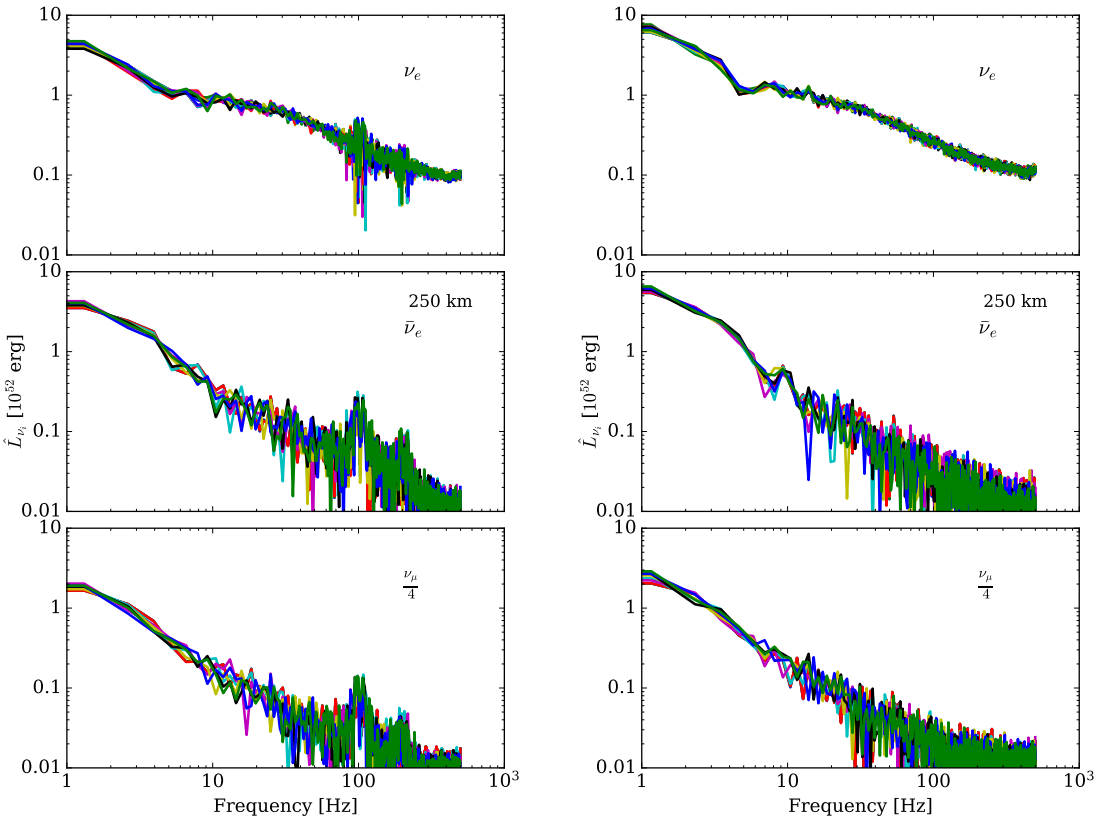

Figure 5.12: We plot the Fourier transform $\hat{L}$ over an entire simulation of the luminosity at 250 km for the 13- (**left**, failed explosion) and 19-$M_\odot$ (**right**, successful explosion) progenitors along multiple lines-of-sight, indicated by the different colors, for all neutrino species. Note the strong peak in all species for the non-exploding 13-$M_\odot$ progenitor at ∼100 Hz (and a smaller peak at 200 Hz), indicative of the SASI. In the exploding 19-$M_\odot$, we see a peak at 10 Hz, but no peak near ∼100 Hz. See text for a discussion.

In Fig. 5.11, we portray gravitational-wave spectrograms of the four models (13-, 14-, 15-, and 25-$M_\odot$) that exhibit some form of the SASI. Prior to 100 ms, we see the development of a low-frequency (less than 100 Hz) component associated with prompt convection. The fundamental mode (f-mode) frequency increases with time to 1 kHz by $\sim$500 ms postbounce (Morozova et al. 2018b). Up to $\sim$250 ms after bounce, we see the telltale $\sim$100 Hz gravitational wave signature for these four models indicating the development of the the SASI. These models either fail to explode, or explode late. After $\sim$400 ms, we see the development of a spiral SASI $-$ indicated by a gravitational wave signature of less than $\sim$200 Hz $-$ in the 13-, 14-, and 15-$M_\odot$ progenitors, all of which fail to explode. The low-energy, low-frequency component after $\sim$300 ms in the 25-$M_\odot$ progenitor does not correspond to the SASI, but is due to the long-term global motions, such as expansion mass asymmetries. This signature is present only in the exploding models. The 25-$M_\odot$ progenitor explodes and shows no spiral SASI. The SASI signal is weaker than the fundamental mode frequency for all models considered.

In Fig. 5.12 we plot the Fourier transform of the luminosity for the 13- (failed explosion) and 19-$M_\odot$ (successful explosion) progenitors along multiple, arbitrarily chosen, lines-of-sight, indicated by the different colors, for all neutrino species. Note the strong peak at $\sim$100 Hz in all neutrino species for the non-exploding 13-$M_\odot$ progenitor at $\sim$100 Hz, indicative of the SASI. In the exploding 19-$M_\odot$, we see a clear peak at $\sim$10 Hz, and the $\sim$100 Hz SASI signal is absent.

Summa et al. (2018) find dynamic shock expansion due to kinetic energy deposition in the SASI spiral arm, driving their models to explosion. In our (non-rotating models), we do not witness shock revival for the three failed models where the spiral SASI does develop. Therefore, when the SASI appears in our non-rotating models, it is usually in the context of receding shocks and failed explosions. The turbulence seen

is always predominantly a consequence of neutrino-driven convection, and exploding models rarely show any signs of the SASI, at least for our non-rotating model set.

5.6 LESA

The lepton-number emission self-sustained asymmetry (LESA) was proposed by Tamborra et al. (2014a) as a neutrino-hydrodynamical instability resulting in $\nu_e - \bar{\nu}_e$ emission asymmetry, with possible implications for nucleosynthesis (Fujimoto & Nagakura 2019). In later work, Vartanyan et al. (2018b); O'Connor & Couch (2018a) identified the LESA by examining the dipole component of the spherical harmonic decomposition of the net lepton number flux ($\mathrm{F}_{\nu_e} - \mathrm{F}_{\bar{\nu}_e}$) for a single simulation in 3D of the 16-$\mathrm{M}_\odot$ progenitor (Woosley & Heger 2007). Walk et al. (2018) found that, for rotating models, the LESA instability is suppressed associated with weaker PNS convection and Walk et al. (2018), Glas et al. (2018), and Walk et al. (2019) have studied possible connections between neutrino emissions, neutrino oscillations, and the LESA.

We now extend our exploration of the possible presence of the LESA to 11 progenitors evolved in 3D. In Fig. 5.13, we depict the monopole and dipole components of the lepton asymmetry as a function of time after bounce at 500 km. Here, we follow O'Connor & Couch (2018b) and plot the dipole magnitude,

$$A_{\mathrm{dipole}} = 3 \times \sqrt{\sum_{i=-1}^{1} a_{1i}^2, }, \tag{5.4}$$

using the normalization scheme of Burrows et al. (2012).

For all of our models – irrespective of explosion outcome – we see the development of the LESA, and illustrate the monopole and dipole components of this asymmetry in Fig. 5.13, consistent with recent 3D simulations (O'Connor & Couch 2018b; Glas

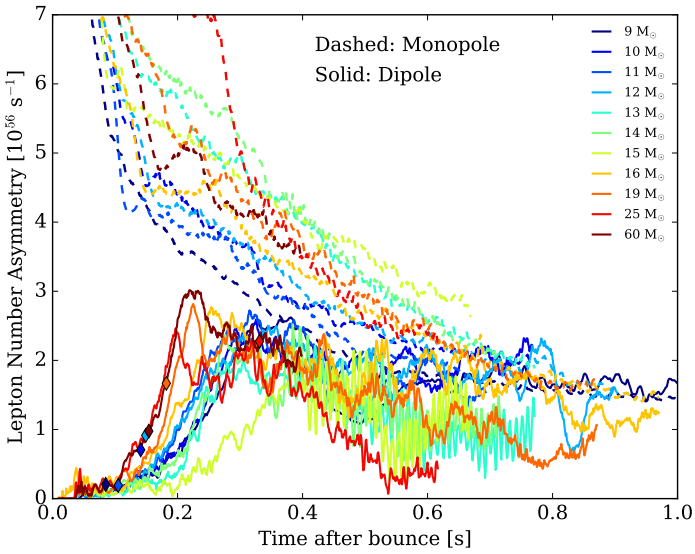

Figure 5.13: The monopole and dipole components of the LESA (at 500 km) as a function of time after bounce (in seconds). In all models, we see the development of the LESA at or shortly after ∼200 ms. The LESA disappears after ∼500 ms for the 25-$M_\odot$ progenitor and abates in magnitude for all but the lowest mass progenitors.

et al. 2018). Note the strong periodicity in the non-exploding models (13-, 14-, 15-$M_\odot$) after 400 ms, as the spiral SASI develops. We do not find strong evidence that the LESA correlates with either the behavior of the shock surface or the accretion rate; rather, as we note in § 5.7, it is the neutrino luminosity itself that correlates with the shock radius and accretion rate temporal oscillations, in agreement with Dolence et al. (2015).

In Fig. 5.14, we plot the θ and ϕ components of the orientation of the LESA dipole axis, and of the radius-weighted dipole axis of the electron fraction distribution at 25 km, following the prescription of O'Connor & Couch (2018a). For all eleven models, we see remarkable correlation between the orientation of the LESA dipole axis and the dipole axis of the electron-fraction distribution in the convective PNS. We see that the Y_e dipole precedes that of the LESA by ∼2 ms, which can be explained by the light travel time from the PNS to 500 km, where we measure the LESA. These results

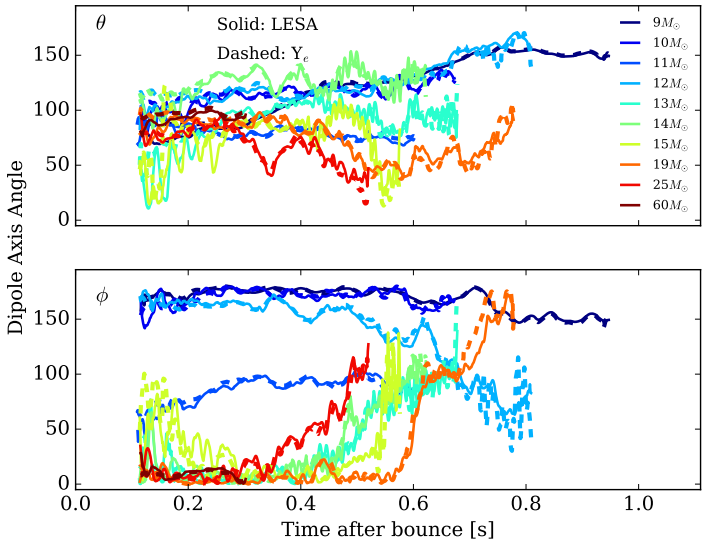

Figure 5.14: The orientation of the LESA dipole (at 500 km) and the Y_e dipole (measured at 25 km, tracing PNS convection) for the various models considered. For all models, we see that the LESA evolution closely correlates with the Y_e evolution. It trails the Y_e evolution by $\sim$2 ms, corresponding to the light travel time from the PNS to 500 km. See text for a discussion.

build on recent evidence (O'Connor & Couch 2018a; Glas et al. 2018) to suggest that hemispheric differences in PNS convection drive the LESA dipole.

5.7 Neutrino and Gravitational Wave Emission Correlations

In this section, we explore correlations of the potentially observable neutrino and gravitational wave signatures with the inner dynamics of the supernova. In Fig. 5.15, we plot the normalized (by the monopole) dipole components of the accretion rate (blue, at 100 km), shock surface (black), LESA (brown), and neutrino luminosities (solid-red for electron-neutrinos, dashed-red for electron anti-neutrinos, and green for heavy-neutrinos, at 500 km). We use the approach outlined in Burrows et al. (2012) to decompose the shock surface $R_s(\theta, \phi)$ into spherical harmonic components with

coefficients:

$$a_{lm} = \frac{(-1)^{|m|}}{\sqrt{4\pi(2l+1)}} \oint R_s(\theta,\phi) Y_l^m(\theta,\phi) d\Omega \,, \tag{5.5}$$

normalized such that $a_{00} = a_0 = \langle R_s \rangle$ (the average shock radius). a_{11}, a_{1-1}, and a_{10} correspond to the average Cartesian coordinates of the shock surface dipole $\langle x_s \rangle$, $\langle y_s \rangle$, and $\langle z_s \rangle$, respectively. The orthonormal harmonic basis functions are given by

$$Y_l^m(\theta,\phi) = \begin{cases} \sqrt{2} N_l^m P_l^m(\cos\theta) \cos m\phi & m > 0 \,, \\ N_l^0 P_l^0(\cos\theta) & m = 0 \,, \\ \sqrt{2} N_l^{|m|} P_l^{|m|}(\cos\theta) \sin |m|\phi & m < 0 \,, \end{cases} \tag{5.6}$$

where

$$N_l^m = \sqrt{\frac{2l+1}{4\pi} \frac{(l-m)!}{(l+m)!}} \,, \tag{5.7}$$

$P_l^m(\cos\theta)$ are the associated Legendre polynomials, and θ and ϕ are the spherical coordinate angles. We define the norm,

$$A_\ell = \frac{\sqrt{\sum_{m=-\ell}^{\ell} a_{\ell m}^2}}{a_{00}} \,. \tag{5.8}$$

We see a hierarchy, with the normalized accretion rate dipole being largest, and that for the neutrino luminosity smallest. Non-exploding models have smaller accretion rate dipoles. We see that ν_e and $\bar{\nu}_e$ neutrino luminosities have comparable normalized dipoles, with the $\bar{\nu}_e$ dipole slightly larger, and the ν_μ neutrino luminosity having the smallest dipole. This may attest to the different neutrinosphere radii for the different neutrino species, though the temporal variations of their luminosities track each other. We see remarkable similarity between the oscillations in the luminosity dipole and shock surface dipole, with the former lagging by $\sim$5$-$10 ms at early times, prior to explosion, due to advection of accreta from the stalled shock to the neutrinosphere. The shock radius dipole has longer period variations, of $\sim$10 ms and

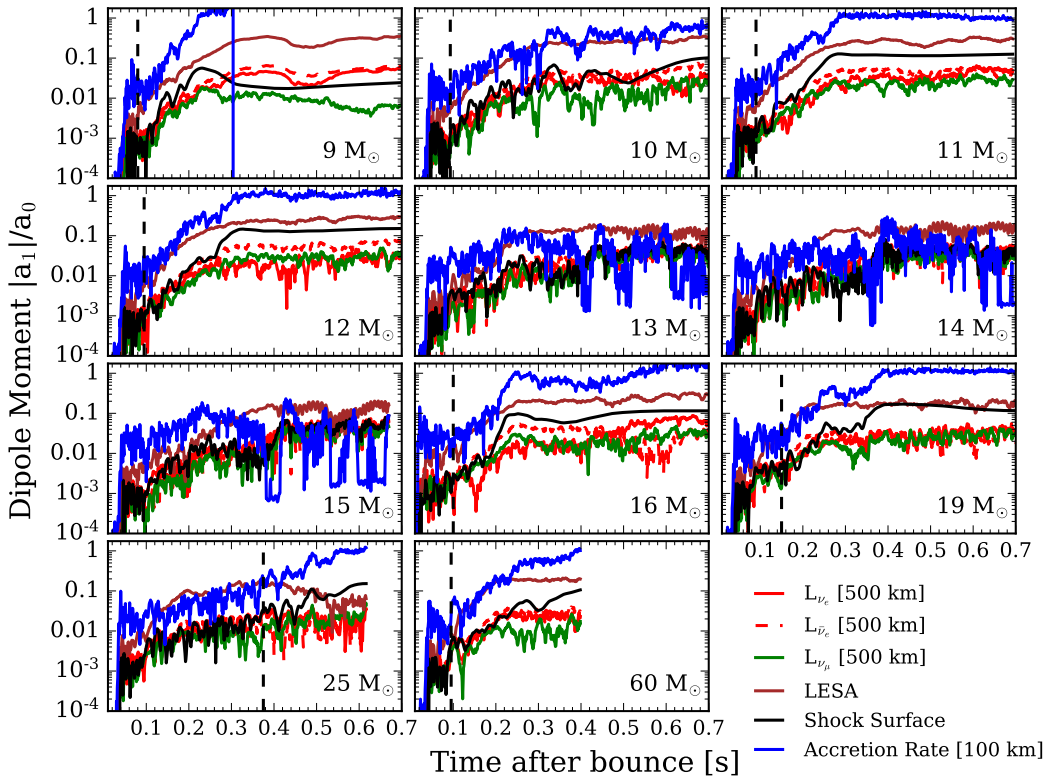

Figure 5.15: The normalized dipole components of the accretion rate (blue, at 100 km), shock surface (black), and neutrino luminosities (solid-red for electron-neutrinos, dashed-red for electron anti-neutrinos, and green for heavy-neutrinos, at 500 km). We see a hierarchy, with the normalized accretion rate dipole being largest, and that for the neutrino luminosity smallest. Among the neutrino luminosities, the electron-neutrino and anti-neutrino luminosities have comparable normalized dipoles, with the anti-neutrino dipole slightly larger, and the heavy-neutrino having the smallest dipole. This may attest to the different positions of the neutrinospheres for the different neutrino species. Notably, the non-exploding models have smaller accretion rate dipoles.

greater, and settles earliest after explosion, asymptoting to a roughly constant value in those models whose explosion energies have also begun to asymptote (Radice et al. 2019). The shock surface lies interior to ∼500 km at the early times plotted here, out to ∼300 ms. The 25-$M_\odot$ progenitor shows the clearest correlation between accretion and luminosity; its later explosion is powered by a higher sustained accretion rate and consequent neutrino luminosity.

To correlate the time variation of the shock radii, the accretion rate, and the neutrino luminosities, we investigated their Fourier frequency content. Prior to explosion, we generally see large amplitude variation for these physical quantities on short timescales of ∼5 ms. After explosion, the dipole of the shock radii, neutrino luminosities, and accretion rates transition to small amplitude, long-period variations. In the accretion rate and neutrino luminosities, we see fast temporal variation with timescales of ∼5 ms, within a broader, quasi-periodic envelope with a typical width of ∼40 ms but as high as ∼100 ms, corresponding to large-scale anisotropies of the shock motion modulating the accretion rate. The 9-$M_\odot$ progenitor, whose explosion proceeds relatively isotropically and whose accretion phase ends early, lacks such a feature. Additionally, for the first ∼400 ms, of − for example, − the 25-$M_\odot$ progenitor's evolution, we see variation on ∼30 ms timescales, corresponding to advection of material from the (initially) slowing growing shock.

For the non-exploding models, the shock radius, accretion rate, and neutrino luminosity all sustain persistent, short-timescale variations even at late times, ∼500 ms postbounce. Furthermore, we see in non-exploding models a transition to shorter timescales and higher frequencies (see Fig. 5.16 and following) after ∼400 ms, coincident with the development of the spiral SASI thereabouts. This is most visible in the 14-$M_\odot$ model, for which we see periodic ∼10-ms variations after ∼400ms in the shock surface, accretion rate, and neutrino luminosity dipoles (for all species). After the spiral SASI develops, we also see large drops by two orders of magnitude

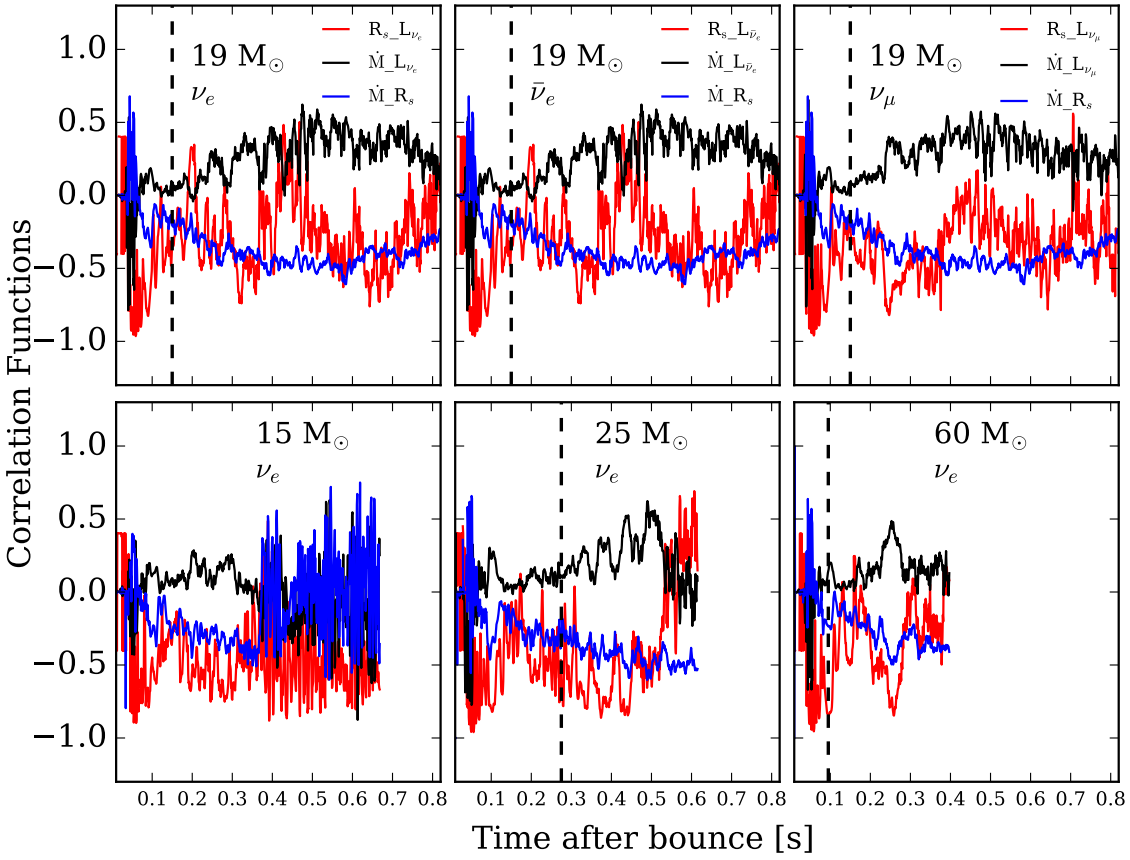

Figure 5.16: Angle-correlations between the various physical quantities depicted for the 19-M$_\odot$ progenitor (**top**) and other various progenitors (**bottom**). From left to right in the top panel, these correlations are shown for different neutrino species for the 19-M$_\odot$. We note the strong dependence of heavy-neutrinos on the accretion rate. We see correlation between the luminosity and accretion rate, and anti-correlation between the luminosity and shock radius, and shock radius and accretion rate for all models, exploding and non-exploding alike. After ∼300 ms, the non-exploding models (the 15-M$_\odot$ progenitor is shown here) show no persistent correlation, but rather high-frequency oscillation around zero, indicative of SASI activity. See text for a discussion.

in the dipole of the accretion rate over ∼80 ms timescales. Concurrently, and for the non-exploding models alone, we see the development of periodic 10-ms oscillations of the LESA dipole, which we associate with the spiral motion of the SASI, perhaps due to modulation of infalling accretion. The LESA dipole shows little to no temporal variation for the exploding models. While the 25-$M_\odot$ progenitor does show early SASI activity, it explodes without a spiral SASI developing. We reiterate that ∼10 ms periodicity of the neutrino luminosity several hundred milliseconds after bounce is an indicator of spiral SASI activity.

We follow the formalism of Kuroda et al. (2017) to calculate the time-dependent angle-integrated correlation $X\,(t)$ between two physical quantities, $\mathrm{A}_1\,(\Omega)$ and $\mathrm{A}_2\,(\Omega)$,

$$X\,(t) = \frac{\int A_1\,(t,\Omega)\,A_2\,(t,\Omega)\,d\Omega}{\sqrt{\int A_1\,(t,\Omega)^2 d\Omega \int A_2\,(t,\Omega)^2\,d\Omega}}\,. \tag{5.9}$$

In Fig. 5.16, we plot angle-averaged correlations as a function of time after bounce between the shock radius and neutrino luminosity, shock radius and accretion rate, and accretion rate and neutrino luminosity for various progenitors. In the top panel, we show the correlation with the neutrino luminosities of different neutrino species for the 19-$M_\odot$ progenitor. We note the dependence of the heavy-neutrino luminosity on the accretion rate. We see correlation between the luminosity and accretion rate, and shock radius and accretion rate, and weaker anti-correlation both between the luminosity and shock radius, for all models exploding and non-exploding alike. However, after ∼300 ms, the non-exploding models show no persistent correlation, but rather show variation around zero on ∼10-ms timescales, illustrating SASI activity.

In Fig. 5.17, we visualize the above angle correlations by plotting a Mollweide projection of the dipole directions of the LESA at 500 km (square), $\mathrm{Y_e}$ (circle) in the convective PNS at 25 km, the shock radius (triangle), and the antipode of the accretion rate at 100 km (diamond) at a snapshot 536 milliseconds after bounce for

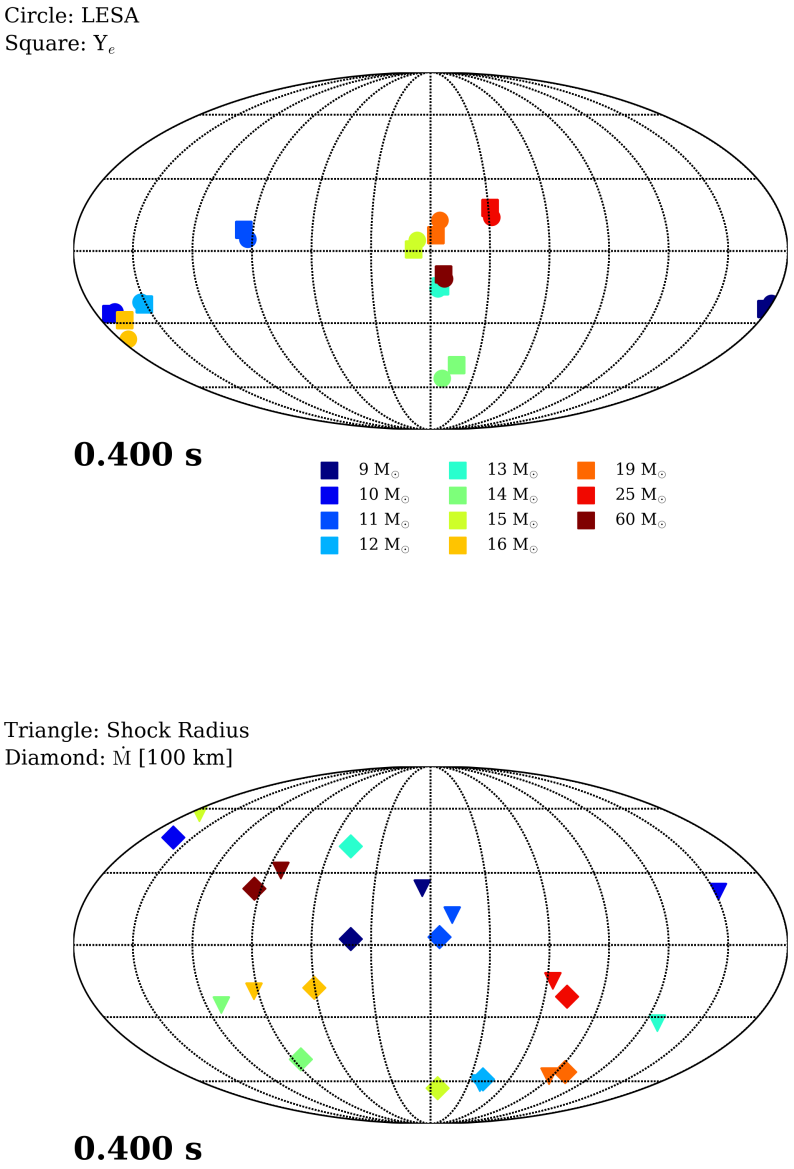

Figure 5.17: **Top**: Mollweide projection of the dipole directions of the LESA at 500 km (square) and Y_e (circle) in the convective PNS at 25 km at 400 ms postbounce. **Bottom**: The shock radius (triangle), and the antipode of the accretion rate at 100 km (diamond) 400 ms after bounce for all progenitor models studied here. The LESA dipole closely traces the Y_e dipole when the LESA is active. Similarly, for the exploding models, the shock radius dipole strongly anti-correlates with the accretion rate.

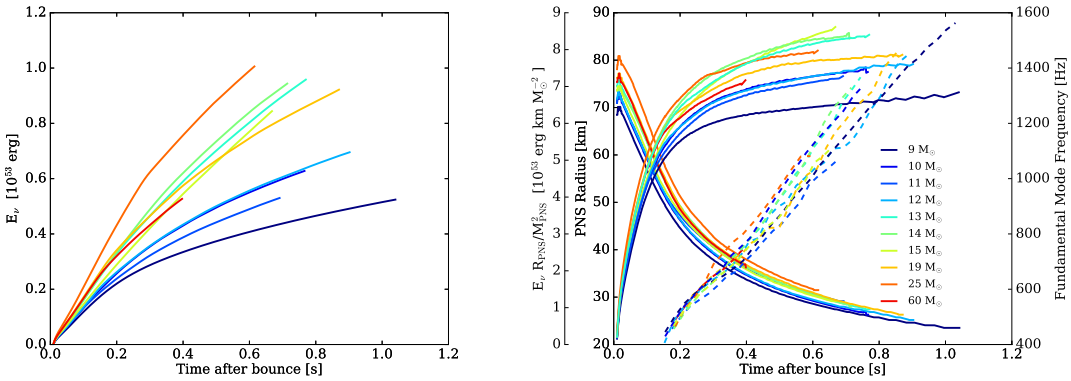

Figure 5.18: **Left**: The total neutrino energy loss as a function of time after bounce (in seconds) for all progenitors highlighted here. **Right**: The PNS radius (km) on the left y-axis and the gravitational wave fundamental mode frequency (dashed lines), right y-axis, as a function of time after bounce (in seconds). We also plot the total neutrino energy loss normalized by the Newtonian binding energy of the PNS. As the PNS radiates neutrinos and loses energy, it contracts and the fundamental (f-) mode frequency increases. Neglecting the 9-$M_\odot$ progenitor, normalizing energy-loss by PNS mass results in a smaller variation, $\sim$10%, by progenitor mass. Roughly, we see a correlation between highest neutrino energy loss (**left**), and smallest PNS radii (**right**). As seen in Morozova et al. (2018b), at later times the fundamental mode frequency begins to turn over quadratically (most visible here for the 9-$M_\odot$, carried out furthest). However, models need to be carried out to later postbounce times for this to be easily discernible.

all progenitor models studied. The LESA dipole closely traces the Y_e dipole when the LESA is active. For the non-exploding models, we see precession of the LESA dipole direction around the Y_e dipole direction as the spiral SASI develops. In the bottom panel, we plot the antipode of the accretion rate to illustrate its strong anti-correlation in direction with the shock radius.

In Fig. 5.18, we plot the PNS radius, integrated energy lost by neutrinos, and the fundamental mode frequency of the emitted gravitational waves as a function of time. Increasing neutrino energy losses cause the core to shrink and the fundamental mode frequency to increase. Both the fundamental mode frequency and the PNS radii show less than $\sim$10% scatter with progenitor mass. The total energy lost is normalized by the Newtonian binding energy of the PNS to reduce scatter. Four

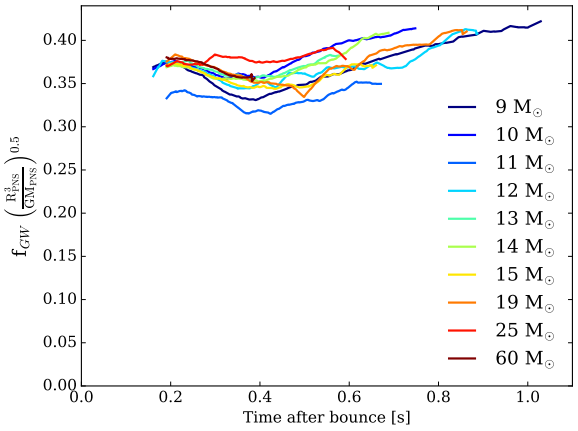

Figure 5.19: The gravitational wave fundamental mode frequency normalized by PNS dynamical time, a function of the PNS radius and mass, for the various progenitors plotted versus time after bounce (in seconds). We see little variation, approximately $\sim$10% in the normalized fundamental frequency, which is itself approximately 0.35 $\times$ the dynamical time 500 ms after bounce and tends to increase with time. See text for a discussion.

hundred milliseconds after bounce, the PNS's have typical radii of $\sim$38 km and f-mode gravitational wave frequencies of $\sim$800 Hz. To illustrate the correlation between the PNS radii and f-mode frequency, we find a least-squared fit to the mean behavior,

$$R_{\rm PNS}[{\rm km}] \approx 46 \times \left(\frac{f[{\rm kHz}]}{1.3} - 0.23\right)^{-0.25}, \tag{5.10}$$

where the best-fit power lies between 0.25 and 0.31, or conversely, we can invert to find that the fundamental mode frequency scales as the PNS radius to the 3 to 4 power, to a multiplicative constant and additive offset. We emphasize that this scaling is for illustrative purposes, to indicate the PNS-probing power of future supernovae GW detections, and can certainly be improved upon.

The f-mode gravitational waves depend approximately upon the average density of the PNS (Müller et al. 2013; Sotani et al. 2019; Torres-Forné et al. 2019). In Fig. 5.19, we plot the gravitational wave fundamental mode frequency normalized by the PNS dynamical time, depending on the PNS mass and radius alone. The result

is largely progenitor-independent (roughly 0.35 divided by the dynamical time), with only $\sim$10% variation by progenitor mass, suggesting that observations of gravitational wave frequencies from a galactic event will constrain the PNS mass and radius. Independent measurement of the PNS gravitational mass will further constrain the PNS radius, providing insight into the PNS mass-radius relation and nuclear equation of state.

5.8 Conclusions

We have provided in this Chapter the time series and angular distributions of the neutrino and gravitational-wave emissions of eleven state-of-the-art 3D non-rotating models of core-collapse supernovae and explored possible correlations between these signatures and the real-time dynamics of the shock and the proto-neutron-star core. This is the largest set of high-fidelity 3D simulations yet performed and reveals the global characteristics and general systematics for a wide range of available progenitor structures. Identifications of the predicted temporal fluctuations in these emissions in detectors on Earth can be used to constrain core and explosion dynamics in real time before, during, and after the supernova explosion is underway. We find that the neutrino emissions of non-rotating models retain a good degree of isotropy on average, but with instantaneous excursions about the mean inferred luminosity in a given direction of as much as $\pm$20%. Dipolar angular RMS variations in the neutrino emissions are generally restricted to $\sim$10% of the mean after the non-linear turbulent phase is reached and after the supernova is launched (if it is). Most explosions involve in their first phases simultaneous explosion and accretion, with a wasp-waist structure and unsymmetric-dipolar explosive ejection (Burrows et al., 2019). The deviation from isotropy is least for the "ν_μ"-type neutrinos. The temporal variations in the neutrino emissions reflect the motions of the standing accretion shock before

explosion, which itself correlates with the temporal and angular variations in the mass accretion rate through the shock. In particular, we identify a temporal correlation between the dipole component of the shock surface and the corresponding quantities for the accretion rate and the neutrino emissions. We also find that the vector direction of the dipole of the Y_e distribution in the inner region of proto-neutron-star convection and of that of the LESA are highly correlated, particularly after explosion. Furthermore, we witness the LESA phenomenon in all our models, though with distinctive differences in magnitude and temporal evolution.

We find, not unexpectedly, that the time series of the neutrino signatures at a detector bear the stamp of the hydrodynamics of shock motion before explosion and of episodic mass accretion after explosion. Determination of the characteristic timescales of these temporal fluctuations in the neutrino signals can be used to determine the timescales and behavior of shock motion. In particular, if there is a SASI (which we see for only non-exploding models, or over a short time span for models with late explosions), it is reflected in a correponding temporal variation at the SASI frequency in the neutrino signal and at twice the SASI frequency in the gravitational-wave signal. For our non-rotating model set, though the instantaneous values of the different gravitational strain polarizations, $h_{+,\times}$, can be out of phase, on average they are similar in magnitude and frequency content. However, their instantaneous angular variation, both for a given polarization and between polarizations, can be quite large. The relative magnitude of the different polarizations in the initial phase of gravitational radiation, associated with the distinct prompt-convection phase, bears the stamp of the angular character of the initial perturbations. Angular emission patterns and differences between polarizations would be even more pronounced for rapidly-rotating models for which a given preferred direction is set and for which polarization differences in the angular emission pattern won't average out (Hayama et al., 2018).

For our entire set of 3D models, we find strong connections between the cumulative neutrino energy losses, the radius of the proto-neutron star, and the f-mode frequency of the gravitational wave emissions. All these quantities are monotonic with time after bounce and measurement of, for instance, the f-mode frequency or the cumulative neutrino energy loss can be used to constrain the others. When physically normalized, the progenitor-to-progenitor variation in any of these reduced quantities is no more than $\sim$10%. Moreover, the f-mode frequency, times the instantaneous physical dynamical time, is independent of time after bounce to better than $\sim$10%. This implies that simultaneous measurement of gravitational waves and neutrinos from a given supernova event can be used together to extract real physical quantities of the core from which the supernova explosion is launched. Hence, and importantly, the neutrino data can aid in the interpretation of the gravitational-wave data, and vice versa. Since both the distance and spectral type of a galactic core-collapse progenitor are likely to be determined quickly, constraining possible core structures and enabling the determination of absolute neutrino and gravitational-wave powers, the additional correlations we highlight here will enhance the potential scientific return from a galactic event.

Here, we have mined our recent extensive suite of 3D supernova simulations to explore some of the correlations between core dynamics and its temporal evolution and the dominant neutrino and gravitational-wave signatures upon which this dynamics is stamped. The next step will be to filter our emission predictions through detector pipelines, including in the case of neutrinos the effect of neutrino oscillations (Seadrow et al., 2018). Whatever detector configurations exist and are online when the next galactic core-collapse supernova explodes, we hope we have demonstrated with here that modern 3D simulations, incorporating the necessary physical realism, can be used profitably and in detail to inform the interpretation of such a marvelous astronomical opportunity, when next it arises.

Chapter 6

Conclusions

The broader goal within the CCSNe community is to simulate successful explosions with energies of roughly one Bethe and with diagnostics consistent with observations. Towards this end, I have performed a comprehensive, multi-dimensional, and state-of-the art simulation study of core-collapse supernovae spanning a broad suite of progenitors with varying input physics. The majority of these models explode successfully.

To identify the drivers of successful core-collapse supernovae, I first explored the crucial role of detailed neutrino microphysics. In particular, I studied the role of the many-body medium correction to neutrino-nucleon scattering as well as inelasticity in neutrino-matter scattering. Both effects improve neutrino energy deposition in the stalled mantle and buttress the neutrino-heating mechanism as the preferred explosion mechanism for garden-variety CCSNe − those with expected explosion energies of one Bethe.

In a subsequent series of two-dimensional, axisymmetric simulations of 9 progenitors from 12 to 25 $M_{\odot}$, I investigated the role of the progenitor profile − in particular the presence of a steep Silicon-Oxygen layer located deep inside the collapsing star − as well as moderate rotation and velocity perturbations in promoting successful

CCSNe. Accretion of a sharp Si/O density interface, initially located around $\sim$1.5 $M_\odot$, provides a high accretion luminosity interior to the stalled shock and low ram pressure exterior to it. This combination provides a fertile breeding ground for successful shock revival and ultimate explosion. Models with such a feature were more conducive to explosion. Furthermore, since CCSNe work has largely focused on mapping and evolving spherically symmetric progenitors to multiple dimensions to study CCSNe phenomena, the addition of physically-motivated velocity perturbations allows us to approximate multi-dimensional effects, like convection, when initializing with a spherically symmetric progenitor model. Even models without a prominent Si/O interface can be prompted to explode with velocity perturbations and modest rotation. All the models studied could be thus nudged to explosion, indicating that many progenitors are indeed close to a critical condition for explosion. These studies effectively reframe the CCSNe problem: earlier failures to predict explosion for a range of progenitor masses do not suggest a critical failure of CCSNe theory, or of the neutrino-heating mechanism, but rather are indicative of a sensitive dependence to the detailed physics implemented.

These 2D simulations provided a test-bed for identifying crucial components for successful explosion. On the basis of these results, I then performed the first three-dimensional CCSNe simulation with Fornax, and one of the first high-fidelity 3D simulations − with detailed microphysics, respectable grid resolution, and state-of-the-art neutrino transport − in the broader CCSNe simulation community. The 16-$M_\odot$ progenitor, chosen for its steep Si/O interface, explodes promptly − within the first 100 milliseconds of core bounce − and accumulates energy robustly, at the rate of 2.5×10^{50} ergs per second through the first second with no sign of slowing down. This result emphasizes the need to carry out simulations in 3D to much longer timescales of 3−5 seconds to capture the asymptotic explosion energy.

In the subsequent year, FORNAX has been successfully used to study over twenty progenitors in high-fidelity 3D, more than all other current competitive groups combined. This provides the novel opportunity to study the global characteristics of stellar explosion across a diverse array of progenitor properties in detail. I discussed a subset of eleven of these models, focusing on the correlations between neutrino and gravitational signatures and the inner core dynamics of CCSNe (which would otherwise be obscured to study), as well as temporal and angular variations of these signatures, detectable by next-generation instrumentation. Simultaneous detection of neutrinos and gravitational waves can diagnose the properties of the remnant neutron star, the behavior of the stalled shock and mass accretion rate before explosion, and the broader diagnostics of CCSNe evolution. A more thorough study of observational signatures, including a nuclear network with predictions for nucleosynthesis (e.g., compared to SN1987 Nickel yields and distribution, i.e. Wongwathanarat et al. 2017), needs to be done.

Future work in CCSNe will need to address the concerns noted in the Introduction: producing robust explosions with diagnostics consistent with observations. As mentioned above, with little exception (Müller et al. 2017; Yoshida et al. 2019), the CCSNe community has been restricted largely to 1D progenitors, which neglect multi-dimensional turbulent, convective developments on collapse expected to be favorable to explosion outcome. With improving capability in CCSNe simulations, it is only a matter of time before progenitors are evolved fully in 3D, from collapse to explosion.

Furthermore, magneto-rotational effects may be significant in CCSNe evolution, in addition to the neutrino-heating mechanism. Beniamini et al. (2019) find that $\sim$40% of the galactic neutron population may exist as magnetars, which emphasizes both the importance of magnetic fields and rotation in massive star evolution. While believed to be responsible for hyper-energetic ($\sim$10 Bethe) supernovae (hypernovae), only $\sim$1% of CCSNe, rotational contributions to garden-variety CCSNe, with explosion

energies of $\sim$1 Bethe, may be appreciable (Fryer & Warren 2004; Takiwaki et al. 2016; Summa et al. 2018). In these simulations, rotation modifies neutrino energies and explosion outcome, albeit non-monotically, and does not act as a distinct explosion mechanism. To date, magneto-rotational simulations of CCSNe (e.g. Burrows et al. 2007b; Mösta et al. 2014) have used simplified treatment of neutrino transport (but see also Obergaulinger et al. 2018). This may very well change in the coming several years.

Lastly, upwards of 70% of massive stars may be in binaries, signifying the role of mass transfer in determining progenitor profiles (Sana et al. 2012) for both hydrogen-rich and hydrogen-stripped supernovae. Up to half of type II, hydrogen-rich, supernovae may have a history of binary interactions prior to explosion (Zapartas et al. 2019). However, the role of binary mass transfer in determining progenitor profile (e.g. Woosley 2019) has not been studied with self-consistent mass loss, although early simulations (Yoshida et al. 2019; Müller 2019) including binary interactions have been developed. Given the prevalence of stars in binaries, it is essential to identify any systemic differences between binary and single-star progenitors in explosion outcome.

The crux of the core-collapse problem has been the failure to produce vigorous explosions, and the above-mentioned requirements for future work may help resolve the problem. However, the comprehensive study, across a longitudinal suite of progenitor masses with detailed input physics, presented here yields a variety of explosions with robust energy growths. The CCSNe problem is better resolved than generally recognized.

Technical Acknowledgements

I, together with my collaborators, acknowledge helpful discussions with Todd Thompson regarding inelastic scattering, Evan O'Connor regarding the equation of state, Gabriel Martínez-Pinedo concerning electron capture on heavy nuclei, and Tuguldur Sukhbold and Stan Woosley regarding initial progenitor models. We also acknowledge invaluable support from Viktoriya Morozova with visualization using VisIt..

I employed computational resources provided by the TIGRESS high performance computer center at Princeton University, which is jointly supported by the Princeton Institute for Computational Science and Engineering (PICSciE) and the Princeton University Office of Information Technology, and by the National Energy Research Scientific Computing Center (NERSC), which is supported by the Office of Science of the US Department of Energy (DOE) under contract DE-AC03-76SF00098. This overall research project is also part of the Blue Waters sustained-petascale computing project, which is supported by the National Science Foundation and the state of Illinois. Blue Waters is a joint effort of the University of Illinois at Urbana-Champaign and its National Center for Supercomputing Applications. An award of computer time was provided by the INCITE program using Theta at the Argonne Leadership Computing Facility, which is a DOE Office of Science User Facility. This general project is also part of the "Three-Dimensional Simulations of Core-Collapse Supernovae" PRAC allocation support by the National Science Foundation. Our ongoing supernova efforts are enhanced through access to the resource Stampede2 in the Extreme Science and Engineering Discovery Environment (XSEDE). We acknowledge support from the U.S. Department of Energy Office of Science and the Office of Advanced Scientific Computing Research via the Scientific Discovery through Advanced Computing (SciDAC4).

Bibliography

Abbasi, R., Abdou, Y., Abu-Zayyad, T., et al. 2011, A&A, 535, A109

Abbott, B. P., Abbott, R., Abbott, T. D., et al. 2016a, ApJ, 818, L22

—. 2016b, Phys. Rev. Lett., 116, 061102

—. 2017, Physical Review Letters, 119, 161101

Abdikamalov, E., Burrows, A., Ott, C. D., et al. 2012, ApJ, 755, 111

Abdikamalov, E., Zhaksylykov, A., Radice, D., & Berdibek, S. 2016, MNRAS, 461, 3864

Abe, K., Abe, T., Aihara, H., et al. 2011, arXiv e-prints, arXiv:1109.3262

Abe, K., Haga, Y., Hayato, Y., et al. 2016, Astroparticle Physics, 81, 39

Ahmed, Z., Allada, K., Aniol, K. A., et al. 2012, Phys. Rev. Lett., 108, 102001

Andresen, H., Müller, B., Müller, E., & Janka, H. T. 2017, MNRAS, 468, 2032

Andresen, H., Müller, E., Janka, H. T., et al. 2019, MNRAS, 486, 2238

Ankowski, A., Beacom, J., Benhar, O., et al. 2016, arXiv e-prints, arXiv:1608.07853

Baade, W., & Zwicky, F. 1934, Proceedings of the National Academy of Science, 20, 254

Beniamini, P., Hotokezaka, K., van der Horst, A., & Kouveliotou, C. 2019, MNRAS, 487, 1426

Bethe, H. A., & Wilson, J. R. 1985, ApJ, 295, 14

Bliss, J., Arcones, A., & Qian, Y.-Z. 2018, ArXiv e-prints, arXiv:1804.03947

Blondin, J. M. 2005, in Journal of Physics Conference Series, Vol. 16, Journal of Physics Conference Series, ed. A. Mezzacappa, 370–379

Blondin, J. M., Mezzacappa, A., & DeMarino, C. 2003, ApJ, 584, 971

Blondin, J. M., & Shaw, S. 2007, ApJ, 656, 366

Bollig, R., Janka, H.-T., Lohs, A., et al. 2017, Physical Review Letters, 119, 242702

Brandt, T. D., Burrows, A., Ott, C. D., & Livne, E. 2011, ApJ, 728, 8

Bruenn, S. W. 1985, ApJS, 58, 771

Bruenn, S. W., De Nisco, K. R., & Mezzacappa, A. 2001, ApJ, 560, 326

Bruenn, S. W., & Dineva, T. 1996, ApJ, 458, L71

Bruenn, S. W., Mezzacappa, A., Hix, W. R., et al. 2013, ApJ, 767, L6

Bruenn, S. W., Lentz, E. J., Hix, W. R., et al. 2016, ApJ, 818, 123

Bruenn, S. W., Blondin, J. M., Hix, W. R., et al. 2018, arXiv e-prints, arXiv:1809.05608

Buras, R., Rampp, M., Janka, H.-T., & Kifonidis, K. 2006, A&A, 447, 1049

Burbidge, E. M., Burbidge, G. R., Fowler, W. A., & Hoyle, F. 1957, Rev. Mod. Phys., 29, 547

Burrows, A. 1987, ApJ, 318, L57

—. 2013, Reviews of Modern Physics, 85, 245

Burrows, A., Dessart, L., & Livne, E. 2007a, in American Institute of Physics Conference Series, Vol. 937, Supernova 1987A: 20 Years After: Supernovae and Gamma-Ray Bursters, ed. S. Immler, K. Weiler, & R. McCray, 370–380

Burrows, A., Dessart, L., Livne, E., Ott, C. D., & Murphy, J. 2007b, ApJ, 664, 416

Burrows, A., Dolence, J. C., & Murphy, J. W. 2012, ApJ, 759, 5

Burrows, A., & Fryxell, B. A. 1993, ApJ, 418, L33

Burrows, A., & Goshy, J. 1993, ApJ, 416, L75

Burrows, A., Hayes, J., & Fryxell, B. A. 1995, ApJ, 450, 830

Burrows, A., Livne, E., Dessart, L., Ott, C. D., & Murphy, J. 2007c, ApJ, 655, 416

Burrows, A., Radice, D., & Vartanyan, D. 2019, MNRAS, 485, 3153

Burrows, A., Reddy, S., & Thompson, T. A. 2006, Nuclear Physics A, 777, 356

Burrows, A., & Sawyer, R. F. 1998, Phys. Rev. C, 58, 554

—. 1999, Phys. Rev. C, 59, 510

Burrows, A., & Thompson, T. A. 2004, in Astrophysics and Space Science Library, Vol. 302, Astrophysics and Space Science Library, ed. C. L. Fryer, 133–174

Burrows, A., Vartanyan, D., Dolence, J. C., Skinner, M. A., & Radice, D. 2018, Space Sci. Rev., 214, 33

Cabezón, R. M., García-Senz, D., & Figueira, J. 2017, A&A, 606, A78

Cabezón, R. M., Pan, K.-C., Liebendörfer, M., et al. 2018, A&A, 619, A118

Cerdá-Durán, P., DeBrye, N., Aloy, M. A., Font, J. A., & Obergaulinger, M. 2013, ApJ, 779, L18

Colgate, S. A., & White, R. H. 1966, ApJ, 143, 626

Couch, S. M. 2013, ApJ, 775, 35

Couch, S. M., Chatzopoulos, E., Arnett, W. D., & Timmes, F. X. 2015, ApJ, 808, L21

Couch, S. M., & O'Connor, E. P. 2014, ApJ, 785, 123

Couch, S. M., & Ott, C. D. 2013, ApJ, 778, L7

—. 2015, ApJ, 799, 5

Dessart, L., Burrows, A., Livne, E., & Ott, C. D. 2006, ApJ, 645, 534

Dolence, J. C., Burrows, A., Murphy, J. W., & Nordhaus, J. 2013, ApJ, 765, 110

Dolence, J. C., Burrows, A., & Zhang, W. 2015, ApJ, 800, 10

Emmering, R. T., & Chevalier, R. A. 1989, ApJ, 345, 931

Eriguchi, Y., & Müller, E. 1985, A&A, 146, 260

Ertl, T., Janka, H.-T., Woosley, S. E., Sukhbold, T., & Ugliano, M. 2016, ApJ, 818, 124

Farmer, R., Fields, C. E., Petermann, I., et al. 2016, ApJS, 227, 22

Faucher-Giguère, C.-A., & Kaspi, V. M. 2006, ApJ, 643, 332

Fischer, T. 2016, A&A, 593, A103

Foglizzo, T. 2002, A&A, 392, 353

Foglizzo, T., Masset, F., Guilet, J., & Durand, G. 2012, Physical Review Letters, 108, 051103

Frebel, A. 2018, ArXiv e-prints, arXiv:1806.08955

Fröhlich, C., Martínez-Pinedo, G., Liebendörfer, M., et al. 2006, Physical Review Letters, 96, 142502

Fryer, C. L. 1999, ApJ, 522, 413

Fryer, C. L., Rockefeller, G., & Warren, M. S. 2006, The Astrophysical Journal, 643, 292

Fryer, C. L., & Warren, M. S. 2002, ApJ, 574, L65

—. 2004, ApJ, 601, 391

Fryxell, B., Mueller, E., & Arnett, D. 1991, ApJ, 367, 619

Fryxell, B., Olson, K., Ricker, P., et al. 2000, ApJS, 131, 273

Fujimoto, S.-i., & Nagakura, H. 2019, arXiv e-prints, arXiv:1906.09553

Gamow, G., & Schoenberg, M. 1940, Physical Review, 58, 1117

Gizzi, D., O'Connor, E., Rosswog, S., & Perego, A. 2019, arXiv e-prints, arXiv:1906.11494

Glas, R., Janka, H. T., Melson, T., Stockinger, G., & Just, O. 2018, arXiv e-prints, arXiv:1809.10150

Glas, R., Just, O., Janka, H. T., & Obergaulinger, M. 2019, ApJ, 873, 45

Goldberg, J. A., Bildsten, L., & Paxton, B. 2019, ApJ, 879, 3

Green, J., Hasan, N., Meinel, S., et al. 2017, Phys. Rev. D, 95, 114502

Guilet, J., & Fernández, R. 2014, MNRAS, 441, 2782

Hamacher, D. W. 2014, Journal of Astronomical History and Heritage, 17, 161

Handy, T., Plewa, T., & Odrzywołek, A. 2014, ApJ, 783, 125

Hanke, F., Marek, A., Müller, B., & Janka, H.-T. 2012, ApJ, 755, 138

Hanke, F., Müller, B., Wongwathanarat, A., Marek, A., & Janka, H.-T. 2013, ApJ, 770, 66

Hayama, K., Kuroda, T., Kotake, K., & Takiwaki, T. 2018, MNRAS, 477, L96

Heger, A., Woosley, S. E., & Spruit, H. C. 2005, ApJ, 626, 350

Hempel, M., & Schaffner-Bielich, J. 2010, Nucl. Phys. A, 837, 210

Herant, M., Benz, W., Hix, W. R., Fryer, C. L., & Colgate, S. A. 1994, ApJ, 435, 339

Hix, W. R., & Thielemann, F.-K. 1999, ApJ, 511, 862

Hoffman, R. D., Woosley, S. E., Fuller, G. M., & Meyer, B. S. 1996, ApJ, 460, 478

Horiuchi, S., Nakamura, K., Takiwaki, T., & Kotake, K. 2017, Journal of Physics G Nuclear Physics, 44, 114001

Horowitz, C. J., Caballero, O. L., Lin, Z., O'Connor, E., & Schwenk, A. 2017, Phys. Rev. C, 95, 025801

Hyper-Kamiokande Proto-Collaboration, :, Abe, K., et al. 2018, arXiv e-prints, arXiv:1805.04163

Janka, H.-T. 2012, Annual Review of Nuclear and Particle Science, 62, 407

Janka, H.-T., Melson, T., & Summa, A. 2016, Annual Review of Nuclear and Particle Science, 66, 341

Juodagalvis, A., Langanke, K., Hix, W. R., Martínez-Pinedo, G., & Sampaio, J. M. 2010, Nuclear Physics A, 848, 454

Just, O., Bollig, R., Janka, H.-T., et al. 2018, ArXiv e-prints, arXiv:1805.03953

Just, O., Obergaulinger, M., & Janka, H. T. 2015, MNRAS, 453, 3386

Kasen, D., & Woosley, S. E. 2009, ApJ, 703, 2205

Keil, W., Janka, H.-T., & Mueller, E. 1996, ApJ, 473, L111

Kitaura, F. S., Janka, H.-T., & Hillebrandt, W. 2006, A&A, 450, 345

Köpke, L., & IceCube Collaboration. 2011, in Journal of Physics Conference Series, Vol. 309, Journal of Physics Conference Series, 012029

Kotake, K. 2013, Comptes Rendus Physique, 14, 318

Kotake, K., Takiwaki, T., Fischer, T., Nakamura, K., & Martínez-Pinedo, G. 2018, ApJ, 853, 170

Kuroda, T., Kotake, K., Hayama, K., & Takiwaki, T. 2017, ApJ, 851, 62

Kuroda, T., Kotake, K., & Takiwaki, T. 2016a, ApJ, 829, L14

Kuroda, T., Kotake, K., Takiwaki, T., & Thielemann, F.-K. 2018, MNRAS, 477, L80

Kuroda, T., Takiwaki, T., & Kotake, K. 2016b, ApJS, 222, 20

Lattimer, J. M., & Swesty, F. 1991, Nuclear Physics A, 535, 331

Lentz, E. J., Bruenn, S. W., Hix, W. R., et al. 2015, ApJ, 807, L31

Liebendörfer, M., Whitehouse, S. C., & Fischer, T. 2009, ApJ, 698, 1174

Lu, J.-S., Cao, J., Li, Y.-F., & Zhou, S. 2015, Journal of Cosmology and Astro-Particle Physics, 2015, 044

Marek, A., Dimmelmeier, H., Janka, H.-T., Müller, E., & Buras, R. 2006, A&A, 445, 273

Marek, A., & Janka, H.-T. 2009, ApJ, 694, 664

Mathews, G. J., Boccioli, L., Hidaka, J., & Kajino, T. 2019, arXiv e-prints, arXiv:1907.10088

Melson, T., Janka, H.-T., Bollig, R., et al. 2015a, ApJ, 808, L42

Melson, T., Janka, H.-T., & Marek, A. 2015b, ApJ, 801, L24

Migenda, J. 2018, arXiv e-prints, arXiv:1804.01877

Minerbo, G. N. 1978, J. Quant. Spec. Radiat. Transf., 20, 541

Morozova, V., Piro, A. L., & Valenti, S. 2018a, ApJ, 858, 15

Morozova, V., Radice, D., Burrows, A., & Vartanyan, D. 2018b, ApJ, 861, 10

Mösta, P., Ott, C. D., Radice, D., et al. 2015, Nature, 528, 376

Mösta, P., Richers, S., Ott, C. D., et al. 2014, ApJ, 785, L29

Müller, B. 2015, MNRAS, 453, 287

—. 2016, PASA, 33, e048

—. 2019, arXiv e-prints, arXiv:1904.11067

Müller, B., Gay, D. W., Heger, A., Tauris, T. M., & Sim, S. A. 2018, MNRAS, 479, 3675

Müller, B., Heger, A., Liptai, D., & Cameron, J. B. 2016a, MNRAS, 460, 742

Müller, B., & Janka, H.-T. 2015, MNRAS, 448, 2141

Müller, B., Janka, H.-T., & Dimmelmeier, H. 2010, ApJS, 189, 104

Müller, B., Janka, H.-T., & Heger, A. 2012a, ApJ, 761, 72

Müller, B., Janka, H.-T., & Marek, A. 2012b, ApJ, 756, 84

Müller, B., Janka, H.-T., & Marek, A. 2013, The Astrophysical Journal, 766, 43

Müller, B., Melson, T., Heger, A., & Janka, H.-T. 2017, MNRAS, 472, 491

Müller, B., Viallet, M., Heger, A., & Janka, H.-T. 2016b, ApJ, 833, 124

Murphy, J. W., & Burrows, A. 2008, ApJ, 688, 1159

Murphy, J. W., & Dolence, J. C. 2017, ApJ, 834, 183

Murphy, J. W., Mabanta, Q., & Dolence, J. C. 2019, arXiv e-prints, arXiv:1904.09444

Nagakura, H., Burrows, A., Radice, D., & Vartanyan, D. 2019a, arXiv e-prints, arXiv:1905.03786

Nagakura, H., Furusawa, S., Togashi, H., et al. 2019b, ApJS, 240, 38

Nagakura, H., Sumiyoshi, K., & Yamada, S. 2019c, arXiv e-prints, arXiv:1906.10143

Nagakura, H., Iwakami, W., Furusawa, S., et al. 2018, ApJ, 854, 136

Nakamura, K., Horiuchi, S., Tanaka, M., et al. 2016, Monthly Notices of the Royal Astronomical Society, 461, 3296

Nakamura, K., Takiwaki, T., Kuroda, T., & Kotake, K. 2015, PASJ, 67, 107

Nomoto, K. 1984, ApJ, 277, 791

—. 1987, ApJ, 322, 206

Nordhaus, J., Burrows, A., Almgren, A., & Bell, J. 2010, ApJ, 720, 694

Noutsos, A., Schnitzeler, D. H. F. M., Keane, E. F., Kramer, M., & Johnston, S. 2013, MNRAS, 430, 2281

Obergaulinger, M. 2008, PhD thesis, Max-Planck-Institut für Astrophysik, Garching bei München

Obergaulinger, M., Just, O., & Aloy, M. A. 2018, Journal of Physics G Nuclear Physics, 45, 084001

O'Connor, E., Horowitz, C. J., Lin, Z., & Couch, S. 2017, in IAU Symposium, Vol. 331, Supernova 1987A:30 years later - Cosmic Rays and Nuclei from Supernovae and their Aftermaths, ed. A. Marcowith, M. Renaud, G. Dubner, A. Ray, & A. Bykov, 107–112

O'Connor, E., & Ott, C. D. 2010, Classical and Quantum Gravity, 27, 114103

—. 2011, ApJ, 730, 70

—. 2013, ApJ, 762, 126

O'Connor, E., Bollig, R., Burrows, A., et al. 2018, ArXiv e-prints, arXiv:1806.04175

O'Connor, E. P., & Couch, S. M. 2018a, ApJ, 865, 81

—. 2018b, ApJ, 854, 63

Oohara, K.-i., Nakamura, T., & Shibata, M. 1997, Progress of Theoretical Physics Supplement, 128, 183

Ott, C. D. 2009, Classical and Quantum Gravity, 26, 063001

Ott, C. D., Burrows, A., Thompson, T. A., Livne, E., & Walder, R. 2006, ApJS, 164, 130

Ott, C. D., Roberts, L. F., da Silva Schneider, A., et al. 2018, ApJ, 855, L3

Ott, C. D., Abdikamalov, E., O'Connor, E., et al. 2012, Phys. Rev. D, 86, 024026

Ott, C. D., Abdikamalov, E., Mösta, P., et al. 2013, The Astrophysical Journal, 768, 115

Pajkos, M. A., Couch, S. M., Pan, K.-C., & O'Connor, E. P. 2019, ApJ, 878, 13

Pan, K.-C., Mattes, C., O'Connor, E. P., et al. 2019, Journal of Physics G Nuclear Physics, 46, 014001

Pejcha, O., & Thompson, T. A. 2012, ApJ, 746, 106

Perego, A., Cabezón, R. M., & Käppeli, R. 2016, ApJS, 223, 22

Popov, S. B., & Turolla, R. 2012, Ap&SS, 341, 457

Powell, J., & Müller, B. 2019, MNRAS, 487, 1178

Pruet, J., Hoffman, R. D., Woosley, S. E., Janka, H.-T., & Buras, R. 2006, ApJ, 644, 1028

Radice, D., Abdikamalov, E., Ott, C. D., et al. 2018, Journal of Physics G Nuclear Physics, 45, 053003

Radice, D., Burrows, A., Vartanyan, D., Skinner, M. A., & Dolence, J. C. 2017, ApJ, 850, 43

Radice, D., Morozova, V., Burrows, A., Vartanyan, D., & Nagakura, H. 2019, ApJ, 876, L9

Raffelt, G. G. 2005, Physica Scripta, T121, 102

Raives, M. J., Couch, S. M., Greco, J. P., Pejcha, O., & Thompson, T. A. 2018, MNRAS, 481, 3293

Rampp, M., & Janka, H.-T. 2002, A&A, 396, 361

Rantsiou, E., Burrows, A., Nordhaus, J., & Almgren, A. 2011, ApJ, 732, 57

Richers, S., Nagakura, H., Ott, C. D., et al. 2017, ApJ, 847, 133

Ricks, W., & Dwarkadas, V. V. 2019, arXiv e-prints, arXiv:1906.07311

Roberts, L. F., Ott, C. D., Haas, R., et al. 2016, ApJ, 831, 98

Roberts, L. F., & Reddy, S. 2017, Phys. Rev. C, 95, 045807

Roberts, L. F., Reddy, S., & Shen, G. 2012, Phys. Rev. C, 86, 065803

Rosswog, S., & Liebendörfer, M. 2003, MNRAS, 342, 673

Ruffert, M., Janka, H.-T., & Schaefer, G. 1996, A&A, 311, 532

Sana, H., de Mink, S. E., de Koter, A., et al. 2012, Science, 337, 444

Scheck, L., Janka, H.-Th., Foglizzo, T., & Kifonidis, K. 2008, A&A, 477, 931

Schneider, A. S., Roberts, L. F., Ott, C. D., & O'connor, E. 2019, arXiv e-prints, arXiv:1906.02009

Seadrow, S., Burrows, A., Vartanyan, D., Radice, D., & Skinner, M. A. 2018, MNRAS, 480, 4710

Skinner, M. A., Burrows, A., & Dolence, J. C. 2016, ApJ, 831, 81

Skinner, M. A., Dolence, J. C., Burrows, A., Radice, D., & Vartanyan, D. 2019, ApJS, 241, 7

Sotani, H., Kuroda, T., Takiwaki, T., & Kotake, K. 2019, arXiv e-prints, arXiv:1906.04354

Srivastava, V., Ballmer, S., Brown, D. A., et al. 2019, arXiv e-prints, arXiv:1906.00084

Steiner, A. W., Hempel, M., & Fischer, T. 2013, ApJ, 774, 17

Sukhbold, T., Ertl, T., Woosley, S. E., Brown, J. M., & Janka, H.-T. 2016, ApJ, 821, 38

Sukhbold, T., Woosley, S. E., & Heger, A. 2018, ApJ, 860, 93

Summa, A., Hanke, F., Janka, H.-T., et al. 2016, ApJ, 825, 6

Summa, A., Janka, H.-T., Hanke, F., et al. 2017, in IAU Symposium, Vol. 329, The Lives and Death-Throes of Massive Stars, ed. J. J. Eldridge, J. C. Bray, L. A. S. McClelland, & L. Xiao, 449–449

Summa, A., Janka, H.-T., Melson, T., & Marek, A. 2018, ApJ, 852, 28

Suwa, Y., Sumiyoshi, K., Nakazato, K., et al. 2019, ApJ, 881, 139

Suwa, Y., Yamada, S., Takiwaki, T., & Kotake, K. 2016, ApJ, 816, 43

Takiwaki, T., Kotake, K., & Suwa, Y. 2012, ApJ, 749, 98

—. 2014, ApJ, 786, 83

—. 2016, MNRAS, 461, L112

Tamborra, I., Hanke, F., Janka, H.-T., et al. 2014a, ApJ, 792, 96

Tamborra, I., Hanke, F., Müller, B., Janka, H.-T., & Raffelt, G. 2013, Phys. Rev. Lett., 111, 121104

Tamborra, I., Raffelt, G., Hanke, F., Janka, H.-T., & Müller, B. 2014b, Phys. Rev. D, 90, 045032

Tews, I., Lattimer, J. M., Ohnishi, A., & Kolomeitsev, E. E. 2017, ApJ, 848, 105

Thompson, T. A., Burrows, A., & Horvath, J. E. 2000, Phys. Rev. C, 62, 035802

Thompson, T. A., Burrows, A., & Pinto, P. A. 2003, ApJ, 592, 434

Timmes, F. X., Woosley, S. E., & Weaver, T. A. 1996, ApJ, 457, 834

Torres-Forné, A., Cerdá-Durán, P., Obergaulinger, M., Müller, B., & Font, J. A. 2019, arXiv e-prints, arXiv:1902.10048

Totani, T., Sato, K., Dalhed, H. E., & Wilson, J. R. 1998, ApJ, 496, 216

Vartanyan, D., & Burrows, A. 2019, in American Astronomical Society Meeting Abstracts, Vol. 233, American Astronomical Society Meeting Abstracts #233, 113.04

Vartanyan, D., Burrows, A., & Radice, D. 2018a, in American Astronomical Society Meeting Abstracts, Vol. 231, American Astronomical Society Meeting Abstracts #231, 209.06

Vartanyan, D., Burrows, A., & Radice, D. 2019a, arXiv e-prints, arXiv:1906.08787

Vartanyan, D., Burrows, A., Radice, D., Skinner, M. A., & Dolence, J. 2018b, MNRAS, 477, 3091

—. 2019b, MNRAS, 482, 351

Vartanyan, D., & Burrows, A. S. 2017, in American Astronomical Society Meeting Abstracts, Vol. 229, American Astronomical Society Meeting Abstracts #229, 410.07

Vaytet, N. M. H., Audit, E., Dubroca, B., & Delahaye, F. 2011, J. Quant. Spec. Radiat. Transf., 112, 1323

Walk, L., Tamborra, I., Janka, H.-T., & Summa, A. 2018, Phys. Rev. D, 98, 123001

—. 2019, arXiv e-prints, arXiv:1901.06235

Wallace, J., Burrows, A., & Dolence, J. C. 2016, ApJ, 817, 182

Wanajo, S., Janka, H.-T., & Kubono, S. 2011, ApJ, 729, 46

Wanajo, S., Müller, B., Janka, H.-T., & Heger, A. 2018, ApJ, 852, 40

Willingale, R., Bleeker, J. A. M., van der Heyden, K. J., & Kaastra, J. S. 2003, A&A, 398, 1021

Wilson, J. R. 1985, in Numerical Astrophysics, ed. J. M. Centrella, J. M. Leblanc, & R. L. Bowers, 422

Wongwathanarat, A., Janka, H.-T., Müller, E., Pllumbi, E., & Wanajo, S. 2017, ApJ, 842, 13

Woosley, S. E. 2019, ApJ, 878, 49

Woosley, S. E., & Heger, A. 2007, Phys. Rep., 442, 269

Woosley, S. E., Heger, A., & Weaver, T. A. 2002, Reviews of Modern Physics, 74, 1015

Woosley, S. E., & Weaver, T. A. 1995, ApJS, 101, 181

Yakunin, K. N., Mezzacappa, A., Marronetti, P., et al. 2015, Phys. Rev. D, 92, 084040

Yoshida, T., Takiwaki, T., Kotake, K., et al. 2019, arXiv e-prints, arXiv:1903.07811

Zapartas, E., de Mink, S. E., Justham, S., et al. 2019, arXiv e-prints, arXiv:1907.06687

Zhang, W., Howell, L., Almgren, A., et al. 2013, ApJS, 204, 7